

COMPUTER AIDED DIAGNOSIS IN RADIOLOGY

A DISSERTATION
SUBMITTED TO THE DEPARTMENT OF ELECTRICAL AND
ELECTRONICS ENGINEERING
AND THE INSTITUTE OF ENGINEERING AND SCIENCES
OF BILKENT UNIVERSITY
IN PARTIAL FULFILLMENT OF THE REQUIREMENTS
FOR THE DEGREE OF
DOCTOR OF PHILOSOPHY

By
Metin Nafi Gürsoy
March 1999

THESIS
WP
815
G87
1999

COMPUTER AIDED DIAGNOSIS IN RADIOLOGY

A DISSERTATION

SUBMITTED TO THE DEPARTMENT OF ELECTRICAL AND ELECTRONICS

ENGINEERING

AND THE INSTITUTE OF ENGINEERING AND SCIENCES

OF BILKENT UNIVERSITY

IN PARTIAL FULFILLMENT OF THE REQUIREMENTS

FOR THE DEGREE OF

DOCTOR OF PHILOSOPHY

By

Metin Nafi Gürcan

March 1999

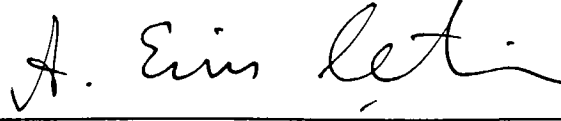
WP
815

-687

1999

8046843

I certify that I have read this thesis and that in my opinion it is fully adequate, in scope and in quality, as a thesis for the degree of Doctor of Philosophy.



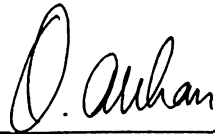
A. Enis Çetin, Ph. D. (Supervisor)

I certify that I have read this thesis and that in my opinion it is fully adequate, in scope and in quality, as a thesis for the degree of Doctor of Philosophy.



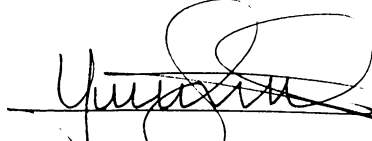
Hayrettin Köymen Ph. D.

I certify that I have read this thesis and that in my opinion it is fully adequate, in scope and in quality, as a thesis for the degree of Doctor of Philosophy.



Orhan Arıkan, Ph. D.

I certify that I have read this thesis and that in my opinion it is fully adequate, in scope and in quality, as a thesis for the degree of Doctor of Philosophy.



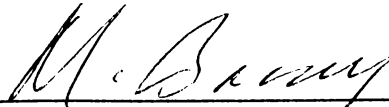
Ugur Gudukbay, Ph. D.

I certify that I have read this thesis and that in my opinion it is fully adequate, in scope and in quality, as a thesis for the degree of Doctor of Philosophy.



Volkan Atalay, Ph. D.

Approved for the Institute of Engineering and Sciences:



Prof. Dr. Mehmet Baray
Director of Institute of Engineering and Sciences

ABSTRACT

COMPUTER AIDED DIAGNOSIS IN RADIOLOGY

Metin Nafi Gürcan

Ph.D. in Electrical and Electronics Engineering

Supervisor: Prof. Dr. A. Enis Çetin

March 1999

Breast cancer is one of the most deadly diseases for middle-aged women. In this thesis, computer-aided diagnosis tools are developed for the detection of breast cancer on mammograms. These tools include a detection scheme for microcalcification clusters which are an early sign of breast cancer, and a method to detect the boundaries of mass lesions. In the first microcalcification detection method we propose, a subband decomposition structure is employed. Contrary to the previous work, the detection is carried out in the subband domain. The mammogram image is first processed by a subband decomposition filter bank. The resulting subimage is analyzed to detect microcalcification clusters. In regions corresponding to the healthy breast tissue the distribution is almost Gaussian. Since microcalcifications are small, isolated bright spots, they produce outliers in the subimages and the distribution of pixels deviates from Gaussian. The subimages are divided into overlapping square regions. In each square region, skewness and kurtosis values are estimated. As third and fourth order correlation parameters, skewness and kurtosis, are measures of the asymmetry and impulsiveness of the distribution, they can be used to find the locations of microcalcification clusters. If the values of these parameters are higher than experimentally determined thresholds then the region is marked as a potential cancer area. Experimental studies indicate that this method successfully detects regions containing microcalcifications.

We also propose another microcalcification detection method which uses two-dimensional (2-D) adaptive filtering and a higher order statistics based Gaussianity test. In this method, statistics of the prediction errors are computed to determine whether the samples are from a Gaussian distribution. The prediction error sequence deviates from Gaussianity around microcalcification locations because prediction of microcalcification

pixels is more difficult than prediction of the pixels corresponding to healthy breast tissue. Then, we develop a new Gaussianity test which has higher sensitivity to outliers. The scheme which uses this test gives better detection performance compared to the previously proposed methods. Within the detected regions it is possible to segment individual microcalcifications. An outlier labeling and nonlinear subband decomposition based microcalcification segmentation method is also investigated.

Two types of lesions, namely mass and stellate lesions, might be indicators of breast cancer. Finally, we propose a snake algorithm based scheme to detect the boundaries of mass lesions on mammograms. This scheme is compared with a recently developed region growing based boundary detection method. It is observed that the snake algorithm results in a more smooth boundary which is consistent with the morphological structure of mass lesions.

Keywords: Mammography, microcalcification, mass lesion, computer-aided diagnosis, Gaussianity tests, higher-order statistics, boundary detection.

ÖZET

RADYOLOJİDE BİLGİSAYAR DESTEKLİ TANI

Metin Nafi Gürcan
Elektrik ve Elektronik Mühendisliği Doktora
Tez Yöneticisi: Prof. Dr. A. Enis Çetin
Mart 1999

Meme kanseri orta yaştaki kadınlar için en ölümcül hastalıklardan birisidir. Bu tezde, mammogramlarda meme kanserinin bilgisayar destekli tanısı için yöntemler geliştirilmiştir. Bunlar içerisinde, meme kanserinin erken bir belirtisi olan mikrokalsifikasyon topaklanmalarının sezimlenmesi ve kütle lezyonlarının çevrelerinin bulunması için geliştirilmiş yöntemler vardır. Geliştirdiğimiz ilk mikrokalsifikasyon sezimleme yönteminde, altbantlara ayrıştırma yapısı kullanılmıştır. Daha önceki yapılmış çalışmaların aksine, sezimleme işlemi altbantta gerçekleştirilmiştir. Mammogram resmi öncelikle bir altbantlara ayrıştırma süzgeç dizisi ile işlenir. Ortaya çıkan alt-imege analiz edilerek, mikrokalsifikasyon topaklanmaları sezimlenir. Sağlıklı göğüs hücrelerine karşılık gelen bölgelerde yaklaşık olarak Gauss dağılımı gözlenir. Mikrokalsifikasyonlar küçük, ayrışık parlak bölgeler oldukları için, alt-imegelerde aykırı değer oluştururlar ve görellerin dağılımı Gauss dağılımından sapar. Alt-imegeler birbiri içine geçmiş kare bölgelere bölünür. Her bir kare içerisinde yamukluk ve savrukluk değerleri hesaplanır. Üçüncü ve dördüncü dereceden ilinti parametreleri yamukluk ve savrukluk, dağılımın bakışsızlık ve dürtüselliğini gösterdiğinden, mikrokalsifikasyon topaklanmalarının yerlerinin bulunmasında kullanılabilir. Eğer bir kare bölgede bu değerler, deneysel olarak belirlenmiş eşik değerlerinin üzerinde çıkarlarsa, o bölge potansiyel kanser bölgesi olarak işaretlenir. Deneysel çalışmalar göstermiştir ki bu yöntem mikrokalsifikasyon topaklanmalarının sezimlenmesinde başarılıdır.

Biz ayrıca iki boyutlu uyarlamalı süzgeçlemeye ve yüksek dereceli istatistiklere dayalı Gauss dağılımına uygunluk testlerinden yararlanan bir mikrokalsifikasyon topaklanması sezimleme algoritması öneriyoruz. Bu yöntemde, öngörü hatalarının bir Gauss dağılımından gelip gelmediği belirlenir. Öngörü hataları mikrokalsifikasyonların

olduđu bölgelerde Gauss dağılımından sapar çünkü mikrokalsifikasyona karşılık gelen görellerin öngörüsü sağlıklı meme hücrelerine karşılık gelen görellerin öngörüsünden daha zordur. Daha sonra, aykırılıklara daha yüksek duyarlılığa sahip bir Gauss dağılımına uygunluk testi geliştirilmiştir. Bu testi kullanan yeni bir sezimleme sistemi geliştirilmiş ve önceden önerilmiş yöntemlerle karşılaştırıldığında daha iyi bir başarıml elde edilmiştir. Sezimlenmiş bölgelerde, her bir mikrokalsifikasyonun bölütlenmesi mümkündür. Aykırı değeri etiketlemesine ve doğrusal olmayan altbantlara ayrıştırma yapıları kullanılan bölütleme yöntemleri incelenmiştir.

Kütle lezyonları ve yıldızsal lezyonlar meme kanserinin göstergeleri olabilir. Son olarak, kütle lezyonlarının çevrelerinin bulunması için yılan algoritmasına dayalı bir yöntem geliştirilmiştir. Bu yöntem, bölge büyötmeye dayalı benzer bir algoritma ile karşılaştırılmıştır. Yılan algoritmasının daha yumuşak bir çevre oluşturduğu gözlenmiştir ve bu da kütle lezyonlarının morfolojisine daha uygundur.

Anahtar Kelimeler: Mamografi, mikrokalsifikasyon, kütle lezyonu, bilgisayar destekli tanı, Gauss dağılımına uygunluk testleri, yüksek dereceli istatistikler, çevre sezimlemesi.

ACKNOWLEDGMENTS

I would like to thank my supervisor Prof. Dr. Enis Çetin for his supervision, guidance, and suggestions throughout the development of this thesis.

I am grateful to Dr. Yasemin Yardımcı for her invaluable help. Special thanks to Dr. Hayrettin Köymen, Dr. Orhan Arıkan, Dr. Uğur Güdükbay, Dr. Volkan Atalay for reading the manuscript and commenting on the thesis.

I thank all of my friends for their friendships throughout all these years.

It is a pleasure to express my special thanks to my mother, father, and brother for their sincere love, support and encouragement.

Aileme.

Contents

1	INTRODUCTION	1
1.1	Computer-Aided Diagnosis	2
1.2	Previous Work	4
1.3	Outline of the Thesis	10
2	MICROCALCIFICATION DETECTION USING FILTERING AND HIGHER ORDER STATISTICS	12
2.1	Characterization of Microcalcifications	13
2.2	Mammogram Database	17
2.3	Pre-Processing of Mammogram Images	17
2.3.1	Segmentation of Breast Region	18
2.3.2	Linear Processing of Mammogram Images	22
2.4	Statistical Detection Method	24
2.4.1	HOS Measures: Skewness and Kurtosis	26
2.4.2	HOS Based Detection	27
2.5	Nonlinear Subband Decomposition Structures	30
3	MICROCALCIFICATION DETECTION USING ADAPTIVE FILTERING AND HIGHER ORDER STATISTICAL TESTS	37

3.1	2-D Adaptive Prediction based Tests for Microcalcification Detection	38
3.1.1	Adaptive Filtering	38
3.1.2	2-D Adaptive Filtering	40
3.1.3	Gaussianity Test	43
3.1.4	Experimental Results	45
3.2	A Gaussianity Test Using Fourth Order Parameters	46
3.2.1	The Influence Function	47
3.2.2	The Sensitivity Curve of the OCM Test	48
3.2.3	New Gaussianity Test Using Fourth Order Moment	51
4	MICROCALCIFICATION SEGMENTATION and MAMMOGRAM ENHANCEMENT	60
4.1	Segmentation of Microcalcifications	62
4.1.1	Adaptive Filtering based Subband Decomposition	62
4.1.2	Boxplot Outlier Labeling Method	66
4.2	Mammogram Image Enhancement	68
4.2.1	Superposition and Amplification Based Enhancement	69
4.2.2	Nonlinear Subband Decomposition Based Enhancement	73
5	DETECTION OF MASS LESION BOUNDARIES USING THE SNAKE ALGORITHM	79
5.1	Mass Lesion	80
5.2	Breast Boundary Detection by Fuzzy Set Pre-processing and Region Growing	82
5.2.1	Fuzzy Set Pre-processing	82
5.2.2	Region Growing Algorithm	83

5.3	The Snake Algorithm	84
5.4	Detection of Mass Lesion Boundaries using the Snake Algorithm	88
6	CONCLUSIONS	92
	APPENDICES	95
A	Bandpass Filter Equivalents of Subband Decomposition Structures	95
B	Frequency Band Characteristics of Tree-Structured Filter Banks	101
B.1	Binary Tree-structured Subband Filtering	102
B.2	Arbitrary Tree-Structured Subband Filtering	104
C	Identification of Relative Protein Bands in Polyacrylamide Gel Electrophoresis (PAGE) Using Multiresolution Snake Algorithm	107
C.1	Methods	108
C.2	Results	110
C.3	Discussion	116
Vita		125

List of Figures

1.1	Block diagram of a generic CAD system.	2
2.1	Part of a mammogram image containing microcalcification cluster.	13
2.2	Cross section of a part of a mammogram image with microcalcifications. The locations of microcalcifications are indicated by arrows.	14
2.3	Cross section of a part of a mammogram image with microcalcifications. The locations of microcalcifications are indicated by arrows.	15
2.4	Typical mammogram image (cranio caudal view).	18
2.5	Horizontal profile of the mammogram image in Figure 2.4.	19
2.6	Vertical profile of the mammogram image in Figure 2.4.	19
2.7	The adaptive iterative thresholding algorithm.	21
2.8	Segmented breast area of the mammogram image in Figure 2.4.	22
2.9	The magnitude response of the overall bandpass filter.	23
2.10	Skewness and Kurtosis are estimated in overlapping square regions.	25
2.11	100x100 region with microcalcifications, distribution after linear processing and magnified view of the tail.	25
2.12	100x100 region with no microcalcification, distribution after linear processing	26
2.13	Detection scheme output, (a) part of a mammogram image, (b) regions with microcalcifications as indicated by the detection scheme.	29

2.14	Nonlinear Subband Decomposition Structure.	31
2.15	Median filter based nonlinear processing (a) A line extracted from the mammogram image (b) the median filter output (c) the difference between the signals in (a) and (b).	33
2.16	100x100 region with microcalcifications, distribution after nonlinear processing and magnified view of the tail.	34
2.17	100x100 region with no microcalcification, distribution after nonlinear processing	34
3.1	Adaptive filtering structure.	39
3.2	2-D adaptive filter structure.	41
3.3	Region of support (ROS) of the adaptive filter. ROS is “anticausal.” . . .	41
3.4	(a) Part of a mammogram image containing a microcalcification cluster (b) The error image obtained after the 2-D adaptive filtering	42
3.5	Causal, semicausal and noncausal finite prediction windows.	42
3.6	Scanning directions in adaptive filtering.	43
3.7	Error value distributions in regions (a) without microcalcifications, and (b) with microcalcifications. (c) shows the an enlarged view of the tail of the distribution in (b).	45
3.8	Sensitivity curves for mean estimator (dashed lines) and for the OCM Gaussianity test in Equation 3.28 (solid line).	52
3.9	Sensitivity curves for the Gaussianity test in Equation 3.28 (solid line) and for the Gaussianity test in Equation 3.50 (dashed line).	56
3.10	Sensitivity curves for skewness (dashed line) and the OCM Gaussianity test (solid line).	58
3.11	Sensitivity curves for kurtosis (dashed line) and our Gaussianity test (solid line).	58
4.1	Microcalcification segmentation structure.	61

4.2	Adaptive Structure Analysis Stage in [52].	62
4.3	Adaptive Structure Synthesis Stage in [52].	63
4.4	Adaptive filtering based subband decomposition for microcalcification segmentation.	64
4.5	Comparison of detail images produced by different breast structure removal operations. (a) Original line of mammogram image, (b) bandpass filtering, (c) adaptive filtering, (d) nonlinear subband decomposition (e) adaptive filtering based subband decomposition	65
4.6	Illustration of the outlier detection by the boxplot outlier labeling method described in Section 4.1.2.	66
4.7	Microcalcification segmentation using outlier detection: (a) A horizontal line of the mammogram image which is known to contain a microcalcification, (b) high-band sub-signal x_h , (c) output of the outlier detection method.	67
4.8	(a) A region of a mammogram image containing microcalcifications, (b) output of the segmentation.	68
4.9	Mammogram image enhancement.	68
4.10	Superposition based mammogram image enhancement: (a) A horizontal line of the mammogram image, (b) the detail signal, $y_d[n]$ obtained by nonlinear subband decomposition, (c) output of the outlier detection method, (d) microcalcifications are enhanced by superposition.	70
4.11	Amplification based mammogram image enhancement: (a) A horizontal line of the mammogram image, (b) the detail signal, $y_d[n]$ obtained by nonlinear subband decomposition, (c) output of the outlier detection method, (d) microcalcifications are enhanced by amplification.	71
4.12	Comparison of mammogram image enhancement schemes: (a) A horizontal line of the mammogram image, (b) mammogram image enhancement by superposition, (c) mammogram image enhancement by amplification.	72

4.13	Enhanced Images (a) Microcalcifications are superimposed on the mammogram image, (b) Mammogram image is magnified at the locations of microcalcifications.	72
4.14	(a) Enhanced and (b) contrast stretched images for the mammogram image in Figure 4.8 (a).	73
4.15	Nonlinear Subband Decomposition Structure.	73
4.16	Median filter based nonlinear subband decomposition.	75
4.17	Microcalcification segmentation using the closing filtering on the difference image.	75
4.18	Enhancement of the mammogram image by nonlinear subband decomposition.	76
4.19	Enhancement of mammogram image by nonlinear subband decomposition: (a) A region of a mammogram image containing microcalcifications, (b) output of the segmentation (c) enhanced mammogram image.	76
4.20	Mammogram image enhancement scheme.	77
4.21	Results of mammogram image enhancement: (a) Part of a mammogram image to be enhanced (b) Output of the contrast stretching operation (c) Superposition based enhancement (d) Magnification based enhancement.	78
5.1	Part of a mammogram image with a circumscribed mass lesion.	80
5.2	Cross section of the mammogram image in horizontal direction.	81
5.3	Cross section of the mammogram image in vertical direction.	81
5.4	Membership functions for two different values of β . $\beta = 0.007$ (Solid line), $\beta = 0.07$ (Broken line).	83
5.5	(a) Part of a mammogram image containing a mass lesion (b) Fuzzy Set based pre-processing of (a).	84
5.6	Output of the region growing algorithm for the detection of the mass lesion boundaries.	85
5.7	The mass lesion boundary detection algorithm.	88

5.8	(a) Part of a mammogram image containing a mass lesion, (b) after histogram equalization.	88
5.9	(a) Part of a mammogram image (b) Initial position of the snake, (c), (d), (e), (f) The position of the snake at each iteration.	89
5.10	(a) Original image (b) Region marked by the radiologist (c) Output of the snake algorithm.	90
A.1	Binary tree structured 2-level subband decomposition and weighting. The subsignal X_0 contains $[0, \frac{\pi}{4}]$, X_1 contains $[\frac{\pi}{4}, \frac{\pi}{2}]$, X_2 contains $[\frac{3\pi}{4}, \pi]$, X_3 contains $[\frac{\pi}{2}, \frac{3\pi}{4}]$, frequency ranges of the original signal, $X(n)$	96
A.2	The overall filter amplitude response using the LAD8 wavelet. Only the 2nd and 3rd scales are included in the final image [10].	96
A.3	The ideal filter amplitude response obtained using the weights in Table A.2.	97
A.4	The overall filter amplitude response using the LAD8 wavelet: Weighted scales [6].	99
A.5	The overall filter amplitude response using the Biorthogonal Spline wavelet and including the 2nd and 3rd scales [11].	99
A.6	The overall filter amplitude response using the LAD4 wavelet and including the first 4 scales [12].	100
B.1	Binary tree-structured 2-level subband decomposition.	102
B.2	4-channel decomposition of a signal.	103
B.3	Tree structure generation of a ternary Gray code.	105
B.4	A hybrid tree structure.	106
C.1	(a) Denaturing PAGE image, (b) a lane of the denaturing PAGE image.	109
C.2	Histograms of three different regions of a PAGE image.	109

C.3	Change of different energy components. Solid lines indicate the energy changes in the high-resolution image and dashed lines show the energy changes in the lower-resolution image.	111
C.4	Protein of interest is enclosed within the snake : (a) Original lane image (b) Snake obtained using only the low-resolution image (c) Snake obtained using only the high-resolution image (d) Snake obtained using the multiresolutional approach.	112
C.5	Results of the initialization process : (a) Initial position of the snake located on the extracted edge (b) The snake in (a) after one iteration on low-resolution image (c) Snake obtained using the multiresolutional approach with the initial snake in (c).	113
C.6	Different regions of interest for percentage calculations shown in (a) , (b), (c) Percentage calculations of our program are compared with the eye estimate of a molecular biologist.	114
C.7	(a) Known amounts of protein bands determined by Bradford protein assay, (b) Comparisons of percentage calculations of our software and a commercial software.	115

List of Tables

2.1	Filter Coefficients	23
2.2	Skewness, $\hat{\gamma}_3$, and kurtosis, $\hat{\gamma}_4$ estimates of the data plotted in Figures 2.11 and 2.12.	24
2.3	Skewness and Kurtosis estimates on the original image, (a) regions with microcalcifications, (b) regions without microcalcifications.	28
2.4	Skewness and Kurtosis estimates on the bandpass filtered image, (a) regions with microcalcifications, (b) regions without microcalcifications. .	28
2.5	Skewness and Kurtosis estimates on the highpass filtered image, (a) regions with microcalcifications, (b) regions without microcalcifications .	29
2.6	Skewness and Kurtosis estimates of the distributions in Figures 2.16 and 2.17.	33
2.7	Skewness and Kurtosis Estimates on the detail image after nonlinear subband decomposition, (a) regions with microcalcifications, (b) regions without microcalcifications.	35
3.1	Statistics of h in regions with microcalcifications.	45
3.2	Statistics of h in regions no microcalcification.	45
3.3	Test statistics in regions with microcalcifications.	57
3.4	Test statistics in regions with no microcalcification.	57

3.5	Test statistics obtained from bandpass filtered images in regions with microcalcifications: the OCM test $h(I_1, I_2, I_3)$ and our Gaussianity test $H(I_1, I_2, I_4)$.	59
3.6	Test statistics obtained from bandpass filtered images in regions with no microcalcification: the OCM test $h(I_1, I_2, I_3)$ and our Gaussianity test $H(I_1, I_2, I_4)$.	59
5.1	The snake algorithm.	87
A.1	8-tap Least Asymmetric Daubhecies' filter coefficients.	97
A.2	Optimized weights of the wavelet scales.	97
A.3	9-tap Biorthogonal spline wavelets.	98
A.4	4-tap Least Asymmetric Daubhecies' filter coefficients.	98
C.1	Number of computations for high and low resolution	116

Chapter 1

INTRODUCTION

Breast cancer is one of the most deadly diseases for middle-aged women. One out of eight women is prone to this disease in her lifetime [1]. The success of treatment depends on early detection. Therefore, women, especially in their middle ages, must be regularly screened [2]. Mammography (X-ray image of breasts) is the commonly used screening technique for the early detection and it is recommended by the American Cancer Society to asymptomatic women over the age of 40 [2].

Breast cancer detection in mammogram images is currently carried out by radiologists who examine mammograms with a magnifying glass to find out tumors such as *microcalcifications, masses, and stellate lesions* [3]. Clustered microcalcifications are observed between 30% and 50% of breast cancer cases [4, 5]. Microcalcifications are tiny calcium deposits in breast parenchymal tissue structures, which appear as small bright spots on mammograms. A cluster is defined as 3 or more microcalcifications within a 1 cm^2 area. Microcalcification sizes vary from 0.01 mm^2 to 1 mm^2 . With the current 50 *micron* scanning technology, the smallest microcalcification appears as a 2 pixel by 2 pixel bright region in the digital mammogram image. Since microcalcifications are small and subtle abnormalities, they may be overlooked by an examining radiologist. For instance, in retrospective studies it has been determined that between 10%-30% of the undetected breast cancers are actually visible on mammograms [2].

While microcalcifications are regarded as an early sign of breast cancer, two types of lesions, namely mass and stellate lesions might be indicators of cancer. A mass appears on the mammogram as an almost uniform density elliptical disk. It is brighter than its

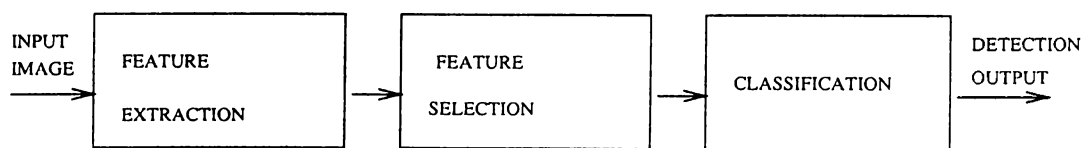


Figure 1.1: Block diagram of a generic CAD system.

surrounding area and its edges are fuzzy. A stellate lesion has a central mass very much like a mass. Additionally, it has sharp fine lines (spicules) emanating from the center [3].

1.1 Computer-Aided Diagnosis

Recently, pattern recognition and image processing techniques have been used in the analysis of medical images [1, 6]. Resulting systems are called Computer-Aided Diagnosis (CAD) systems. In general, a generic CAD system consists of three main tasks as shown in Figure 1.1 [13]:

- **Feature Extraction:** Different sets of features are extracted either from the original image through some measurements (e.g., size of microcalcifications), or from processed images. Image can be processed by the Fourier transform, the wavelet transform or nonlinear filter based transforms. For instance, higher order correlations, autocorrelation, energy, and entropy are some of the features corresponding to a group of pixels in the wavelet domain [12].
- **Feature Selection:** Extracted features are grouped to achieve maximum separability. The aim is to obtain non-overlapping feature classes such that a perfect separability is possible. Some popular feature selection methods include genetic algorithms, multivariable cluster analysis [7].
- **Classification:** The selected set of features are classified using, for instance, linear and quadratic classifiers, binary decision trees, standard back-propagation network, dynamic neural networks, and K-nearest neighbor rule [5].

A user-friendly interface is also an important part of a CAD system as most radiologists may not be familiar with computers.

Radiography is entering a new phase of development after the introduction of digital techniques. Now, some of the modalities such as *Computed Radiography (CR)*, *Digital Subtraction Angiography*, *Digital Mammography*, *Computed Tomography(CT)*, and *Magnetic Resonance Imaging (MRI)* produce digital outputs, directly. For archiving purposes, analog radiographs are digitized. Hence, digital image processing techniques will be utilized for a wide range of radiological applications. Some examples of the use of computer-aided techniques for different modalities are given in [23]. These include detection of pulmonary nodules and pneumothorax; detection and characterization of interstitial disease; and analysis of heart size in chest radiography. In angiography, stenotic lesions are analyzed by computerized methods. In mammography, mass, stellate lesions, and microcalcification clusters are detected and classified.

CAD will be an important feature of next generation Picture Archiving and Communication Systems (PACS), with which filmless hospitals are envisaged [14]. In these systems, radiological pictures are captured, stored and communicated digitally. Many hospitals all over the world have these systems.

It is clinically observed that the detection rate increases if the same mammogram image is read by two different radiologists. However, employing two radiologists for double reading is not always feasible. Currently, CAD systems are intended to act as “second readers” rather than to replace radiologists.

In a computerized detection system there are four possible outcomes:

- 1) There is an abnormality and it is detected (true positive),
- 2) there is an abnormality and it is missed,
- 3) there is no abnormality but something is detected (false positive), and
- 4) there is no abnormality and nothing is detected.

Preliminary studies indicate that CAD systems increase the performance of radiologists [9]. With the help of CAD systems, radiologists can detect all suspicious regions on mammograms (i.e., high sensitivity), while not marking healthy regions as suspicious (i.e., high specificity) [8]. High sensitivity means achieving the maximum true positive rate while high specificity means having the minimum false negative rate.

Two factors contributed to a recent worldwide increased interest in CAD systems for mammography. First, there has been (and will be) a significant increase in the number

of mammograms to be examined due to national screening programs through which all women over the age of 40 are advised to undergo regular mammogram exams. The second factor is the introduction of digital techniques in radiography, and availability and proliferation of digital radiological images. In this thesis, we develop CAD tools for the detection and analysis of breast abnormalities on mammogram images.

1.2 Previous Work

A significant part of CAD research for mammography has concentrated on the early detection of breast cancer, and in particular the detection of microcalcifications. In one of the early works in this field, a difference-image technique is employed [2]. First, the image is processed by two filters and their outputs which are called the signal-suppressed image and signal-enhanced image, are subtracted from each other. The first filter, the signal enhancement filter is a spatial filter approximately matching to the size and contrast variations of typical microcalcifications. This filter is designed to increase the peak intensity values of microcalcification pixels relative to the background pixels. Different forms of filters such as median filters and box-rim filters are used for signal suppression filters. The difference image is grey-level thresholded to single out microcalcification locations from the noise. The area and the contrast values of the pixels with values higher than globally and locally set threshold values are then analyzed. The resultant parts of the image are considered to be microcalcifications and these are clustered. This CAD system has 87% true-positive cluster detection accuracy at a false-positive detection rate of 4 clusters per image in a mammogram database consisting of 60 mammograms [9].

Woods *et al.* compare different pattern recognition techniques for the detection of microcalcifications on mammograms [5]. They employ a multistage detection algorithm. The first stage is segmentation. At this stage, a local contrast image is computed by subtracting from each pixel the average value of 15×15 region surrounding that pixel. The maximum value in the local contrast image defines a threshold value. The pixels with values higher than this threshold constitute the locally bright spots on the mammogram. Some of these local bright spots are eliminated by region growing algorithm (described in Chapter 4). A feature vector consisting of 29 components are considered to characterize the resultant image. Seven of these features are selected to form a feature vector: area of the object, average grey level of the object, gradient strength of the object's perimeter pixels, root mean square (RMS) noise fluctuations in the object, RMS noise fluctuation

in the surrounding background, contrast, a low order moment based shape descriptor. Finally, seven different classifiers are used to detect microcalcification clusters: linear and quadratic classifiers, binary decision trees, a standard back-propagation network, 2 dynamic neural networks, and a K-nearest neighbor classifier. Based on the experiments performed on a database of 24 images, the authors conclude that the simple Bayesian linear classifier performs the best according to the receiver operating characteristics (ROC) curve methodology . The results are dependent on the choice of the feature set and on finding a good operating point.

Recently, a variety of wavelet transform based schemes has been proposed for the computerized detection of microcalcifications [4, 6, 10]. In these schemes, the mammogram image is first passed through a subband decomposing filter bank. Then, a selected set of subband images are weighted to enhance the microcalcification locations. Next, a new image is reconstructed from the weighted sub-images. In the detection step, global and local gray-level thresholds are applied to the reconstructed image to extract possible microcalcification locations. Finally, these locations are grouped to identify microcalcification clusters.

In wavelet based schemes, microcalcification detection is carried out on the reconstructed image. These schemes mainly differ in their choice of wavelet filters and the selection of subband images used in the reconstruction. For example, Yoshida *et al.* use the Least Asymmetric Daubechies' wavelet with 8 coefficients (LAD8) [10]. Only the second and third scales of the wavelet transform are selected for the reconstruction. In their later work [6], they employ seven different scales, only the first three of which are given more emphasis by higher weights. Strickland and Hahn use the biorthogonal spline wavelet with nine coefficients [11]. In another work, Wei *et al.* use the Least Asymmetric Daubechies' wavelet with 4 coefficients (LAD4) [12]. They include only the first four scales for feature extraction. We show that these wavelet based schemes are essentially equivalent to linear filtering followed by thresholding. In Appendix A, we demonstrate the equivalence and give equivalent linear filter responses.

Clarke *et al.* develop a microcalcification detection method based on a tree-structured non-linear filter, edge detector, and the wavelet transform [8, 21]. The mammogram image is first filtered with multistage, tree-structured nonlinear filters. The major filtering blocks are Central-Weighted Median Filters (CWMF). In calculation of the CWMF, the current pixel is given more weight by including several copies of it in the

usual median calculation. The purpose of CWMF filters is to increase the signal-to-noise ratio and to suppress the undesired background structures. Next, a *quasi-range dispersion edge detector* enhances the edges. The output of the edge detector is input to the wavelet transform. Finally, a linear combination of the wavelet transform coefficients is utilized to extract microcalcifications. In their evaluation of nine images, the authors detected all the clusters with an average of four false clusters per image.

Segmentation of individual microcalcifications after detecting their locations is the next step in diagnosis. In this step, the size and shape information of microcalcifications are extracted. This information can be used by radiologists while classifying the clusters as malignant or benign. Another important decision factor for the classification of clusters is the three-dimensional arrangement of microcalcifications within the cluster. For example, *ductal carcinoma in situ* tend to show linear arrangements while microcalcifications caused by cysts are often arranged on the surface of a sphere [17]. Müller *et al.* [18, 19] built a system to reconstruct and visualize the three-dimensional arrangement of a cluster from only two different views. The final decision is based on breast biopsy.

Dengler *et al.* employ a nonlinear filtering approach for microcalcification detection and segmentation [20]. The first step of this detection scheme is background gray level elimination. A broadband highpass filter eliminates the large background structures. The resulting image is thresholded. The value of the threshold is 0 because microcalcifications are expected to have pixel values greater than 0. Then, the processed mammogram image is filtered with two Gaussian filters of different standard deviations, σ_+ and σ_- . The standard deviation σ_+ is proportional to the microcalcification size and the standard deviation σ_- is related to the expected distance between microcalcifications. A circularly symmetric Gaussian filter in two dimensions is defined as:

$$g[m, n] = \frac{1}{2\pi\sigma^2} e^{-\frac{m^2+n^2}{2\sigma^2}} \quad (1.1)$$

where σ is the standard deviation of the filter, $(m, n) \in \mathcal{R}$ and $\mathcal{R} = [-N, \dots, 0, \dots, N] \times [-N, \dots, 0, \dots, N]$. The difference of two filtered images is thresholded to locate suspicious spots. The value of the threshold is determined from the final image as a multiple of the standard deviation of the noise in the difference image. Finally, the thresholded image is nonlinearly processed by morphological opening and thickening operations to extract the original shape and size of microcalcifications. They obtained 97% sensitivity at 70% specificity for the 24 images they used. Although it is not realized

by the authors, this method is also based on bandpass filtering as utilized Gaussian filters are two low-pass filters and their difference turns out to be a bandpass filter.

Dhawan *et al.* propose a scheme for the classification of microcalcifications on mammogram images as *benign* or *malignant* [7]. The first step of the method is the manual extraction of regions of interest on mammograms. These regions contain microcalcification clusters. Next, they compute global texture features from second-order histogram statistics: entropy, contrast, angular second moment, inverse difference moment, correlation, mean, deviation. The image is subband decomposed using the Daubechies' wavelet filters of size 6 and 20. Local texture features, energy and entropy are computed on the original image and four subband images (low-low, low-high, high-low, high-high). The energy, E and the entropy, H for an $M \times N$ region are defined as

$$E = \frac{\sum_{m=1}^M \sum_{n=1}^N x^2[m, n]}{N \times M} \quad (1.2)$$

$$H = - \sum_{m=1}^M \sum_{n=1}^N \frac{x^2[m, n]}{S} \log \left(\frac{x^2[m, n]}{S} \right) \quad (1.3)$$

where S is the sum of the squares of pixel intensity values, $x[m, n]$ within the region of interest, $S = \sum_{m=1}^M \sum_{n=1}^N x^2[m, n]$. The global and local texture features are combined with another feature set which include features such as the distance between microcalcifications and the number of microcalcifications. Among all these extracted features, the best set of features is selected by means of multivariate cluster analysis and a genetic algorithm-based search method. Finally, back-propagation neural networks and parametric statistical classifiers are used to classify the selected features. The authors conclude that genetic algorithm-based best feature selection combined with the neural network classifier gives the best performance in the classification of "difficult-to-diagnose" microcalcifications.

Another branch of computer-aided diagnosis for mammography deals with mass detection and stellate lesion detection on mammograms. In [22], it was determined that the length of the long axis of the masses varies in size from 6 mm to 26 mm. Compared to microcalcifications, these abnormalities are considerably larger but their detection is still difficult because they look very much like the surrounding parenchymal tissue and their contrast is usually low.

Doi *et al.* propose a mass detection scheme by taking advantage of the fact that normal right and left breasts [23] are symmetrical. If a tumor is developed in one of the breasts then this symmetry is disturbed. Hence, a comparison between left and right breast mammograms reveals the locations of the masses. The symmetry comparison is also a common practice for radiologists in their diagnosis of mass lesions. In computerized detection, first, left and right breast images are aligned. After suitable adjustments, the left and right breast images are subtracted from each other. The difference image shows a discrepancy at locations of mass lesions.

Gulsrud and Kjode propose a linear filter design method for the mass and stellate detection [3]. Mammograms are first filtered by a linear filter which is designed according to the Fisher criterion is defined in Equation 1.4. This filter is designed to maximally separate the local energies of the normal breast tissue and suspicious areas. The output of the filter is squared and then low-pass filtered. The operations of squaring and smoothing by low-pass filtering make it possible to segment suspicious regions by a simple thresholding. The Fisher criterion implies that the filter maximally separates the mean values of healthy and abnormal regions, while keeping the variances within these regions as low as possible. The objective function is defined as

$$J(\mathbf{h}) = \frac{(\mu_{v_1}(\mathbf{h}) - \mu_{v_2}(\mathbf{h}))^2}{\sigma_{v_1}^2(\mathbf{h}) + \sigma_{v_2}^2(\mathbf{h})} \quad (1.4)$$

where $\mu_{v_i}(\mathbf{h})$ and $\sigma_{v_i}(\mathbf{h})$, $i = 1, 2$ are the mean and standard deviation of normal and suspicious regions, respectively, and these are functions of the filter coefficients, \mathbf{h} .

The optimization is achieved taking the derivative of Equation 1.4 with respect to \mathbf{h} and equating it to zero. A simple gradient search gives the solution. However, in order to avoid the risk of converging to a local minimum, a close form of the solution is obtained. It is assumed that the output of the filter can be modeled as separable first order autoregressive processes. Then, the close form solution is used as the initial solution for the iterative gradient search method. The mammogram image is filtered with the optimal filter. On the output of the filter, a simple thresholding separates mass and stellate lesions from the normal breast tissue. The authors use the same scheme for the detection of both mass lesions and stellate lesions, observing that they have similar characteristics. The false alarms produced by the system are eliminated by checking the size and the circularity of the detected regions. The authors conclude that this scheme is unable to detect mass and stellate lesions when (i) the lesion is surrounded by very dense tissue, (ii) the lesion has low intensity compared to the normal tissue

in the breast. The gradient search method has high computational costs. However, it needs to be computed only once for this problem and the calculation can be off-line (the parameters are obtained from a training set and these are used for all other detections).

In [22], mass lesions are detected using textual features derived from Spatial Grey Level Dependence (SGLD) matrices. The SGLD matrix $S_{(d,\theta)}$, for the image, x is defined in terms of a distance d and an angle θ . If there are k different grey levels, L_m ($m = 1, \dots, k$) in x , then the size of the $S_{(d,\theta)}$ matrix is $k \times k$. For each d and θ , the elements of the SDGL matrix, $S_{(d,\theta)}[m, n]$ give the number of times the pixels with grey level, L_m occur at a distance d and angle θ relative to the pixels with grey level, L_n ($1 \leq m, n \leq k$). From the SGLD matrix eight features are calculated which are correlation, entropy, energy (angular second moment), inertia, inverse difference moment, sum average, sum entropy, and difference entropy. SGLD matrices are calculated on mammogram images whose backgrounds are removed. Four different angles (0, 45, 90, 135) are considered and this produces 32 dimensional feature vector. This vector is averaged at four directions and an 8 dimensional feature vector is created. Next, the stepwise feature selection is performed to select the most discriminating subset of all available features. Selected features are used in *linear discriminant analysis* to detect masses on mammograms. The discriminant function, D , is a linear combination of the N feature variables, F_i [22]:

$$D = a_0 + \sum_{i=1}^N a_i F_i \quad (1.5)$$

where a_i are weights calculated from the input data during training. The performance of the detection is evaluated using a receiver operating characteristics (ROC) methodology [24]. In an ROC curve, true positive rate is plotted versus false positive detection rate. ROC curves are obtained for different detection thresholds. The area under the ROC curve is a measure of the performance of the scheme with a selected threshold value. In another work, the same features are fed into a convolutional neural network classifier for classification [24].

A multiresolution framework is also used for the detection of mass lesions in [12] and stellate lesions in [25]. In [12], Daubhecies' filter with four coefficients is used as the wavelet filter to obtain low-low subband images up to the fourth scale. In each scale SGLD matrices are calculated. Then, linear discriminant methodology described in Equation 1.5 is employed to differentiate between regions with tumor and healthy breast tissue.

In another multiresolution framework, Liu and Delp use a linear phase non-separable wavelet transform whose analysis filter, $h[m, n]$, is [25]:

$$h[m, n] = \begin{bmatrix} 0 & 0.125 & 0 \\ 0.125 & 0.5 & 0.125 \\ 0 & 0.125 & 0 \end{bmatrix} \quad (1.6)$$

The authors choose this filter because it does not introduce phase distortions or any bias in the horizontal and vertical directions. A two-dimensional quincunx subsampling is used. Then, at each resolution, four different features are extracted for every pixel: mean pixel gray level, standard deviation of pixel gray levels, standard deviation of edge histogram, standard deviation of folded edge orientations. For classification purposes a binary classification tree is employed. The main advantage of using a multiresolution framework is that abnormalities at different sizes can be more efficiently detected.

1.3 Outline of the Thesis

In this thesis, Higher Order Statistical (HOS) methods are developed for microcalcification detection on mammograms. In Chapter 2, the microcalcification modeling problem is discussed and it is concluded that deterministic microcalcification models introduced in [4, 40] are not sufficient to represent all types of microcalcifications as they can take different forms. Our modeling approach is statistical rather than deterministic. Furthermore, instead of modeling the microcalcifications on the original mammogram image, we model them in the bandpass images or in the multiresolution wavelet domain. Since microcalcifications are isolated single bright spots they appear as outliers in the bandpass images and in the wavelet domain images. Therefore, the problem of detecting microcalcification clusters is equivalent to detecting outlier clusters in these images. The linear and nonlinear filtering methods used in the first stage of the detection scheme are reviewed. Then, skewness and kurtosis based higher order statistical tests of the detection are introduced.

In Chapter 3, the regular structure of the mammogram image corresponding to the breast is removed by the adaptive filtering in the pre-processing stage. The method we propose makes use of two-dimensional (2-D) adaptive filtering and a HOS based Gaussianity test recently developed by Ojeda *et al.* for causal invertible time

series [54]. After adaptive linear prediction, a statistic of the prediction errors is computed to determine whether they are samples from a Gaussian distribution. Since microcalcifications are isolated bright spots, the prediction sequence deviates from Gaussianity around microcalcification locations. In Chapter 3, a new HOS based Gaussianity test is also developed which has a higher sensitivity than Ojeda *et al.*'s test. The concepts of the influence function and sensitivity curves are reviewed in this chapter and the sensitivity curves of the higher order statistical tests are derived. Our experiments with the mammogram database show that the proposed Gaussianity test gives better detection performance.

At the output of the HOS based detection scheme, parts of mammogram image with microcalcifications are marked as suspicious regions. Within these marked regions (or regions marked by other detection schemes), individual microcalcifications can be segmented through further processing. The shape and exact extent of microcalcifications can provide valuable information to radiologists in their diagnosis, and classification of the abnormalities as benign or malignant. They can also be used in three dimensional reconstruction of microcalcifications within the breast structure. In Chapter 4, several segmentation methods that use nonlinear and adaptive filtering based 'subband' decomposition structures, and a statistical outlier method are introduced. After the segmentation of individual microcalcifications, they can be superimposed on to the original mammogram image to get visually enhanced images. This chapter also describes mammogram enhancement operations.

While microcalcifications are regarded as an early sign of breast cancer, two types of lesions, namely masses and stellate lesions, are indicators of cancer. An additional tool has been developed for the detection of mass lesion boundaries on mammogram images. The method is based on active contour models, which are also known as snakes. In Chapter 5, the boundary detection method is explained and a comparison is made with another, recently developed, boundary detection method which is based on fuzzy-set pre-processing and region growing. Finally, conclusions and future work are given in Chapter 6.

Chapter 2

MICROCALCIFICATION DETECTION USING FILTERING AND HIGHER ORDER STATISTICS

As discussed in Chapter 1 clusters of fine, granular microcalcifications are an early sign of breast cancer in 30%-50% of the cases detected by mammography. In this chapter, microcalcification detection using filtering followed by Higher Order Statistical (HOS) analysis is described. In Sections 2.1 and 2.2, a stochastic characterization of microcalcifications is described and the database with which all the experiments are carried out is introduced, respectively. The mammogram image is processed by either a subband decomposition structure or a linear bandpass filter to enhance microcalcifications while suppressing the underlying breast structure. The filtered image is divided into overlapping square regions for statistical analysis. It is observed that in regions without microcalcifications, the distribution of pixel values is almost Gaussian whereas in regions with microcalcifications, the distribution is skewed due to outliers caused by microcalcifications. Therefore, skewness and kurtosis are estimated in the filtered image to identify suspicious regions. The use of nonlinear subband decomposition structures instead of linear subband decomposition as a pre-processing stage is also

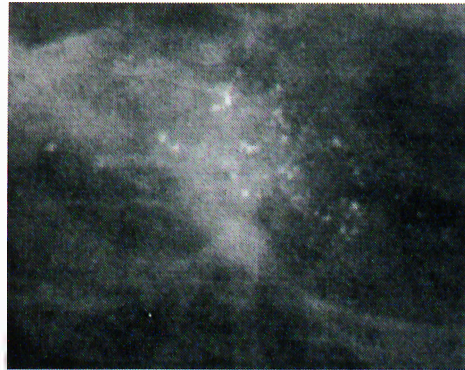


Figure 2.1: Part of a mammogram image containing microcalcification cluster.

investigated.

2.1 Characterization of Microcalcifications

The development of a microcalcification detection system starts with some characterization of microcalcifications [40]. Various authors have tried to model their shape, dimensions and their appearance on mammogram images. All of these approaches is deterministic.

Microcalcifications do not have a particular shape; their shapes vary from granular to rod-shaped. Morphologically, they can be classified as dust-like, worm-like, crushed stone, etc. [42]. Figure 2.1 shows part of a mammogram image containing a microcalcification cluster. Figures 2.2 and 2.3 give the cross sections of parts of two different mammogram images. In these figures, the arrows indicate the locations of microcalcifications. In these particular cases, microcalcifications are easy to locate due to their high contrast relative to the surrounding parenchymal tissues. However, there is no lower limit to the contrast difference and in some cases parts of the mammogram image can be brighter than microcalcifications in the mammogram image [20]. Therefore, a simple thresholding technique is not sufficient for the detection.

Strickland and Hahn model microcalcifications as circularly-symmetric Gaussian functions by looking at the average profile of 80 different microcalcifications [4]. However, this model cannot satisfactorily represent every type of microcalcification, especially those with non-regular shapes. Actually, the resultant profile can be thought

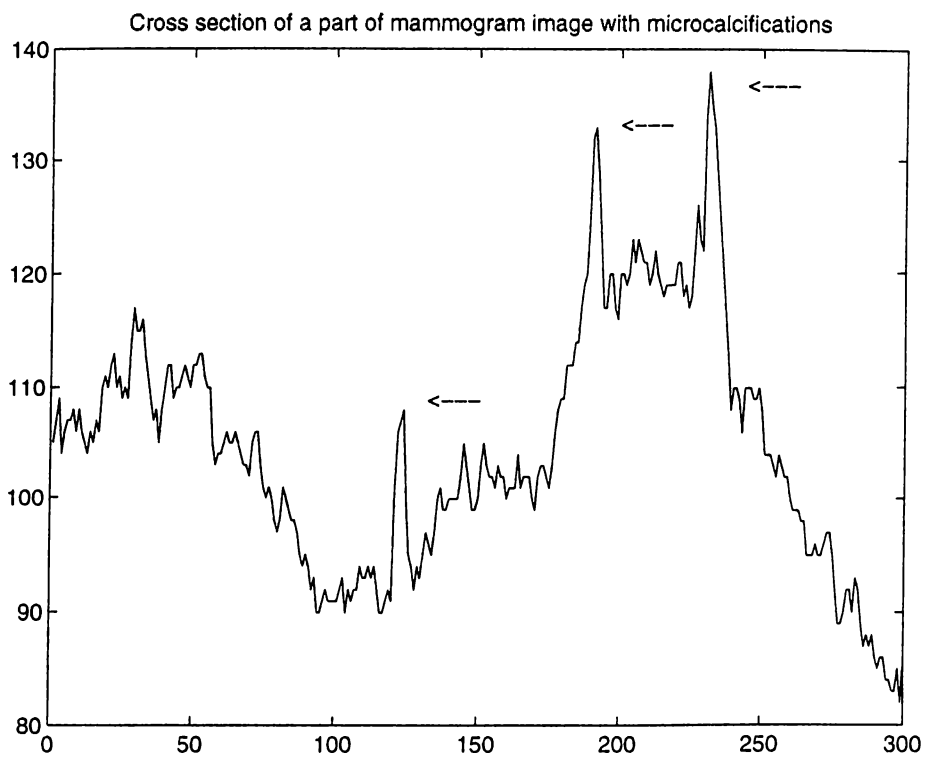


Figure 2.2: Cross section of a part of a mammogram image with microcalcifications. The locations of microcalcifications are indicated by arrows.

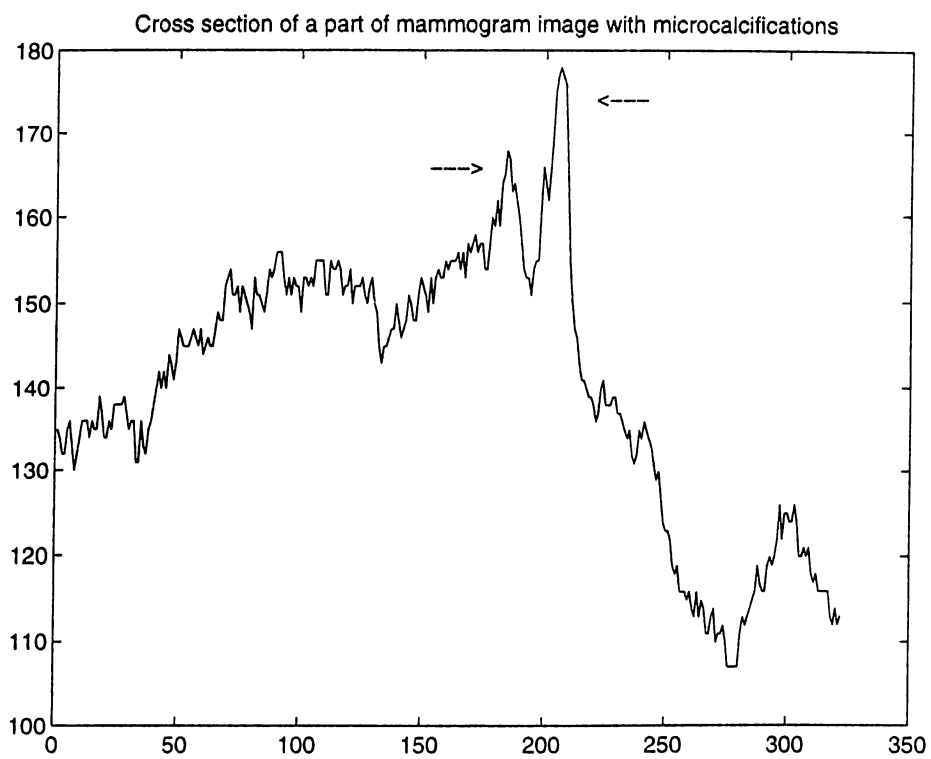


Figure 2.3: Cross section of a part of a mammogram image with microcalcifications. The locations of microcalcifications are indicated by arrows.

of a natural result of the central limit theorem. Since the authors average quite a large set of microcalcification profiles, it is natural to expect the average microcalcification to have a Gaussian distribution.

In another modeling attempt, Netsch describes microcalcifications as bright, circular spots and models them as cylinders of certain height and weight [40]. The following equation gives his model of a microcalcification located at $(0, 0)$:

$$x[m, n] = \begin{cases} C + C_0 & \text{if } m^2 + n^2 \leq \frac{D^2}{4} \\ C_0 & \text{otherwise} \end{cases} \quad (2.1)$$

where, $x[m, n]$ is the intensity of the microcalcification pixels, D is the size, C is the local contrast, and C_0 is the local background intensity. This model can also be criticized for being over-simplified and not taking into account various microcalcification shapes.

In our approach, we do not use a deterministic explicit form of a microcalcification model. Instead, we have a stochastic approach. This approach is motivated by the fact that microcalcifications appear as impulsive outliers in subband decomposed or bandpass filtered mammogram images. This observation has been verified by our experiments as well as by those of other researchers [4, 6]. Since an outlier is “an observation (or subset of observations) which appears to be inconsistent with the remainder of that set of data” [44], this information can be used in the detection process. The key idea is to model the microcalcification clusters in the subband images as outlier clusters instead of modeling them on the original mammogram image, and to use higher order statistics to find the locations of outlier clusters in the data.

Due to this modeling approach our detection scheme consists of two stages. In the first stage, the image is processed by a filter and in the second stage, the outliers in the processed image is detected by using HOS methods. In the next section we describe the mammogram image database that we use in our experiments. In Section 2.3 we describe the first stage of the detection scheme in which the breast image area is segmented and it is bandpass filtered to enhance microcalcifications. HOS based detection, the second stage, is described in Section 2.4.

2.2 Mammogram Database

We have carried out our experiments on mammogram images taken from a set digitized by Nico Karssemeijer of University Hospital Nijmegen, The Netherlands¹. The database is publicly available on the Internet [39] and is used by other researchers in the field [4, 40]. The database consists of 40 mammograms of 21 patients. Mediolateral oblique (side) and cranio caudal (top-down) views of patients are recorded with a Kodak MIN-R/SO177 screen/film combination. Both malignant and benign cases are included in the set.

Mammograms were digitized using a Eikonix 1412, 12 bits CCD camera with fixed calibration. The sampling aperture is 0.05 mm and the sampling distance is 0.1 mm. The size of the digital images is 2048 pixels by 2048 pixels. The images were corrected for inhomogeneity of the light source (Gordon planar 1417). Background pixel values (those with pixel values less than 15) were all set to a constant value. Each image is converted from 12 bits to 8 bits using an adaptive noise equalization technique, in which the noise due to film and digitization is equalized over all pixels.

For each mammogram image there is a ground truth file, in which the locations and the sizes of microcalcification clusters are marked. Individual microcalcifications are not marked in these ground truth images. These markings were recorded by two expert radiologists.

2.3 Pre-Processing of Mammogram Images

The aim of filtering the mammogram image is to remove the relatively smooth part of the image corresponding to normal breast tissue so that detection of microcalcifications is easier and the false-positive rate decreases. The pre-processing can be accomplished through either linear filters, adaptive filters or nonlinear filters. We investigate the performance of these filters in terms of their detection efficiency, false alarm rates and computational complexity. In Section 2.3.1 we describe a breast boundary detection algorithm. By carrying out the processing inside this boundary, computational complexity of the detection process is reduced. In Section 2.3.2, the bandpass linear filtering structure is explained. The filtered image is used by the statistical detection

¹Images were provided by courtesy of the National Expert and Training Centre for Breast Cancer Screening and the Department of Radiology at the University of Nijmegen, the Netherlands.

Mammogram Image

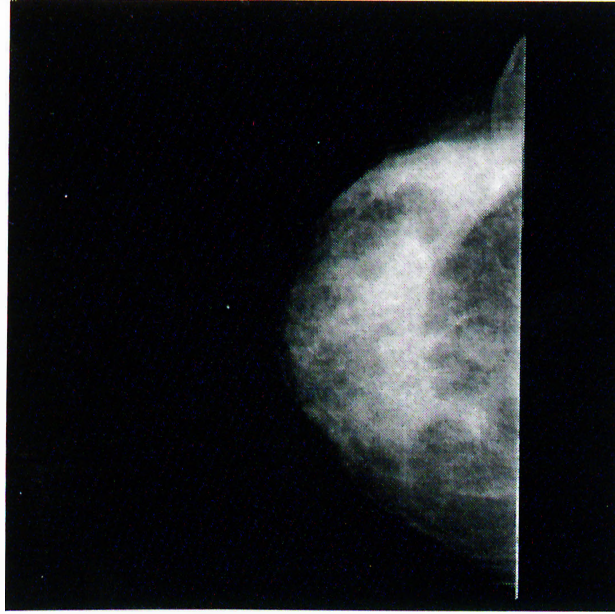


Figure 2.4: Typical mammogram image (cranio caudal view).

scheme which is explained in Section 2.4. Finally, Section 2.5 explains nonlinear ‘subband’ decomposition structures for the microcalcification detection.

2.3.1 Segmentation of Breast Region

Breast occupies only a relatively small part of the image area on a typical mammogram image. Executing the detection algorithms only within the breast area decreases the processing time significantly. Additionally, false positives obtained by the detection scheme due to markers in the image (the patient identification labels and letters to indicate the type of the view such as R, L, CC) and the sharp edge near the chest side are eliminated by the breast area segmentation.

Breast boundary is determined by using the projections which describe the extent of the breast area. The horizontal, $H[n]$, and vertical, $V[m]$, projections of a mammogram image are given as

$$H[n] = \frac{\sum_{m=1}^M x[m, n]}{M} \quad (2.2)$$

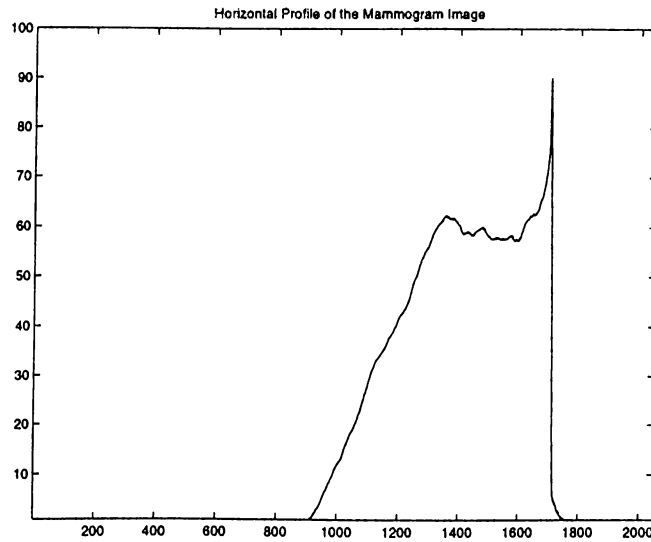


Figure 2.5: Horizontal profile of the mammogram image in Figure 2.4.

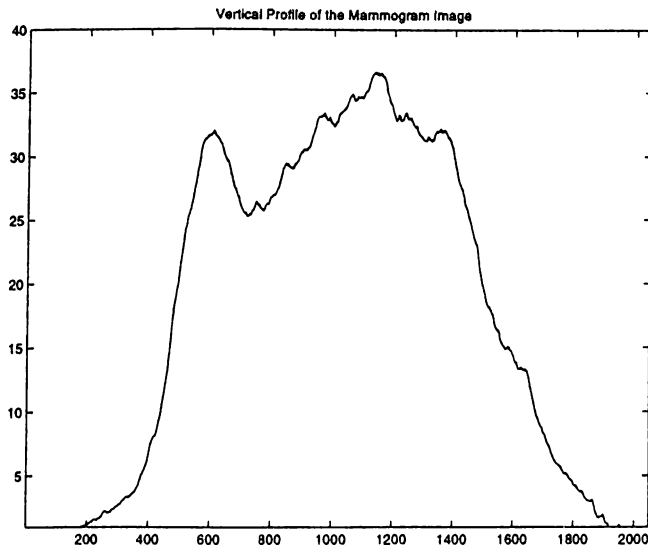


Figure 2.6: Vertical profile of the mammogram image in Figure 2.4.

$$V[m] = \frac{\sum_{n=1}^N x[m, n]}{N} \quad (2.3)$$

where $x[m, n]$ represents the pixel value of the digital mammogram image at the location (m, n) , and the image size is $M \times N$. For example, Figure 2.5 shows the horizontal and Figure 2.6 shows the vertical projections of the mammogram image in Figure 2.4 which shows cranio caudal (top-down) view of a breast image.

Applying a simple thresholding on these one-dimensional signals produces the corners of a rectangular region enclosing the actual breast area. Within this rectangular area, an adaptive iterative thresholding method can be employed to segment the actual breast area. As it is explained in the next chapter while discussing adaptive algorithm based detection schemes, some of the detection algorithms can work more efficiently, if realized within the segmented breast area.

In the adaptive iterative thresholding method, initially a threshold value is determined as the mid-value between the minimum pixel and the maximum pixel values. The choice of the middle value is not critical. Any value in between these extremes will do, however, such a choice may only affect the convergence speed of the algorithm depending on the values of the image pixels. For the mammogram images, one or two iterations are usually enough because the background region has an almost uniform low intensity (black).

Figure 2.7 shows the flowchart of the adaptive iterative thresholding algorithm. The image pixel values are divided into two regions by the initial threshold. One of the regions (say, black region) includes those pixels with values higher than the initial threshold and the other one (white region) contains all the other pixel values. The means of these black and white regions, m_w, m_b are calculated separately. The average of these two mean values constitutes the new threshold value, $T(k)$ for the algorithm. The iterative algorithm continues in this manner until the difference between two successive threshold values, $T(k) - T(k - 1)$ is less than a pre-determined number, A . As an example, Figure 2.8 shows the segmented breast area of the mammogram image in Figure 2.4, obtained by using the described adaptive iterative thresholding scheme.

Breast segmentation is not only useful for the detection schemes but also for the compression of mammogram images. For each patient, 4 mammogram images are recorded (mediolateral oblique and cranio caudal views of right and left breasts). Each mammogram image approximately occupies 6 Megabytes ($\approx 2048 \times 2048$ pixels \times 12 bits/pixel). Such a boundary delineation and breast segmentation can bring in significant storage savings even without using a further compression scheme, if only the segmented breast area is stored instead of the whole digital mammogram image.

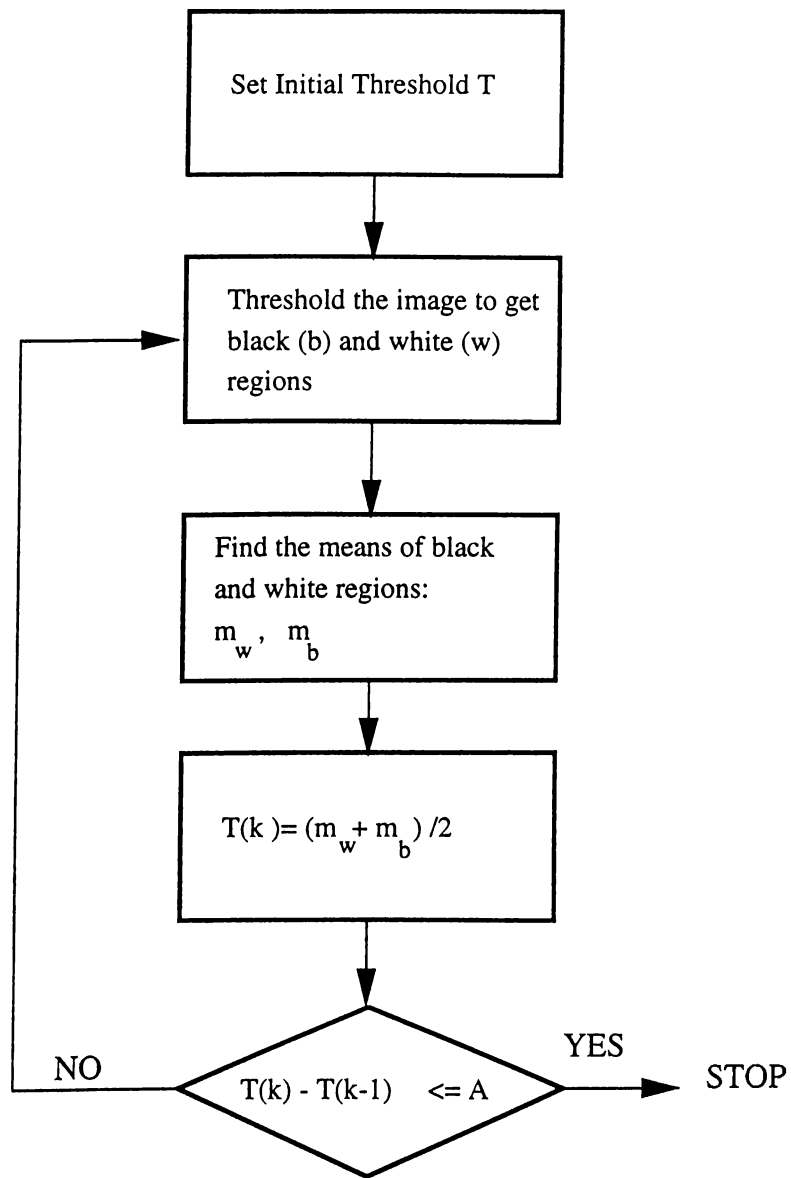


Figure 2.7: The adaptive iterative thresholding algorithm.

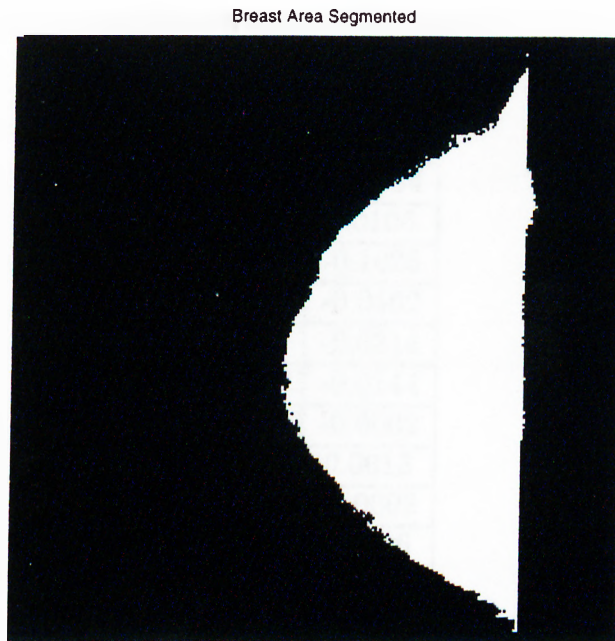


Figure 2.8: Segmented breast area of the mammogram image in Figure 2.4.

2.3.2 Linear Processing of Mammogram Images

In Chapter 1, while discussing the wavelet based multiresolution microcalcification detection schemes, we mention that these schemes are essentially equivalent to linear bandpass filtering. In Appendix A we show this equivalence. Instead of going through a subband decomposition and reconstruction stage, it is easier and much faster to implement the pre-processing using only linear filters. In our first experiments we examined the effectiveness of bandpass filtering in extracting microcalcifications while suppressing the background breast structure in mammogram images.

Our experiments with different mammogram images lead to the conclusion that a zero-phase bandpass filter with passband $\left[\frac{5\pi}{32}, \frac{3\pi}{4}\right]$ is effective for our detection scheme. A bandpass filter, h that approximates this constraint has the filter coefficients given in Table 2.3.2. This filter is designed by Parks-McClellan algorithm [41]. The frequency response of the filter is shown in Figure 2.9.

The two-dimensional filter with the passband $\left[\frac{5\pi}{32}, \frac{3\pi}{4}\right] \times \left[\frac{5\pi}{32}, \frac{3\pi}{4}\right]$ is constructed in a separable manner. This filter can be implemented in a multiresolution framework but the computational cost is not heavy, therefore there is not a pressing need for multiresolution processing.

n	h
0	0.6953
± 1	0.0681
± 2	-0.2334
± 3	0.0106
± 4	-0.1025
± 5	-0.0462
± 6	-0.0314
± 7	-0.0144
± 8	-0.0002
± 9	0.0013
± 10	-0.0002
± 11	0.0006

Table 2.1: Filter Coefficients

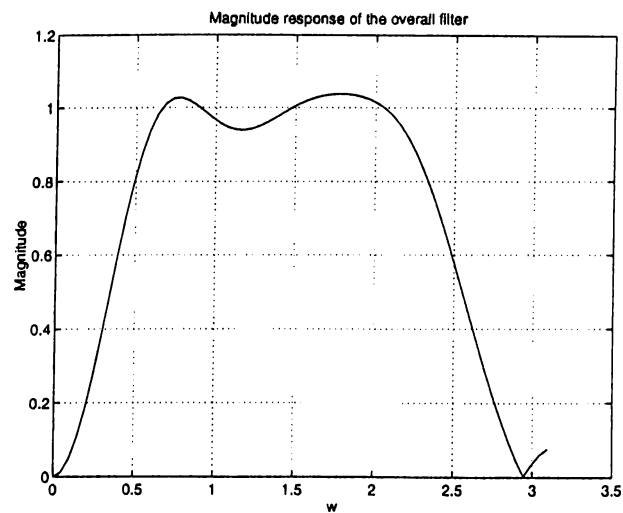


Figure 2.9: The magnitude response of the overall bandpass filter.

The choice of the bandpass filter has also an intuitive explanation. By blocking the low frequency components, the regions corresponding to the smooth breast tissue are eliminated, and the effect of noise is reduced by blocking the high frequency components.

2.4 Statistical Detection Method

As we pointed out earlier, detection of microcalcifications is carried out over the filtered mammogram image [30]. The bandpass filtered subimage is divided into overlapping square regions as shown in Figure 2.10. Figures 2.11-2.12 show the distribution of pixel values after linear bandpass filtering in regions with and without microcalcifications, respectively. The sizes of the regions are 100 pixel by 100 pixel. It is observed that the histograms of the bandpass filtered subimages are very close to the Gaussian distribution as shown in Figure 2.12.

If a region contains microcalcifications then due to the impulsive nature of microcalcifications the symmetry of the distribution of bandpass subimage coefficients is destroyed as shown in Figure 2.11. It is also evident that the tails of the distribution are heavier. *Skewness* and *kurtosis* are Higher Order Statistical (HOS) measures of the asymmetry and impulsiveness of the distribution [45]. The skewness and kurtosis values for Gaussian distributed random variables is zero. In the following section, these HOS based measures are reviewed. Therefore, a statistical test based on *skewness* and *kurtosis* is effective in finding regions with asymmetrical and heavier tailed distributions.

In our detection scheme, these HOS parameters are estimated in each square region. If a region has high positive skewness and kurtosis then it is marked as a region of interest. For instance, the skewness and kurtosis estimates of the distributions plotted in Figures 2.11 and 2.12 are shown in Table 2.2. Both the skewness and the kurtosis assume very small values in the healthy breast region, while they have high values in the region containing microcalcifications. The microcalcification detection scheme using these HOS based measures is described in Section 2.4.2.

	Skewness	Kurtosis
Microcalcifications (Linear Processing)	1.4716	6.0538
No microcalcification (Linear Processing)	0.1173	0.0854

Table 2.2: Skewness, $\hat{\gamma}_3$, and kurtosis, $\hat{\gamma}_4$ estimates of the data plotted in Figures 2.11 and 2.12.

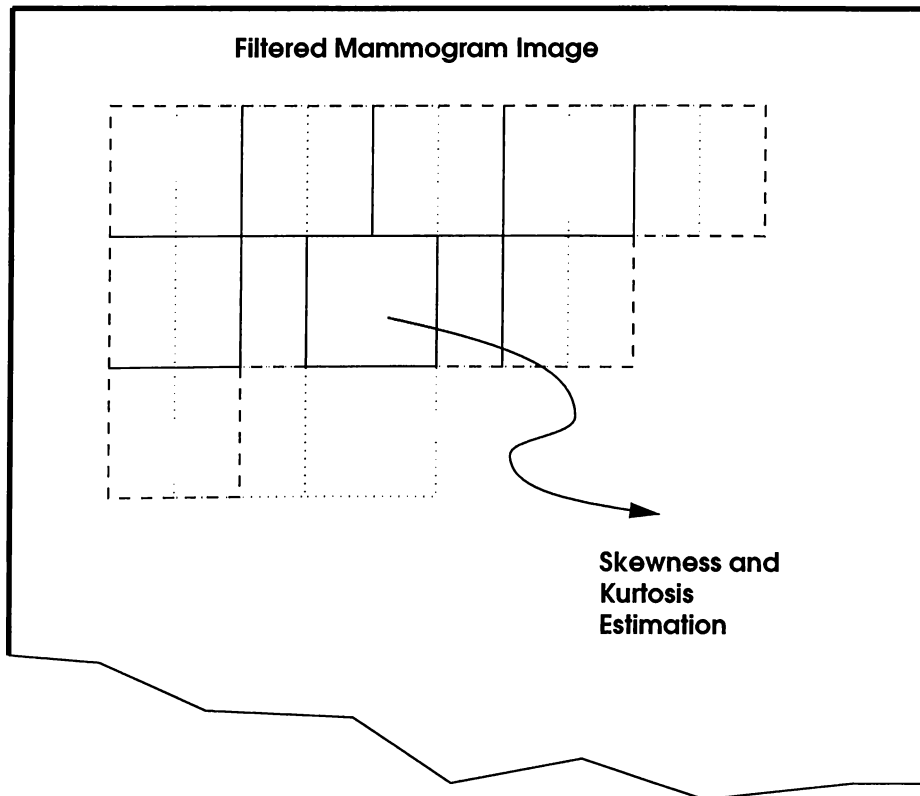


Figure 2.10: Skewness and Kurtosis are estimated in overlapping square regions.

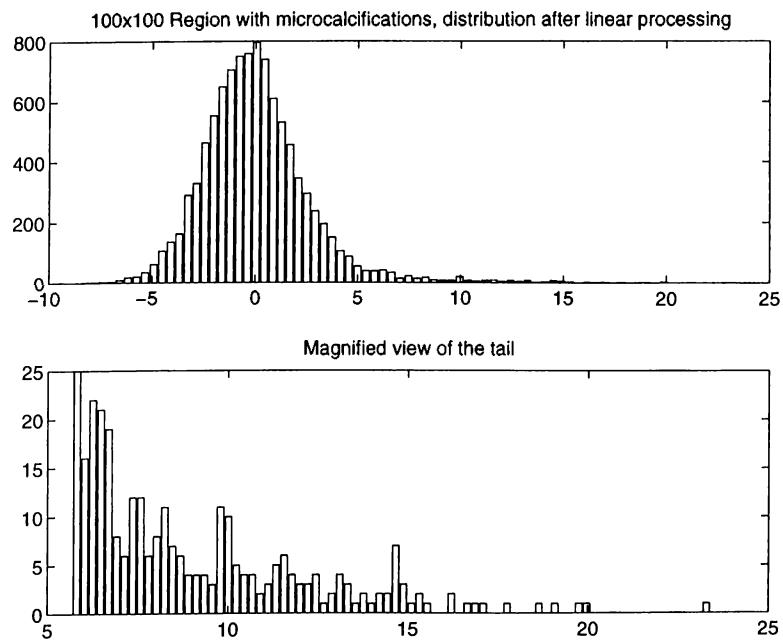


Figure 2.11: 100x100 region with microcalcifications, distribution after linear processing and magnified view of the tail.

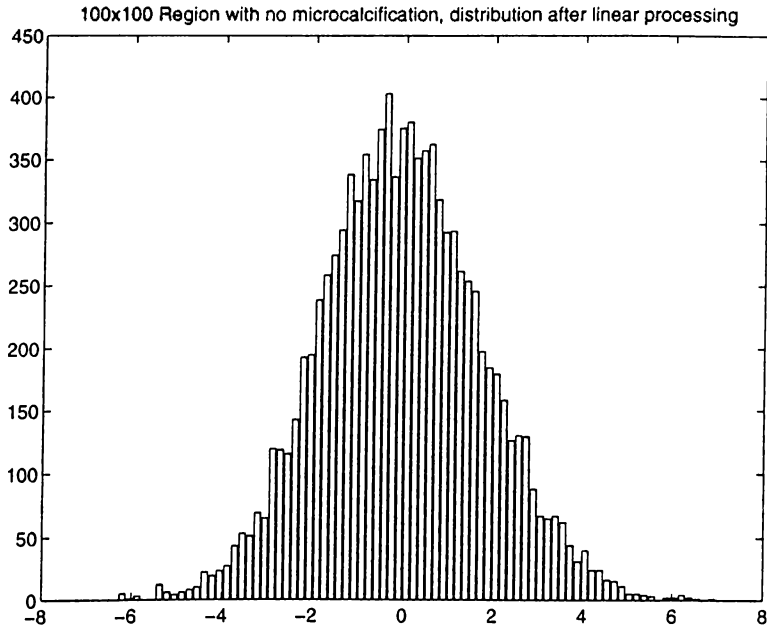


Figure 2.12: 100x100 region with no microcalcification, distribution after linear processing

2.4.1 HOS Measures: Skewness and Kurtosis

Skewness and kurtosis are third and fourth order HOS measures, respectively. For a random variable \mathbf{x} , the skewness is defined as [46],

$$\gamma_3 = \frac{E[(\mathbf{x} - E[\mathbf{x}])^3]}{(E[(\mathbf{x} - E[\mathbf{x}])^2])^{3/2}} \quad (2.4)$$

and it is a measure of the symmetry of the distribution. An estimate of the skewness is given by:

$$\hat{\gamma}_3 = \frac{\sum_{i=1}^N (x_i - \hat{\mu})^3}{(N-1)\hat{\sigma}^3} \quad (2.5)$$

where $\hat{\mu}$ and $\hat{\sigma}$ are the estimates of the mean and standard deviation over N observations x_i ($i = 1, \dots, N$).

Similarly, for a random variable \mathbf{x} the kurtosis is defined as

$$\gamma_4 = \frac{E[(\mathbf{x} - E[\mathbf{x}])^4]}{(E[(\mathbf{x} - E[\mathbf{x}])^2])^2} - 3 \quad (2.6)$$

and it is a measure of the heaviness of the tails in a distribution. An estimate of the kurtosis is given by:

$$\hat{\gamma}_4 = \frac{\sum_{i=1}^N (x_i - \hat{\mu})^4}{(N-1)\hat{\sigma}^4} - 3 \quad (2.7)$$

where $\hat{\mu}$ and $\hat{\sigma}$ are defined as before.

For the Gaussian distribution γ_3 and γ_4 are equal to zero:

$$\begin{aligned} E[(\mathbf{x} - E[\mathbf{x}])^3] &= E[\mathbf{x}^3 - 3\mathbf{x}^2\hat{\mu} + 3\mathbf{x}\hat{\mu}^2 - \hat{\mu}^3] \\ &= 0 \end{aligned} \quad (2.8)$$

$$\text{as } E[\mathbf{x}^3] = \hat{\mu}^3 + 3\hat{\sigma}^2\hat{\mu}.$$

The numerator of Equation 2.7 can be expressed as :

$$\begin{aligned} E[(\mathbf{x} - E[\mathbf{x}])^4] - 3(E[(\mathbf{x} - E[\mathbf{x}])^2])^2 &= E[\mathbf{x}^4 - 4\mathbf{x}^3\hat{\mu} + 6\mathbf{x}^2\hat{\mu}^2 - 4\mathbf{x}\hat{\mu}^3 + \hat{\mu}^4] - 3\hat{\sigma}^2 \\ &= 0 \end{aligned} \quad (2.9)$$

$$\text{as } E[\mathbf{x}^4] = \hat{\mu}^4 + 6\hat{\mu}^2\hat{\sigma}^2 + 3\hat{\sigma}^4.$$

2.4.2 HOS Based Detection

The detection problem can be posed as an hypothesis testing problem in which the null hypothesis, H_0 , corresponds to the case of no microcalcifications against the alternative H_1 :

- $H_0 : |\hat{\gamma}_3| < T_1 \text{ or } |\hat{\gamma}_4| < T_2$
- $H_1 : |\hat{\gamma}_3| \geq T_1 \text{ and } \hat{\gamma}_4 \geq T_2$

where T_1 and T_2 are experimentally determined thresholds.

In our first experiments, skewness and kurtosis values were estimated in original, bandpass and highpass filtered mammogram images. The aim was to determine the lower and upper bounds on these values in regions with and without microcalcifications

on mammograms. In this way, the threshold values of the hypothesis testing, T_1 , T_2 can be determined by analyzing a set of training images.

Tables 2.3–2.5 give the statistics of skewness and kurtosis estimates on original, bandpass, and highpass filtered images. These estimates are made from 100 blocks of size 30 pixels \times 30 pixels with microcalcifications and 100 blocks of the same size without microcalcifications on a total of five images. This constitutes our training set. By examining Tables 2.3–2.5 one can conclude that skewness and kurtosis parameters are not

Estimate	Mean	Minimum value	Maximum value
Skewness	0.7179	-0.7598	3.2354
Kurtosis	1.3759	-1.1269	14.122

(a)

Estimate	Mean	Minimum value	Maximum value
Skewness	0.3044	-0.7118	1.5806
Kurtosis	0.1650	-1.2262	4.5514

(b)

Table 2.3: Skewness and Kurtosis estimates on the original image, (a) regions with microcalcifications, (b) regions without microcalcifications.

Estimate	Mean	Minimum value	Maximum value
Skewness	1.5824	0.5507	3.4023
Kurtosis	5.6282	0.9906	18.5437

(a)

Estimate	Mean	Minimum value	Maximum value
Skewness	0.0767	-0.2655	0.5195
Kurtosis	0.0773	-0.3968	0.8561

(b)

Table 2.4: Skewness and Kurtosis estimates on the bandpass filtered image, (a) regions with microcalcifications, (b) regions without microcalcifications.

Estimates	Mean	Minimum value	Maximum value
Skewness	1.3993	0.4385	2.8970
Kurtosis	4.5934	0.8216	17.864

(a)

Estimates	Mean	Minimum value	Maximum value
Skewness	0.0800	-0.2203	0.4823
Kurtosis	0.0550	-0.3227	0.9218

(b)

Table 2.5: Skewness and Kurtosis estimates on the highpass filtered image, (a) regions with microcalcifications, (b) regions without microcalcifications



Figure 2.13: Detection scheme output, (a) part of a mammogram image, (b) regions with microcalcifications as indicated by the detection scheme.

indicative of microcalcifications on original images whereas they are most discriminating in the detection for bandpass filtered images. For the bandpass images neither skewness nor kurtosis estimates had an overlapping region under hypotheses H_0 and H_1 in this data set.

Since, the HOS parameters show the best discriminating power in the bandpass filtered images, only these images are utilized in the first stage of the detection scheme. The thresholds, T_1 , T_2 for skewness $\hat{\gamma}_3$ and kurtosis $\hat{\gamma}_4$ are determined to be 0.51 and 0.85, respectively. These threshold levels are chosen slightly below the maxima of the skewness and kurtosis values of the no microcalcification case so that none of the regions with microcalcifications is missed.

Our detection scheme detected all the 105 microcalcification clusters with an average of 3.3 false alarms per mammogram image in all mammogram images in the Nijmegen database. In the standard practice, the training and the test cases must be separate. However, in this thesis, as the estimations are done over a relatively very small area on the mammogram image, we prefer to include all the images in our detection performance tests. This false alarm rate is better than the microcalcification detection scheme in [4] in which a wavelet based subband decomposition and thresholding are used on the same database to get 8 false alarms per image. However, our false alarm rate can be further reduced by introducing other HOS based statistical measures and adaptive prediction which does a better job of removing the effect of healthy regions corresponding to the breast tissue. In Figure 2.13(a) a part of a mammogram image which contains a cluster of microcalcifications is shown. Figure 2.13 (b) illustrates the result of our detection algorithm; the black squares indicates suspicious regions.

2.5 Nonlinear Subband Decomposition Structures

Nonlinear filters such as median type filters have been previously used for the detection of microcalcifications by Chan *et.al.* [2]. In this work, the effects of linear and nonlinear filters and their region of support on the detection and enhancement of microcalcifications are investigated through ROC studies. A median filter with a 9×9 support is found to be most effective on mammogram images with simulated microcalcifications in [2]. However, such a median filter cannot be effective in eliminating all of the microcalcifications on the mammogram images of Nijmegen database as we discuss later in this section.

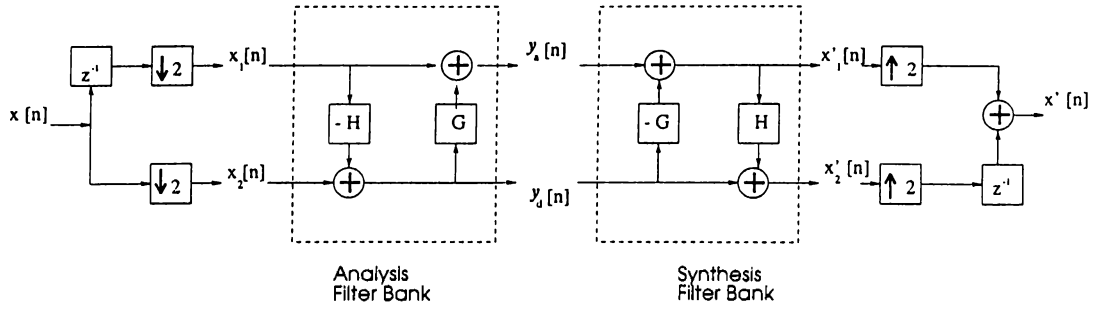


Figure 2.14: Nonlinear Subband Decomposition Structure.

We also investigated the use of nonlinear filters and filterbanks in the analysis of mammogram images for microcalcifications detection. Recently, the ‘subband’ decomposition using nonlinear filters have been proposed and used in image coding [33]–[36]. We will use this filterbank structure in both detection and enhancement of microcalcifications in mammogram images.

In Figure 2.14, the block diagram of the nonlinear subband decomposition structure used by Hampson and Pesquet is shown [36]. This structure is based on the *lifting scheme* of Sweldens [37]. It is obtained by replacing linear filters of the lifting filter bank by nonlinear operators H and G . The approximate signal y_a , and the detail signal y_d are obtained from the input signal $x[n]$ as follows [36]:

$$y_a[n] = x_1[n] + G(y_d)[n] \quad (2.10)$$

$$y_d[n] = x_2[n] - H(x_1)[n] \quad (2.11)$$

where $x_1[n] = x[2n - 1]$, $x_2[n] = x[2n]$ which are the odd and even samples of the input $x[n]$, respectively.

The corresponding synthesis equations are:

$$x'_1[n] = y_a[n] - G(y_d)[n] \quad (2.12)$$

$$x'_2[n] = y_d[n] + H(x'_1)[n] \quad (2.13)$$

In this structure, perfect reconstruction is achieved as $x'_1[n] = x_1[n] + G(y_d)[n] - G(y_d)[n]$ and $x'_2[n]$ turn out to be odd and even samples of the original signal, $x[n]$, respectively.

In the mammogram image analysis, H is chosen as a median filter. The output of the median filter is the middle value of the ordered set of pixel values within a window. A median filter with a proper Region of Support (ROS) eliminates all impulsive type structures in an image. As microcalcifications exhibit impulsive character, a median filter with suitable ROS can eliminate these abnormalities from the mammogram image. The detail signal, $y_d[n]$ in Equation 2.10 is obtained by subtracting the median filtered image from the original image. Therefore, we expect that mainly microcalcifications are observed in $y_d[n]$. The choice and characteristics of the nonlinear G filter will be explained in Section 4.2.2 while discussing the segmentation and enhancement of microcalcifications.

Figure 2.15 shows the outputs at different stages of the nonlinear processing. Figure 2.15 (a) illustrates an original line of mammogram image which contains a microcalcification. Figure 2.15 (b) illustrates the same line of image after median type nonlinear filtering. As can be observed in this figure, the output of the median filter mainly represents the relatively smooth part of the mammogram image corresponding to the normal breast tissue. Figure 2.15 (c) displays the difference between the original line of image and the median filter output. HOS based microcalcification detection is carried out in the detail signal, $y_d[n]$.

In the subband decomposition structure, the signal is downsampled. However, downsampling operation can eliminate some of the microcalcifications if the resolution of the scanner is not high enough. For example, the smallest microcalcification with $0.1mm \times 0.1mm$ dimensions will appear as a $1pixel \times 1pixel$ region on the digital mammogram image if the resolution of the scanner is $100\mu m$. Therefore, either the resolution of the scanner must be increased or downsampling operation should not be carried out. The advantage of downsampling in the multirate processing is the reduced computational complexity.

The nonlinear subband decomposition structure illustrated in Figure 2.14 can be extended to two dimensions in a straightforward manner [33, 34]. In two dimensions, the detail image, $y_d[m, n]$ can be obtained by simply subtracting the median filtered image from the original image. In this detail image microcalcification detection can be carried out. The image, $y_d[m, n]$ is divided into overlapping square regions as explained in Section 2.4, and in each square region skewness and kurtosis values are estimated. Figures 2.16 and 2.17 show the distributions of the detail image pixel values. As in the linear filtering case, the presence of microcalcifications disturbs the Gaussian nature of

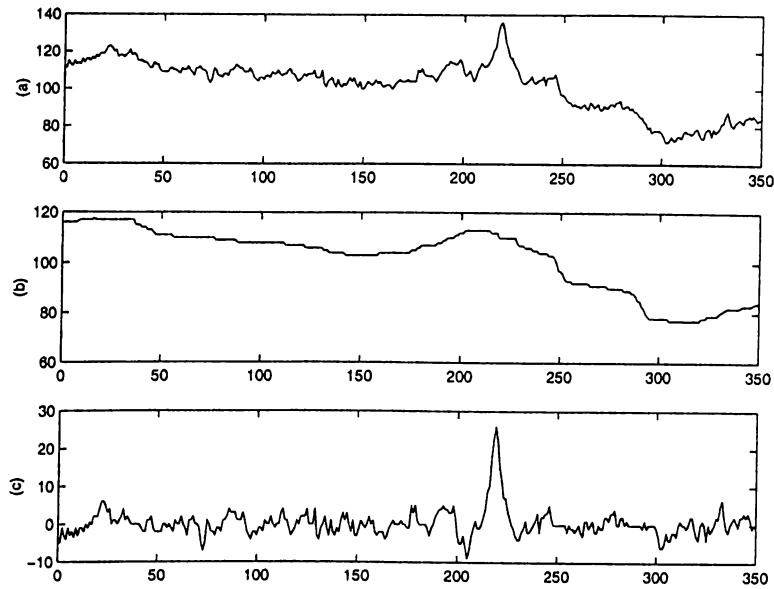


Figure 2.15: Median filter based nonlinear processing (a) A line extracted from the mammogram image (b) the median filter output (c) the difference between the signals in (a) and (b).

the distribution. Table 2.6 shows the skewness and kurtosis estimates of the distributions in Figures 2.16 and 2.17.

Table 2.7 gives the statistics of skewness and kurtosis estimates on the detail images, $y_d[m, n]$, in nonlinear decomposition structure. The nonlinear filter, H is chosen as a median filter with an 21×21 square ROS. Parameters are estimated from a data set consisting of 100 blocks of size 30 pixels \times 30 pixels with microcalcifications and from 100 blocks of the image data with the same size without microcalcifications on a total of five images. Estimated skewness and kurtosis values in Tables 2.4 and 2.7 are very similar. These estimates as well as our other experiments with different mammograms indicate that similar results can be obtained both in linear and nonlinear processing cases. Therefore, a HOS based detection is also possible after the nonlinear processing.

	Skewness	Kurtosis
Microcalcifications (Nonlinear Processing)	1.5476	5.8609
No microcalcification (Nonlinear Processing)	0.0968	-0.0983

Table 2.6: Skewness and Kurtosis estimates of the distributions in Figures 2.16 and 2.17.

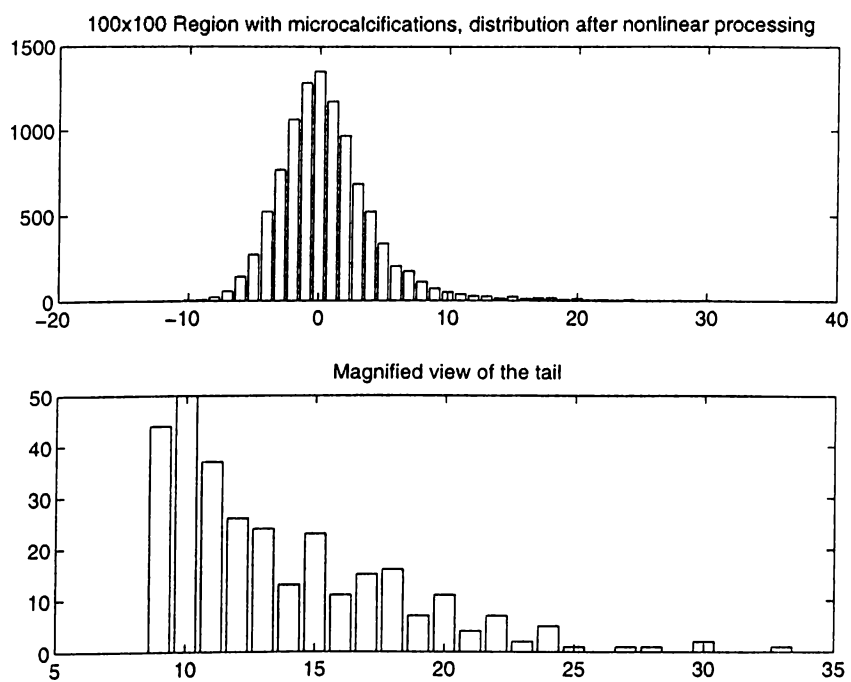


Figure 2.16: 100x100 region with microcalcifications, distribution after nonlinear processing and magnified view of the tail.

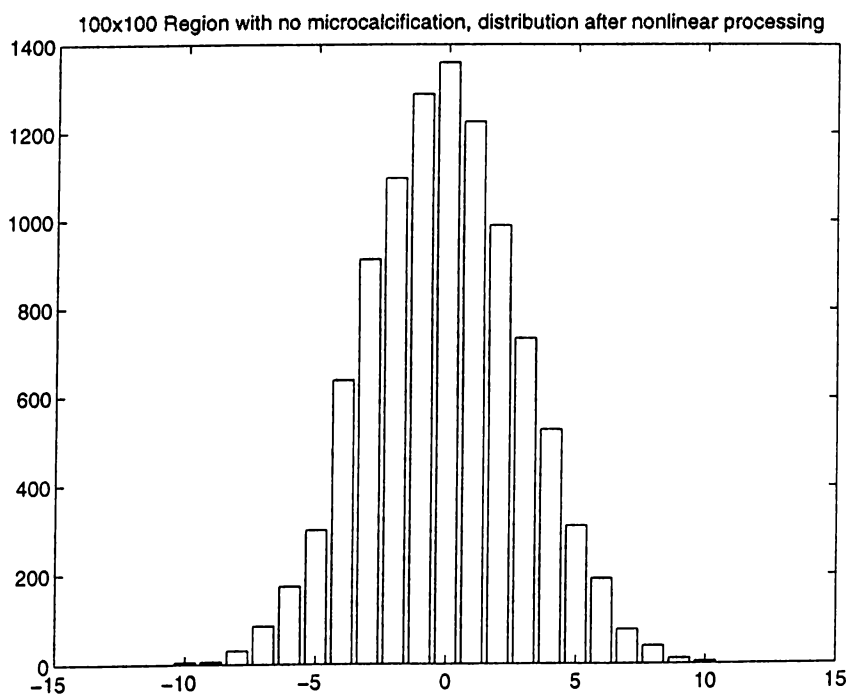


Figure 2.17: 100x100 region with no microcalcification, distribution after nonlinear processing

Estimate	Mean	Minimum value	Maximum value
Skewness	1.7255	1.1446	2.1574
Kurtosis	4.9720	2.0837	19.1673

(a)

Estimate	Mean	Minimum value	Maximum value
Skewness	0.0520	-0.4485	0.5432
Kurtosis	-0.0330	-0.5285	0.6725

(b)

Table 2.7: Skewness and Kurtosis Estimates on the detail image after nonlinear subband decomposition, (a) regions with microcalcifications, (b) regions without microcalcifications.

The ROS of the median filter should be determined in such a way that the median filtered image should not contain any microcalcification as shown in Figure 2.15 (b). In order to achieve this, the image scanning rate and the sizes of microcalcifications should be taken into account. In general, in order to eliminate all impulsive structures of maximum width w , the width of the median filter should be chosen as $2 \times w + 1$. The maximum size of a microcalcification in our database can be $10 \text{ pixels} \times 10 \text{ pixels}$ ($10 = 1 \text{ mm} / 100\mu \text{ m}$). The median filter is designed to eliminate all these abnormalities while retaining the regular breast structure. Therefore, in our application, H in Equation 2.10 is chosen as a median filter with an 21×21 square ROS in accordance with the dimensions of the microcalcifications ($21 = 2 \times 10 + 1$). The 9×9 choice suggested in [2] will not be effective in the Nijmegen database. Only some of the microcalcifications will be completely removed. Furthermore, the simple thresholding of the difference image will produce omissions of some of the microcalcifications due to the partial removal of the microcalcifications.

The median filter with a support region containing N samples requires ' $2N$ comparisons' to produce an output sample. On the other hand, a linear phase FIR filter requires $N/4$ multiplications. We found out that implementing the median filter is relatively slower than linear filtering in a general purpose computer. Therefore, only linear filtering is performed in the pre-processing stage. However, the nonlinear filtering structure can be effectively used in microcalcification segmentation and mammogram

image enhancement as will be explained in Chapter 4. As the processing is only over detected regions and not the entire image, the computational costs do not present a problem.

Our HOS based microcalcification detection algorithm drastically reduces the false alarm rate compared to simple thresholding based methods. This is due to our statistical modeling approach. Some pixels may accidentally exceed the simple threshold in regions corresponding to healthy breast tissue and this may cause false alarms in the previous approaches [4]. On the other hand, Gaussian modeling can accommodate such outliers in the tails of the distribution. Whenever the number of outliers increases in a region, the tails of the distribution become heavier and this means that the distribution deviates from Gaussian, thus microcalcifications may be present in the region.

Chapter 3

MICROCALCIFICATION DETECTION USING ADAPTIVE FILTERING AND HIGHER ORDER STATISTICAL TESTS

Linear and nonlinear subband decomposition structures combined with higher order statistical measures, skewness and kurtosis, constitute an effective framework for the microcalcification detection problem. In this chapter, this problem is investigated within a different framework which involves adaptive filtering. The adaptive filter is used to predict the breast tissue structure in the mammogram image. It is assumed that regular breast tissue can be effectively predicted by an adaptive predictor and unpredictable pixels correspond to the microcalcifications which are physically different from the breast tissue. Therefore, it is expected that the microcalcifications produce outliers in the prediction error image.

Recently, Ojeda et. al. use a Gaussianity test based on HOS to detect model changes of stationary time series [54]. This test uses the second and third order parameters. We also investigated the use of this test in this chapter instead of skewness and kurtosis. We analyzed the Ojeda's test using influence function approach and based on this approach we developed another statistical test which has higher sensitivity to outliers. This is

achieved by designing the new test using second and fourth order statistical parameters.

3.1 2-D Adaptive Prediction based Tests for Microcalcification Detection

The linear and nonlinear filtering based methods discussed in Chapter 2 are in a way *ad hoc* methods. The idea of using a fixed linear or a nonlinear filter on the entire image may not be as efficient as an adaptive filter which can update itself to changing conditions on the mammogram image. We also experimentally observed that adaptive filtering based Gaussianity tests provide a more robust framework for the microcalcification detection [31, 32]. The method we propose makes use of two-dimensional (2-D) adaptive filtering and a Gaussianity test recently developed by Ojeda, Cardoso and Moulines for causal invertible time series [54] (this test will be called the OCM test in short, hereafter). Similar to the methods described in Chapter 2, the image is analyzed block by block. After adaptive linear prediction, a statistic of the prediction errors is estimated in the current block to determine whether the samples correspond to a Gaussian distribution. The prediction error sequence exhibits Gaussian behavior in the normal breast tissue. Since microcalcifications are isolated bright spots, the prediction sequence deviates from Gaussianity around microcalcification locations. As before, the regions with high deviations are marked as suspicious regions.

In Section 3.1.1, the adaptive filtering concept is reviewed. The extension of the one dimensional adaptive filtering structure to two dimensions is explained in Section 3.1.2. The OCM Gaussianity test is introduced in Section 3.1.3. Experimental results obtained by utilizing the two dimensional adaptive filtering and the OCM test is given in Section 3.1.4.

3.1.1 Adaptive Filtering

In many signal processing applications, the signal is processed without utilizing any feedback information. The matched filter is an example. The frequency response or the transfer function of adaptive filters, on the other hand, is updated according to the nature of the input signal [56]. Adaptive filtering has found many applications in various

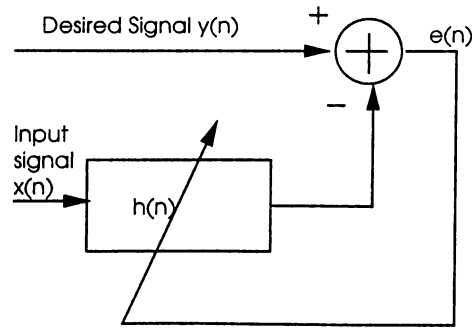


Figure 3.1: Adaptive filtering structure.

areas of signal processing and communication since 1960s, after Lucky designed a zero-forcing equalizer to compensate for distortion in data transmission systems [57]. In this section, we review the basic adaptive filtering concepts and introduce our notation.

The adaptive filter adjusts its coefficients according to the input statistics. The structure of a typical adaptive filter is illustrated in Figure 3.1. The output of the linear finite impulse response (FIR) filter can be written as the convolution of the input sequence \mathbf{x} and the impulse response of the adaptive filter \mathbf{h} .

$$\hat{y}[n] = \sum_{i=0}^{N-1} h[i]x[n-i] \quad (3.1)$$

or in the matrix form

$$\hat{\mathbf{y}} = \mathbf{h}^T \mathbf{x} \quad (3.2)$$

where $\mathbf{h} = [h[0] \ h[1] \ \dots \ h[N-1]]$ and $\mathbf{x} = [x[n] \ x[n-1] \ \dots \ x[n-N+1]]$.

The error signal, $e[n]$, is the difference between the estimated output, $\hat{y}[n]$ and the desired signal, $y[n]$.

$$e[n] = y[n] - \hat{y}[n] \quad (3.3)$$

The mean square error (MSE) is defined as

$$\xi[n] = E[e^2[n]] \quad (3.4)$$

Substituting Equations 3.2 and 3.3 into the MSE equation yields

$$\xi[n] = E[y^2[n]] + \mathbf{h}^T \phi_{xx} \mathbf{h} - 2\mathbf{h}^T \phi_{xy} \quad (3.5)$$

where ϕ_{xx} and ϕ_{xy} are the autocorrelation and cross correlation matrices, respectively. The MSE can be minimized to get the optimum \mathbf{h} filter, \mathbf{h}_{opt} .

$$\mathbf{h}_{\text{opt}} = \phi_{xx}^{-1} \phi_{xy} \quad (3.6)$$

In the least mean squares (LMS) algorithm [56], instead of calculating ϕ_{xx} and ϕ_{xy} , an iterative procedure is followed:

$$\mathbf{h}_{k+1} = \mathbf{h}_k + \mu \mathbf{x}_k e[k] \quad (3.7)$$

where μ is the adaptation constant.

3.1.2 2-D Adaptive Filtering

For the microcalcification detection problem, we use a 2-D Least Mean Square (LMS) adaptive filter in the prediction step. Recently, Ffrench *et. al.* independently proposed the use of 2-D adaptive filters for enhancement of mammogram images so that microcalcification locations are brighter than the regular breast tissue [50]. Figure 3.2 illustrates the adaptive filtering scheme in two dimensions. The adaptive filter predicts an image pixel $x[m, n]$ at location (m, n) as a weighted average of pixels in its region of support.

The region of support, \mathcal{R} , of the filter is chosen as the pixels surrounding the pixel to be predicted as shown in Figure 3.3. The predicted value $\hat{x}[m, n]$ is given as

$$\hat{x}[m, n] = \sum_{\substack{k = -n_1 \\ (k, l) \neq (0, 0)}}^{n_1} \sum_{l = -n_2}^{n_2} w_{(m,n)}[k, l] x[m - k, n - l], \quad m = 0, \dots, N_1 - 1, \quad n = 0, \dots, N_2 - 1 \quad (3.8)$$

where x is the input image of size $N_1 \times N_2$, $w_{(m,n)}$ are the weight values at (m, n) , and $(2n_1 + 1) \times (2n_2 + 1)$ is the size of the region of support, \mathcal{R} of the adaptive filter.

The prediction error at pixel location (m, n) is computed as

$$e[m, n] = \hat{x}[m, n] - x[m, n] \quad (3.9)$$

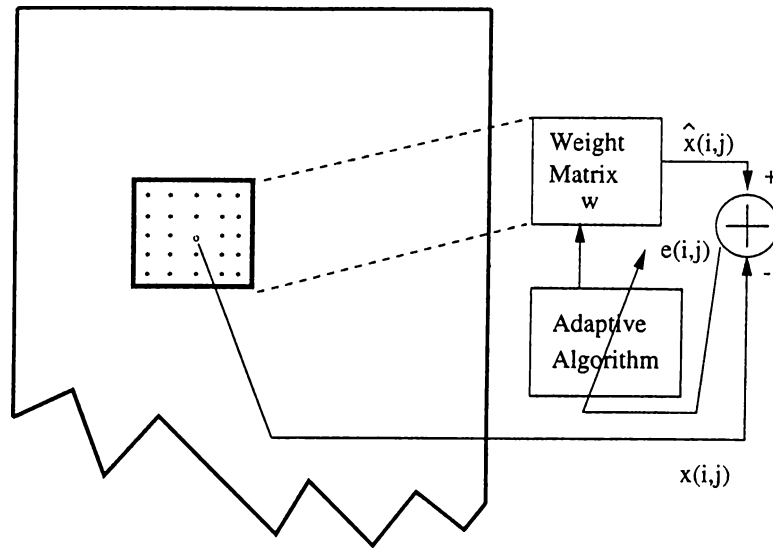


Figure 3.2: 2-D adaptive filter structure.

At each iteration the weights $w_{(m,n)}[k, l]$ are adapted using a two-dimensional LMS-type adaptation algorithm:

$$w_{(m+1,n)}[k, l] = w_{(m,n)}[k, l] + \mu \times e[m, n] \times x[k, l] \quad (3.10)$$

where $(k, l) \in \mathcal{R}$, the region of support, and μ is the adaptation constant. The filter weights are adapted using this equation while processing the image in the horizontal direction. In the vertical direction, the weight $w_{(m,n+1)}[k, l]$ is used instead of the weight $w_{(m+1,n)}[k, l]$. Figure 3.4 (a) shows part of a mammogram image containing a microcalcification cluster. This image is filtered by a two dimensional adaptive filter. Figure 3.4 (b) displays the error image, $e[m, n]$ obtained after the adaptive filtering. The detection is performed over this error image.

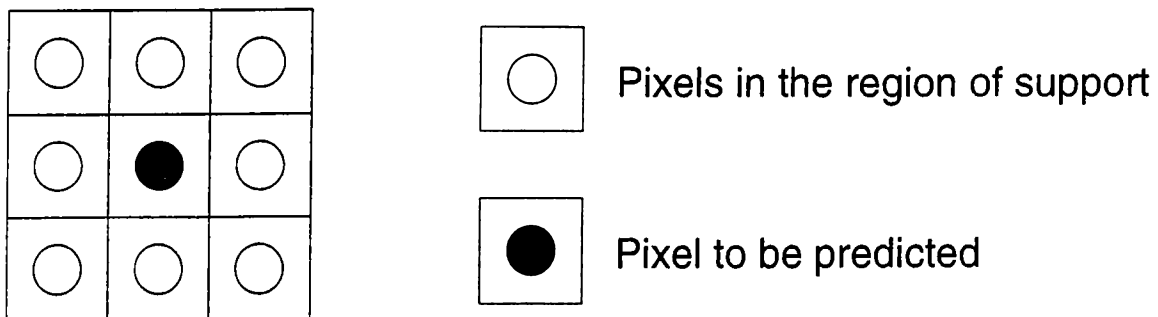


Figure 3.3: Region of support (ROS) of the adaptive filter. ROS is “anticausal.”

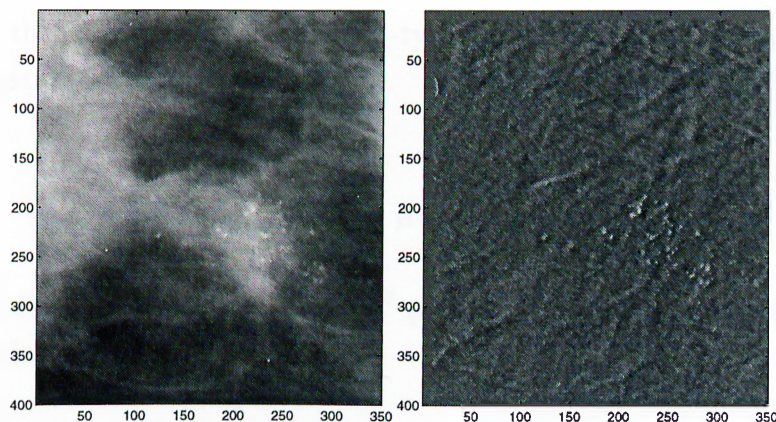


Figure 3.4: (a) Part of a mammogram image containing a microcalcification cluster (b) The error image obtained after the 2-D adaptive filtering

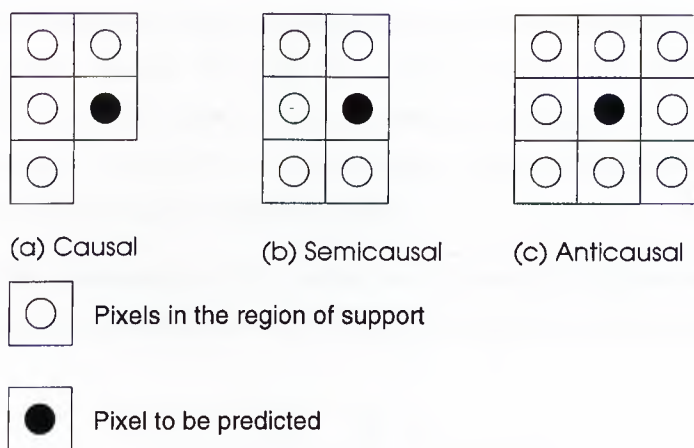


Figure 3.5: Causal, semicausal and noncausal finite prediction windows.

The chosen region of support, \mathcal{R} , is anticausal. Figure 3.5 illustrates causal, semicausal and anticausal finite prediction windows for adaptive filtering and linear predictions in two dimensions. Our experimental studies show that the best detection results are obtained by using anticausal regions of support similar to the fixed nonlinear filters. The region of support size should be chosen in accordance with the dimensions of microcalcifications on the mammogram. As we discuss in Section 2.5, the extent of the ROS is determined by the resolution of the scanner.

In our work, the original mammogram image is processed row by row as shown in Figure 3.6. This type of zig-zag scanning prevents false jumps in the error values, that may occur at the end of the rows. Therefore, there is a smooth transition and the convergence problem is not encountered.

Instead of the two-dimensional LMS-type adaptation, a normalized LMS-type (NLMS) adaptation can also be applied. The NLMS is defined by the following equation [51]:

$$w_{(m,n)}[k, l] = w_{(m,n)}[k, l] + \mu \times e[m, n] \times \frac{x[k, l]}{\sum_k \sum_l x[k, l]^2} \quad (3.11)$$

where the normalization factor $\sum_k \sum_l x[k, l]^2$ provides assumed convergence, if the update parameter satisfies, $0 < \mu < 2$.

3.1.3 Gaussianity Test

It is experimentally observed that in regions with no microcalcifications the Gaussian distribution is a good model for $e[m, n]$. In regions with microcalcifications, on the other hand, the distribution is non-Gaussian because of the impulsive nature of microcalcifications. Therefore, a Gaussianity test can be used to detect regions containing microcalcifications in mammograms.

We use the OCM Gaussianity test based on the sample estimates of the first three moments I_1, I_2, I_3 of the prediction errors [55]. Estimates of the moments are given by:

$$I_1 = \frac{1}{M \times N} \sum_{m=1}^M \sum_{n=1}^N e[m, n] \quad (3.12)$$

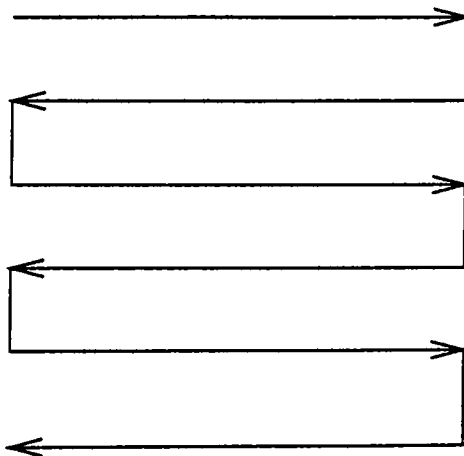


Figure 3.6: Scanning directions in adaptive filtering.

$$I_2 = \frac{1}{M \times N} \sum_{m=1}^M \sum_{n=1}^N e^2[m, n] \quad (3.13)$$

$$I_3 = \frac{1}{M \times N} \sum_{m=1}^M \sum_{n=1}^N e^3[m, n] \quad (3.14)$$

where, $e[m, n]$'s ($m = 1, \dots, M$, $n = 1, \dots, N$) are individual error values at the location (m, n) as calculated in Equation 3.9 and $M \times N$ is the total number of error image pixels in the square region ($M = N = 30$ in our experiments). The parameters, I_1, I_2, I_3 converge to the following values as M, N go to infinity under the ergodicity assumption:

$$I_1 \rightarrow \mu \quad (3.15)$$

$$I_2 \rightarrow \sigma^2 + \mu^2 \quad (3.16)$$

$$I_3 \rightarrow \mu^3 + 3\sigma^2\mu \quad (3.17)$$

where μ and σ^2 denote the mean and the variance of the error image e , respectively. With these limit values, the test statistic

$$h(I_1, I_2, I_3) = I_3 - 3I_1(I_2 - I_1^2) - I_1^3 \quad (3.18)$$

is equal to zero (in the limit) for Gaussian distributed sequences:

$$\begin{aligned} h(I_1, I_2, I_3) &= \mu^3 + 3\sigma^2\mu - 3\mu(\sigma^2 + \mu^2 - \mu^2) - \mu^3 \\ &= 0 \end{aligned} \quad (3.19)$$

The statistical test is based on this observation. If $h(I_1, I_2, I_3)$ deviates from 0, then it is concluded that the data is not Gaussian.

Figure 3.7 depicts the prediction error histograms of 30×30 regions with and without microcalcifications. Figure 3.7-(a) is obtained from a region with no microcalcification. The distribution can be modeled as Gaussian. In a region with microcalcifications the distribution is skewed as shown in Figure 3.7-(b). Figure 3.7-(c) is the enlarged view of the tail of the distribution, which extends far to the right mainly due to the presence of microcalcifications. The test statistic, $h(I_1, I_2, I_3)$ reflects this change in the distribution. It is -0.1163 for the region with no microcalcifications and it is 40.4343 for the region containing microcalcifications.

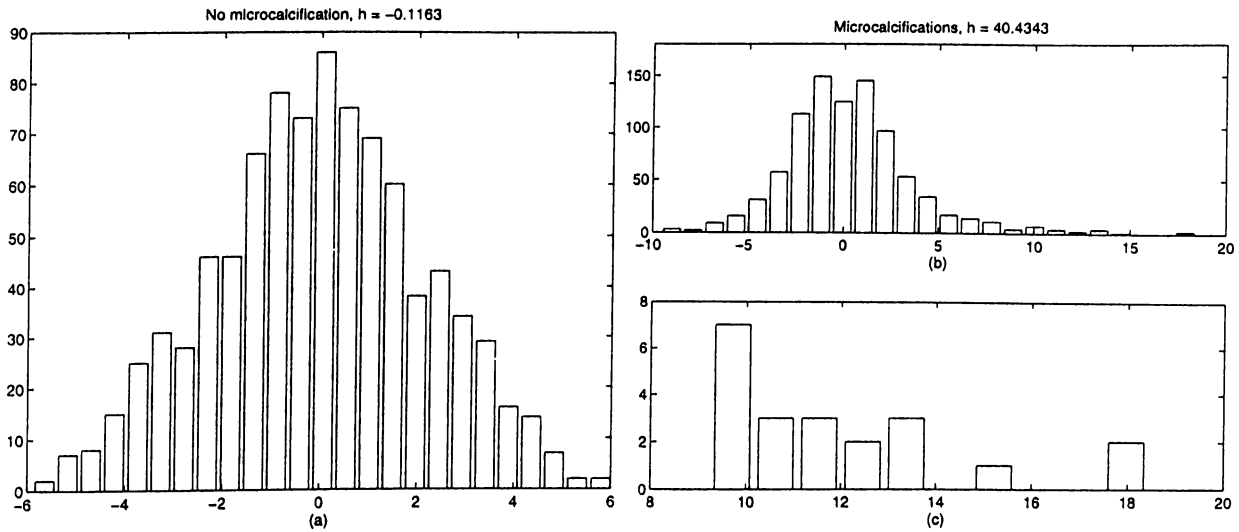


Figure 3.7: Error value distributions in regions (a) without microcalcifications, and (b) with microcalcifications. (c) shows the an enlarged view of the tail of the distribution in (b).

	Mean	Minimum	Maximum
$h(I_1, I_2, I_3)$	65.4993	9.9348	392.9478

Table 3.1: Statistics of h in regions with microcalcifications.

	Mean	Minimum	Maximum
$h(I_1, I_2, I_3)$	0.3819	-2.2578	2.3128

Table 3.2: Statistics of h in regions no microcalcification.

3.1.4 Experimental Results

We tested the above detection method in our training set consisting of 100 different 30×30 regions with and without microcalcifications taken from five different mammogram images. The results of the Gaussianity test are shown in Tables 3.1 and 3.2. These statistics confirm the assumption that in regions with microcalcifications, the test statistic, $h(I_1, I_2, I_3)$ assumes values which are greater than zero while in regions without microcalcifications this statistic is almost equal to zero.

The detection method then can be stated as a hypothesis testing problem in which

the null hypothesis H_0 corresponds to the no microcalcification case and H_1 corresponds to the presence of microcalcifications case:

- H_0 : $|h(I_1, I_2, I_3)| < T_h$
- H_1 : $|h(I_1, I_2, I_3)| \geq T_h$

where T_h is an experimentally determined threshold. Based on the above experimental data, T_h can be chosen as 5 (approximately the midpoint value of [2.31 and 9.93]). The regions with the test statistic value greater than 5 are marked as suspicious regions.

We experimented with the Nijmegen mammogram image database. Using the experimentally determined threshold value, the above detection scheme detected all of the 105 microcalcification clusters with an average 2.3 false detected regions per image (isolated microcalcifications which are not part of a microcalcification cluster are considered to be neutral because they are not early signs of breast cancer). This rate is better than nonadaptive processing.

3.2 A Gaussianity Test Using Fourth Order Parameters

The test statistic, $h(I_1, I_2, I_3)$ depends on second and third order statistics and produces better results than the third order skewness and the fourth order kurtosis in mammogram image analysis. False alarm ratio is reduced from 3.3 false alarms per image to 2.3 false alarms per image. By developing a new test statistic based on the second and fourth order parameters we may further improve the performance of the microcalcification detection scheme. A consequence of this is that the range between the minimum value of the test statistic $h(I_1, I_2, I_3)$ in regions with microcalcifications and the maximum value of the test statistic in regions with no microcalcification can be made larger and if the threshold is set in a wider range, more false positive regions can be eliminated.

In this section, we develop a new Gaussianity test and prove that it is more sensitive to outliers, hence exhibiting a better microcalcification detection performance. The proof is by means of the sensitivity curve, which is a discrete form of the influence function. In Section 3.2.1, the concept of the Influence Function [65] is reviewed. In Section 3.2.2,

the sensitivity curve of the OCM test is derived. Section 3.2.3 describes the design of a new Gaussianity test which use the first, second and the fourth moments.

3.2.1 The Influence Function

The Influence Function (IF) of an estimator T for the cumulative distribution F is given by [65]:

$$IF(u; T, F) = \lim_{t \rightarrow 0} \frac{T((1-t)F + t\delta_u) - T(F)}{t} \quad (3.20)$$

where δ_u is the probability measure which puts mass 1 at point u . The influence function describes the effect of an infinitesimal contamination at the point u on the estimate.

In order to illustrate the use of influence function concept, let us compute the influence function for the sample mean, T_n for a Gaussian distributed sequence. The sample mean function, T_n , for the Gaussian distributed data set, $x_i, i = 1, \dots, n$ is

$$T_n = \frac{1}{n} \sum_{i=1}^n x_i \quad (3.21)$$

The underlying probability density function (pdf) is $f(x) = \frac{1}{\sqrt{2\pi}} e^{-\frac{1}{2}x^2}$ and the cumulative density function (cdf) is $F(u) = \int_{-\infty}^u f(x)dx$. The corresponding functional for the sample mean function in terms of cdf is

$$T(F) = \int u dF(u) \quad (3.22)$$

The influence function for the sample mean function, T_n , for the zero-mean Gaussian distributed sequences can be calculated by substituting Equation 3.22 into the influence function definition given by Equation 3.20:

$$\begin{aligned} IF(u; T, F) &= \lim_{t \rightarrow 0} \frac{\int x d[(1-t)F + t\delta_u](x) - \int x dF(x)}{t} \\ &= \lim_{t \rightarrow 0} \frac{(1-t) \int x dF(x) + t \int x \delta(u-x) dx - \int x dF(x)}{t} \\ &= \lim_{t \rightarrow 0} \frac{tu}{t} \\ &= u \end{aligned} \quad (3.23)$$

noting that the mean of the Gaussian is $\int u dF(u) = 0$

The definition in Equation 3.20 is entirely asymptotic in that functionals with the asymptotic value of the estimator is used. Tukey derived a simple finite-sample version of Equation 3.20 [66]:

$$\mathcal{S}_n(x) = n[T_n(x_1, \dots, x_{n-1}, x) - T_{n-1}(x_1, \dots, x_{n-1})] \quad (3.24)$$

This is called *the sensitivity curve* which basically examines the effect of an additional term, x as an outlier on the overall estimator. Therefore, first the estimator value, $T_{n-1}(x_1, \dots, x_{n-1})$ for $n-1$ terms is calculated. Next, the outlier term, x is added to the sequence and the estimator is again calculated for the n terms, $T_n(x_1, \dots, x_{n-1}, x)$. The difference of these two estimator values exhibits the effect of the outlier on the estimator. The sensitivity curve, $\mathcal{S}_n(x)$ can be plotted against values of the outlier, x to visualize the effect of different values of outliers on the the overall sensitivity of the estimator.

$\mathcal{S}_n(x)$ for the simple mean estimation is:

$$\begin{aligned} \mathcal{S}_n(x) &= n[T_n(x_1, \dots, x_{n-1}, x) - T_{n-1}(x_1, \dots, x_{n-1})] \\ &= n \left[\frac{x_1 + x_2 + \dots + x_{n-1} + x}{n} - \frac{x_1 + x_2 + \dots + x_{n-1}}{n-1} \right] \\ &= x + (x_1 + \dots + x_{n-1}) \left(-\frac{1}{n-1} \right) \end{aligned} \quad (3.25)$$

For large n ,

$$\mathcal{S}_n(x) \rightarrow x \quad (3.26)$$

which is consistent with the result obtained in Equation 3.23 using the definition of the influence function IF.

3.2.2 The Sensitivity Curve of the OCM Test

The OCM Gaussianity test is based on the expression

$$h(I_1, I_2, I_3) = I_3 - 3I_1(I_2 - I_1^2) - I_1^3 \quad (3.27)$$

This test can be simplified and put in the following form after some algebraic manipulations:

$$h(I_1, I_2, I_3) = I_3 - 3I_1I_2 + 2I_1^3 \quad (3.28)$$

The sensitivity curve, $\mathcal{S}_n(x) = n[T_n(x_1, \dots, x_{n-1}, x) - T_{n-1}(x_1, \dots, x_{n-1})]$, of this Gaussianity test can be calculated by first obtaining sensitivity curves for I_3 , I_1I_2 , I_1^3 and then combining these to get the overall sensitivity curve for the statistic $h(I_1, I_2, I_3)$.

The estimator, $T_n(x_1, \dots, x_{n-1}, x)$ for I_3 is

$$T_n(x_1, \dots, x_{n-1}, x) = \frac{x_1^3 + x_2^3 + \dots + x_{n-1}^3 + x^3}{n} \quad (3.29)$$

Therefore, the sensitivity curve, $\mathcal{S}_n^{(i)}(x)$ is

$$\begin{aligned} \mathcal{S}_n^{(i)}(x) &= n \left[\frac{x_1^3 + x_2^3 + \dots + x_{n-1}^3 + x^3}{n} - \frac{x_1^3 + x_2^3 + \dots + x_{n-1}^3}{n-1} \right] \\ &= x^3 + \left(-\frac{1}{n-1} \right) (x_1^3 + \dots + x_{n-1}^3) \end{aligned} \quad (3.30)$$

For large n , $\mathcal{S}_n(x) \rightarrow x^3$.

The estimator, $T_n(x_1, \dots, x_{n-1}, x)$ for I_1I_2 is

$$T_n(x_1, \dots, x_{n-1}, x) = \frac{(x_1 + x_2 + \dots + x_{n-1} + x)(x_1^2 + x_2^2 + \dots + x_{n-1}^2 + x^2)}{n} \quad (3.31)$$

Therefore, the sensitivity curve, $\mathcal{S}_n^{(ii)}(x)$, for I_1I_2 is

$$\begin{aligned} \mathcal{S}_n^{(ii)}(x) &= n \left[\frac{(x_1 + x_2 + \dots + x_{n-1} + x)(x_1^2 + x_2^2 + \dots + x_{n-1}^2 + x^2)}{n} \right. \\ &\quad \left. - \frac{(x_1 + x_2 + \dots + x_{n-1})(x_1^2 + x_2^2 + \dots + x_{n-1}^2)}{n-1} \right] \\ &= \frac{n}{n^2} [x(x_1^2 + \dots + x_{n-1}^2) + xx^2 + (x_1 + \dots + x_{n-1})(x_1^2 + \dots + x_{n-1}^2)] \end{aligned}$$

$$\begin{aligned}
& + x^2(x_1 + \dots + x_{n-1}) - (x_1 + \dots + x_{n-1})(x_1^2 + \dots + x_{n-1}^2)] \\
& \cong \frac{1}{n}[x^3 + x^2(x_1 + \dots + x_{n-1}) + x(x_1^2 + \dots + x_{n-1}^2)] \tag{3.32}
\end{aligned}$$

in the second line it is assumed that $n^2 \cong (n-1)^2$ as we will let $n \rightarrow \infty$.

The estimator, $T_n(x_1, \dots, x_{n-1}, x)$ for I_1^3 is

$$T_n(x_1, \dots, x_{n-1}, x) = \left(\frac{x_1 + x_2 + \dots + x_{n-1} + x}{n} \right)^3 \tag{3.33}$$

Therefore, the sensitivity curve, $\mathcal{S}_n^{(iii)}(x)$ for I_1^3 is

$$\begin{aligned}
\mathcal{S}_n^{(iii)}(x) & = n \left[\left(\frac{x_1 + x_2 + \dots + x_{n-1} + x}{n} \right)^3 - \left(\frac{x_1 + x_2 + \dots + x_{n-1}}{n-1} \right)^3 \right] \\
& = \frac{1}{n^2} [x^3 + 3x^2(x_1 + x_2 + \dots + x_{n-1}) + 3x(x_1 + x_2 + \dots + x_{n-1})^2] \tag{3.34}
\end{aligned}$$

So, the overall sensitivity curve is:

$$\begin{aligned}
\mathcal{S}_n(x) & = \mathcal{S}_n^{(i)}(x) + \mathcal{S}_n^{(ii)}(x) + \mathcal{S}_n^{(iii)}(x) \\
& = x^3 + \left(-\frac{1}{n-1} \right) (x_1^3 + \dots + x_{n-1}^3) \\
& + \frac{1}{n} [x^3 + x^2(x_1 + \dots + x_{n-1}) + x(x_1^2 + \dots + x_{n-1}^2)] \\
& + \frac{1}{n^2} [x^3 + 3x^2(x_1 + x_2 + \dots + x_{n-1}) + 3x(x_1 + x_2 + \dots + x_{n-1})^2] \\
& = x^3 - \frac{3}{n} [x^3 + x^2(x_1 + \dots + x_{n-1}) + x(x_1^2 + \dots + x_{n-1}^2)] \\
& + \frac{2}{n^2} [x^3 + 3x^2(x_1 + x_2 + \dots + x_{n-1}) + 3x(x_1 + x_2 + \dots + x_{n-1})^2] \tag{3.35}
\end{aligned}$$

Simplified expressions for the sensitivity curves can be obtained by defining φ_{n-1} and Ω_{n-1} as follows:

$$\begin{aligned}
\varphi_{n-1} & := x_1 + \dots + x_{n-1}, \\
\Omega_{n-1} & := x_1^2 + \dots + x_{n-1}^2 \tag{3.36}
\end{aligned}$$

Then,

$$\begin{aligned}
\mathcal{S}_n(x) &= x^3 - \frac{3}{n}[x^3 + x^2\varphi_{n-1} + x\Omega_{n-1}] + \frac{2}{n^2}[x^3 + 3x^2\varphi_{n-1} + 3x\varphi_{n-1}^2] \\
&= x^3 \left(1 - \frac{3}{n} + \frac{2}{n^2}\right) + x^2\varphi_{n-1} \left(-\frac{3}{n} + \frac{6}{n^2}\right) + x \left(-\frac{3\Omega_{n-1}}{n} + \frac{6\varphi_{n-1}^2}{n^2}\right) \quad (3.37)
\end{aligned}$$

For large values of n

$$\frac{\varphi_{n-1}}{n} \rightarrow \mu, \quad \frac{\Omega_{n-1}}{n} \rightarrow (\mu^2 + \sigma^2) \quad (3.38)$$

where μ is the mean and σ is the standard deviation. Substituting these values into Equation 3.37, we get

$$\begin{aligned}
\mathcal{S}_n(x) &= x^3 \left(1 - \frac{3}{n} + \frac{2}{n^2}\right) + x^2\mu \left(3 + \frac{6}{n}\right) \\
&\quad + x \left(-3(\mu^2 + \sigma^2) + 6\mu^2\right) \quad (3.39)
\end{aligned}$$

For Gaussian sequences with mean, $\mu = 0$ and standard deviation, $\sigma = 1$, Equation 3.39 simplifies to:

$$\mathcal{S}_n(x) = x^3 \left(1 - \frac{3}{n} + \frac{2}{n^2}\right) - 3x \quad (3.40)$$

For large values of n (i.e. $n \rightarrow \infty$),

$$\mathcal{S}_n(x) = x^3 - 3x \quad (3.41)$$

If (x_1, \dots, x_{n-1}) is a series of 900 random, Gaussian distributed numbers with mean, $\mu = 0$ and standard deviation, $\sigma = 1$ then the sensitivity curve in Figure 3.8 is obtained. This curve closely fits to the curve $y = x^3 - 3x$ as can be expected from Equation 3.39. The sensitivity curve of the mean estimator is also plotted in the same figure.

3.2.3 New Gaussianity Test Using Fourth Order Moment

Traditionally, both third and fourth order statistical parameters are used in Gaussianity detection. For example, Giannakis and Tsatsanis developed a time-domain Gaussianity

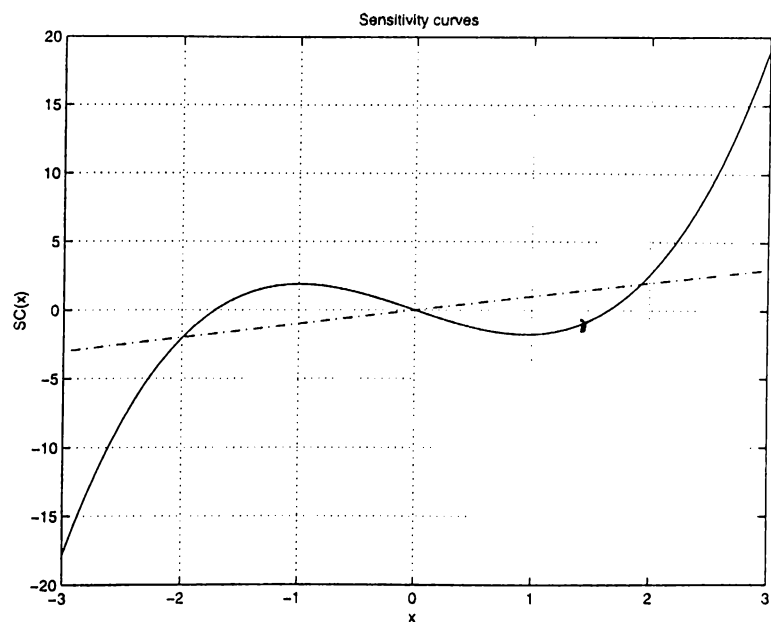


Figure 3.8: Sensitivity curves for mean estimator (dashed lines) and for the OCM Gaussianity test in Equation 3.28 (solid line).

test based on statistics formed from third and fourth order cumulants [16]. In the OCM test, parameters up to the third order are used. By introducing the fourth order, the sensitivity of the statistical test to outliers can be improved. Since microcalcifications will produce outliers in the error image and tests with higher sensitivities can detect the outliers better, the higher the sensitivity of the Gaussianity test, the better its microcalcification detection performance is.

The fourth order moment is derived from the moment generating function of the Gaussian distribution [58], $M_X(t)$:

$$M_X(t) = e^{t\mu + \sigma^2 t^2 / 2} \quad (3.42)$$

The k^{th} order moment of distribution, I_k , is defined in terms of the moment generating function as follows

$$I_k = E(x^k) = \frac{d^k}{dt^k} M_X(t) |_{t=0} \quad (3.43)$$

The first derivative is given by

$$\frac{d}{dt}M_X(t) = (\mu + \sigma^2 t)e^{t\mu + \sigma^2 t^2/2} \quad (3.44)$$

and $I_1 = \mu = \frac{d}{dt}M_X(t)|_{t=0}$. The second derivative is given by

$$\frac{d^2}{dt^2}M_X(t) = [\mu^2 + 2\mu\sigma^2 t + \sigma^2 + \sigma^4 t^2]e^{t\mu + \sigma^2 t^2/2} \quad (3.45)$$

Similar to the mean, $I_2 = \mu^2 + \sigma^2$.

The third derivative is given by

$$\frac{d^3}{dt^3}M_X(t) = [\mu^3 + 3\mu\sigma^2 + t(3\sigma^4 + 3\mu^2\sigma^2) + t^2 3\mu\sigma^4 + t^3 \sigma^6]e^{t\mu + \sigma^2 t^2/2} \quad (3.46)$$

The OCM test is essentially based on Equation 3.46.

Of particular interest here is the fourth moment which is obtained using the following relation:

$$\begin{aligned} \frac{d^4}{dt^4}M_X(t) = & \left[\mu^4 + 3\sigma^4 + 6\mu^2\sigma^2 + t(12\mu\sigma^4 + 4\mu^3\sigma^2) \right. \\ & \left. + t^2(6\sigma^6 + 6\mu^2\sigma^4) + t^3(\mu\sigma^6 + 3\mu\sigma^6) + t^4\sigma^8 \right] e^{t\mu + \sigma^2 t^2/2} \end{aligned} \quad (3.47)$$

In the limit, when the value of t is taken as zero, only the first three terms remain in the above expression and these constitute the fourth moment, I_4 . Hence,

$$I_4 = E(x^4) = \mu^4 + 6\mu^2\sigma^2 + 3\sigma^4 \quad (3.48)$$

In designing the test, we want to establish a function such that it will assume the value of zero for Gaussian distributed sequences. First, a term is needed to eliminate the μ^4 term. In the limit, the moment I_1 approaches to the value of μ , therefore, the fourth power of this moment can be subtracted from the fourth moment term, I_4 . In the limit, $(I_2 - I_1^2)$ approaches to σ^2 , which can then be used to eliminate the second and third terms of the moment expression. Therefore, the statistic for the Gaussianity test turns out to be:

$$H(I_1, I_2, I_4) = I_4 - I_1^4 - 6I_1^2(I_2 - I_1^2) - 3(I_2 - I_1^2)^2 \quad (3.49)$$

which can be then simplified by eliminating the repetitive terms to get:

$$H(I_1, I_2, I_4) = I_4 + 2I_1^4 - 3I_2^2 \quad (3.50)$$

Substituting the limit values of I_4 , I_1 , I_2 into the above expression ensures that this test produces zero for Gaussian distributed sequences:

$$\begin{aligned} H(I_1, I_2, I_4) &= \mu^4 + 6\mu^2\sigma^2 + 3\sigma^4 + 2\mu^4 - 3(\mu^2 + \sigma^2)^2 \\ &= 0 \end{aligned} \quad (3.51)$$

As a natural extension, one may consider designing other Gaussianity tests which include moments higher than the fourth order moment. However, these moments converge very slowly to the normal distributions. So, they should not be used unless very large samples are processed [55].

Let us obtain the sensitivity curve for our Gaussianity test. The estimator, $T_n(x_1, \dots, x_{n-1}, x)$ for I_4 is

$$T_n(x_1, \dots, x_{n-1}, x) = \frac{x_1^4 + x_2^4 + \dots + x_{n-1}^4 + x^4}{n} \quad (3.52)$$

Therefore, the sensitivity curve, $\mathcal{S}_n^{(i)}(x)$ for I_4 is

$$\begin{aligned} \mathcal{S}_n^{(i)}(x) &= n \left[\frac{x_1^4 + x_2^4 + \dots + x_{n-1}^4 + x^4}{n} - \frac{x_1^4 + x_2^4 + \dots + x_{n-1}^4}{n-1} \right] \\ &= x^4 + \left(\frac{1}{n} - \frac{1}{n-1} \right) (x_1^4 + \dots + x_{n-1}^4) \end{aligned} \quad (3.53)$$

For large n , $\left(\frac{1}{n} - \frac{1}{n-1}\right) \rightarrow 0$, hence $\mathcal{S}_n(x) \rightarrow x^4$.

The estimator, $T_n(x_1, \dots, x_{n-1}, x)$ for I_1^4 is

$$T_n(x_1, \dots, x_{n-1}, x) = \left(\frac{x_1 + x_2 + \dots + x_{n-1} + x}{n} \right)^4 \quad (3.54)$$

Therefore, the sensitivity curve, $\mathcal{S}_n^{(i)}(x)$ for I_1^4 is

$$\begin{aligned} \mathcal{S}_n^{(ii)}(x) &= n \left[\left(\frac{x_1 + x_2 + \dots + x_{n-1} + x}{n} \right)^4 - \left(\frac{x_1 + x_2 + \dots + x_{n-1}}{n-1} \right)^4 \right] \\ &= \frac{1}{n^3} [x^4 + 4x^3(x_1 + x_2 + \dots + x_{n-1}) + 4x^2(x_1 + x_2 + \dots + x_{n-1})^2 \\ &\quad + 2x(x_1 + x_2 + \dots + x_{n-1})^3] \end{aligned} \quad (3.55)$$

The estimator, $T_n(x_1, \dots, x_{n-1}, x)$ for I_2^2 is

$$T_n(x_1, \dots, x_{n-1}, x) = \left(\frac{x_1^2 + x_2^2 + \dots + x_{n-1}^2 + x^2}{n} \right)^2 \quad (3.56)$$

Therefore, the sensitivity curve, $\mathcal{S}_n^{(i)}(x)$ for I_2^2 is

$$\begin{aligned} \mathcal{S}_n^{(iii)}(x) &= n \left[\left(\frac{x_1^2 + x_2^2 + \dots + x_{n-1}^2 + x^2}{n} \right)^2 - \left(\frac{x_1^2 + x_2^2 + \dots + x_{n-1}^2}{n-1} \right)^2 \right] \\ &= \frac{1}{n} [x^4 + 2x^2(x_1^2 + x_2^2 + \dots + x_{n-1}^2)] \end{aligned} \quad (3.57)$$

As a result, the overall sensitivity curve is:

$$\begin{aligned} \mathcal{S}_n(x) &= \mathcal{S}_n^{(i)}(x) + \mathcal{S}_n^{(ii)}(x) + \mathcal{S}_n^{(iii)}(x) \\ &= x^4 + \left(\frac{1}{n} - \frac{1}{n-1} \right) (x_1^4 + \dots + x_{n-1}^4) \\ &\quad + \frac{1}{n^3} [x^4 + 4x^3(x_1 + x_2 + \dots + x_{n-1}) + 4x^2(x_1 + x_2 + \dots + x_{n-1})^2 \\ &\quad + 2x(x_1 + x_2 + \dots + x_{n-1})^3] \\ &\quad + \frac{1}{n} [x^4 + 2x^2(x_1^2 + x_2^2 + \dots + x_{n-1}^2)] \\ &= x^4 + \frac{2}{n^3} [x^4 + 4x^3\varphi_{n-1} + 4x^2\varphi_{n-1}^2 + 2x\varphi_{n-1}^3] - \frac{3}{n} [x^4 + 2x^3\Omega_{n-1}] \end{aligned}$$

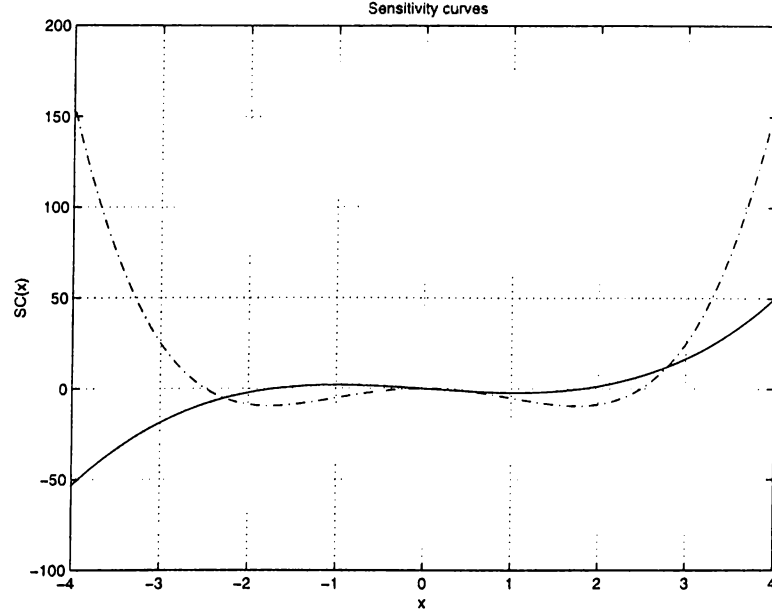


Figure 3.9: Sensitivity curves for the Gaussianity test in Equation 3.28 (solid line) and for the Gaussianity test in Equation 3.50 (dashed line).

$$\begin{aligned}
&= x^4 \left(1 - \frac{3}{n} + \frac{2}{n^3} \right) + x^3 \varphi_{n-1} \left(\frac{8}{n^3} \right) \\
&+ x^2 \left(\frac{8}{n^3} \varphi_{n-1}^2 - \frac{6}{n} \Omega_{n-1} \right) + x \left(-\frac{4\varphi_{n-1}^3}{n^3} \right) \quad (3.58)
\end{aligned}$$

where φ_{n-1} and Ω_{n-1} are as defined in Equation 3.36.

For large values of n , $\frac{\varphi_{n-1}}{n} \rightarrow \mu$, $\frac{\Omega_{n-1}}{n} \rightarrow (\sigma^2 + \mu^2)$. Equation 3.58 becomes:

$$\begin{aligned}
\mathcal{S}_n(x) &= x^4 + x^3 \left(\frac{8}{n^3} n \mu \right) \\
&+ x^2 \left(\frac{8}{n^3} n^2 \mu^2 - \frac{6}{n} n (\sigma^2 + \mu^2) \right) + x \left(-\frac{4}{n^3} n^3 \mu^3 \right) \quad (3.59)
\end{aligned}$$

which boils down to the following relation for Gaussian signals with mean, $\mu = 0$ and standard deviation, $\sigma = 1$:

$$\mathcal{S}_n(x) = x^4 - 6x^2 \quad (3.60)$$

When the new Gaussianity test is used with the adaptive filtering scheme, the statistics in Tables 3.3 and 3.4 are obtained. These test statistics are obtained from 100 different 30×30 regions on 5 different mammogram images.

	Mean	Minimum	Maximum
$H(I_1, I_2, I_4)$	406.8	52.4	3712.3

Table 3.3: Test statistics in regions with microcalcifications.

	Mean	Minimum	Maximum
$H(I_1, I_2, I_4)$	1.25	-4.4	11.1

Table 3.4: Test statistics in regions with no microcalcification.

In Figure 3.9, the sensitivity curves of the OCM Gaussianity test and our Gaussianity test are plotted. As can be observed from this figure, the sensitivity of our Gaussianity test is higher than that of the OCM test especially at large values. Therefore, the new Gaussianity test emphasizes outliers more. Since the microcalcifications appear as outliers, their detection gets easier with the new test. Actually, the statistics of the newly developed test in Equation 3.50 reflect this change: while the mean values in regions with no microcalcifications remain close to zero, the Gaussianity test produces high mean values in regions with microcalcifications.

As skewness and kurtosis are third and fourth order statistical tests, respectively, it might be relevant to compare their sensitivities with the sensitivities of the OCM test and our Gaussianity test. Figure 3.10 compares the sensitivity curve of the skewness with the sensitivity OCM test. A similar comparison is made in Figure 3.11 for kurtosis and our Gaussianity test. These figures indicate that the OCM test and our Gaussianity test show more sensitivity to outliers especially those with high values.

We also examined the effect of the OCM test and the new Gaussianity test when the fixed bandpass filter described in Chapter 2 is used instead of the adaptive filter. Tables 3.5 and 3.6 show the statistics of the OCM test and our Gaussianity test in regions with and without microcalcifications in the training set, respectively. If these tables are compared with the Table 2.4, it can be observed that the OCM test and our Gaussianity test provide better discrimination than skewness and kurtosis based tests for the bandpass filtered images. When combined with adaptive filtering the new tests further improve the discriminating range.

The new Gaussianity test can be combined with the OCM Gaussianity test in order

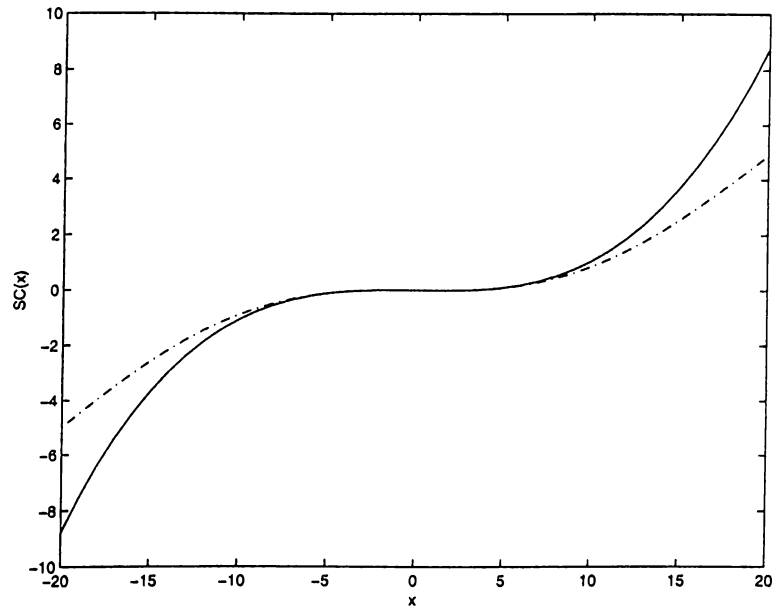


Figure 3.10: Sensitivity curves for skewness (dashed line) and the OCM Gaussianity test (solid line).

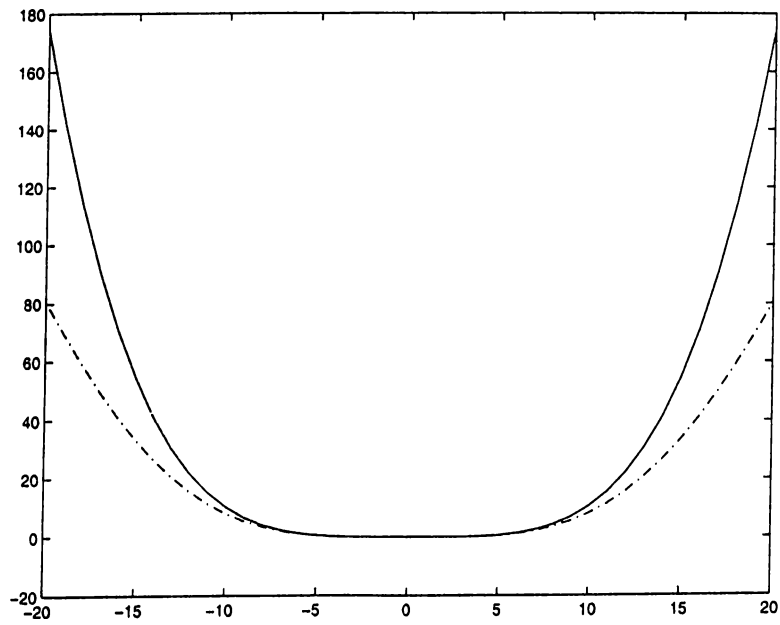


Figure 3.11: Sensitivity curves for kurtosis (dashed line) and our Gaussianity test (solid line).

	Mean	Minimum	Maximum
$h(I_1, I_2, I_3)$	2.8662	1.2780	5.3926
$H(I_1, I_2, I_4)$	13.0044	4.0553	26.1569

Table 3.5: Test statistics obtained from bandpass filtered images in regions with microcalcifications: the OCM test $h(I_1, I_2, I_3)$ and our Gaussianity test $H(I_1, I_2, I_4)$.

	Mean	Minimum	Maximum
$h(I_1, I_2, I_3)$	0.0320	-0.2470	0.4433
$H(I_1, I_2, I_4)$	0.1495	-0.1720	2.0034

Table 3.6: Test statistics obtained from bandpass filtered images in regions with no microcalcification: the OCM test $h(I_1, I_2, I_3)$ and our Gaussianity test $H(I_1, I_2, I_4)$.

to get a better performance. Because in the combined test, both the third order and the fourth order parameters are used. As the range between the maximum value of the test statistic in region with no microcalcifications and the minimum value of the test statistic in regions with microcalcifications gets larger, it is easier to set the threshold at a higher level. The higher threshold provides the flexibility to eliminate some additional false alarm (or single-bright spot) regions.

In our experiments with the mammogram database containing 40 images, the false alarm rate decreased from 2.3 per image to 1.125 per image. This justifies the effectiveness of the new Gaussianity test for the microcalcification detection. The obtained false alarm rate is much lower than that of Strickland and Hahn who use a wavelet based scheme and utilize the same database [4]. They get 8 false alarms per image when all the clusters in the database are detected.

Chapter 4

MICROCALCIFICATION SEGMENTATION and MAMMOGRAM ENHANCEMENT

Chapters 2 and 3 describe microcalcification detection schemes. In these schemes, parts of mammogram image with microcalcifications are marked as suspicious regions as shown in Figure 2.13. Within these marked regions (or regions marked by other detection schemes), individual microcalcifications can be segmented through further processing. The shape and exact extent of segmented microcalcifications can provide valuable information to radiologists in their diagnosis, and classification of the abnormalities as benign or malignant. They can also be used in three dimensional reconstruction of microcalcifications within the breast structure.

Individual microcalcifications can be segmented in a two-stage process. The first stage is removal of the breast structure corresponding to the healthy tissues. The second stage is a statistical outlier detection. Bandpass filtering, nonlinear 'subband' decomposition, adaptive filtering, and adaptive filtering based subband decomposition can be used to remove underlying the breast structure from mammogram images. Bandpass filtering, nonlinear subband decomposition, and adaptive filtering concepts

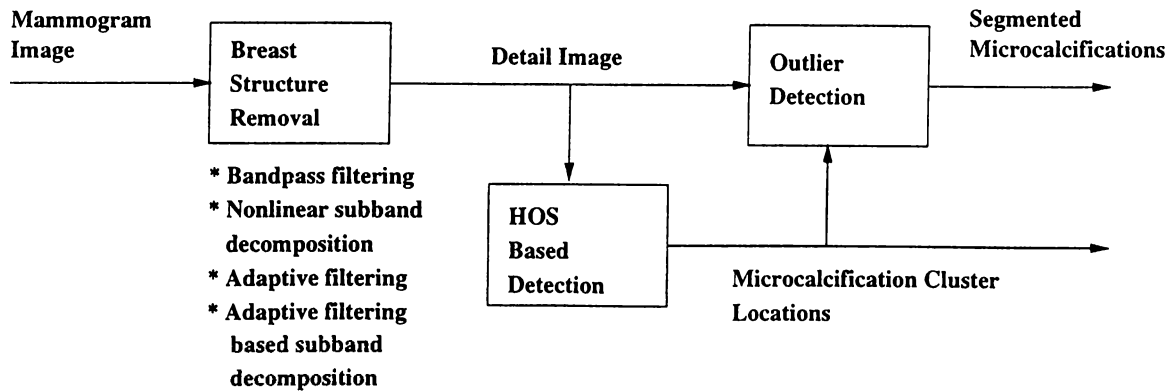


Figure 4.1: Microcalcification segmentation structure.

are reviewed in Chapters 2 and 3 while discussing HOS based detection schemes. A recently developed adaptive filtering based subband decomposition structure is reviewed in Section 4.1.1.

After the underlying breast structure is removed, the remaining detail image mainly contains microcalcifications as well as some additional noise. As we discuss in Chapters 2 and 3, microcalcifications will produce outliers in this detail image. Therefore, an outlier detection method can single out these abnormalities. In Section 4.1.2 boxplot labeling, which is a statistical outlier detection method, is reviewed.

After the segmentation of individual microcalcifications, they can be combined with the original mammogram image to get visually enhanced mammogram images. In Section 4.2 we propose superposition, magnification and nonlinear subband decomposition based mammogram image enhancement methods.

Ffrench *et al.* observe that adaptive filtering enhances the mammogram images by predicting the breast tissue and leaving the small microcalcifications in the error image [50]. However, they do not specify an enhancement or detection scheme. They just suggest that further research needs to be done.

In the segmentation and enhancement processes, nonlinear operations with relatively high computational costs can be used while keeping the overall computational complexity of the system low. Because, rather than processing the entire image for segmentation and enhancement, only suspicious regions are considered.

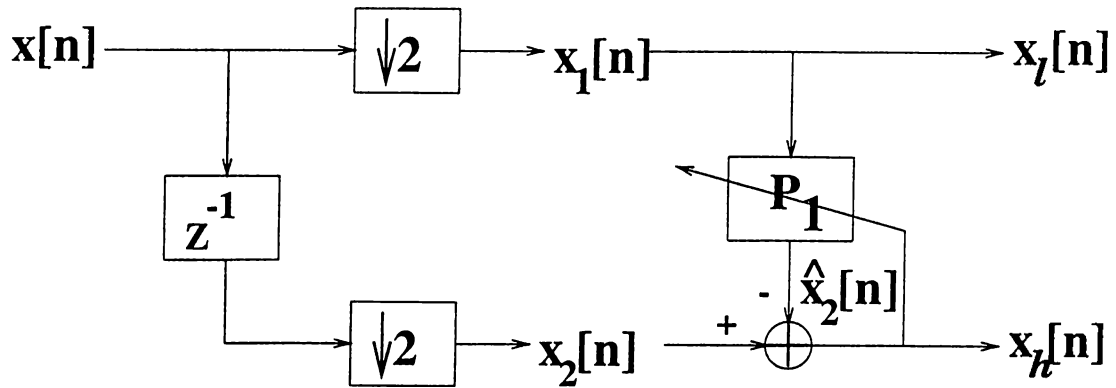


Figure 4.2: Adaptive Structure Analysis Stage in [52].

4.1 Segmentation of Microcalcifications

Once the regions containing microcalcifications are detected, individual microcalcifications can be segmented within detected regions, using further processing [28, 29]. We propose a two-stage microcalcification segmentation scheme as shown in Figure 4.1. The first stage is breast structure removal. We have seen that bandpass filters, nonlinear subband decomposition structures and adaptive filters are effective in removing the breast structure. In Section 4.1.1, we also consider the use of adaptive filtering based subband decomposition structures for the same purpose.

A detail image is produced after the breast structure is removed. This detail image is utilized by the HOS based detection schemes as described in Chapters 2 and 3. Within the detected regions, the statistical outlier detection scheme segments individual microcalcifications using the detail image. In Section 4.2.2, an outlier detection scheme is introduced to segment individual microcalcifications.

4.1.1 Adaptive Filtering based Subband Decomposition

The lifting scheme of Sweldens [37] can be implemented with adaptive filters in the lifting stage [52]. The resulting structure still has the perfect reconstruction property and was utilized in image compression applications [52]. Figures 4.2 and 4.3 illustrate the analysis and the synthesis stages of the subband decomposition structure. Both the analysis side and the synthesis side have the same adaptive filter structures.

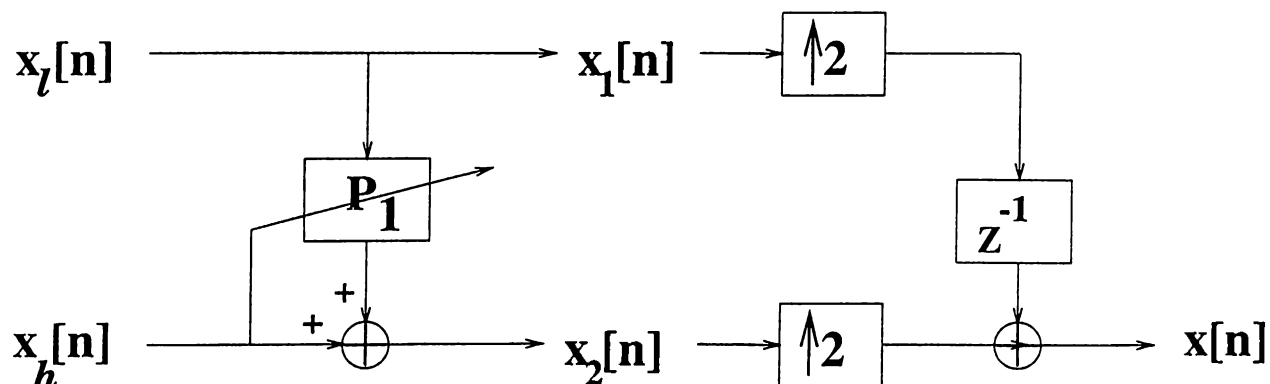


Figure 4.3: Adaptive Structure Synthesis Stage in [52].

In Figure 4.2, the odd indexed pixels constitute the signal x_1 while even indexed pixels constitute the signal x_2 . The finite impulse response estimator predicts the signal x_2 from the signal x_1 in the Linear Minimum Mean Square Sense (LMMS):

$$\hat{x}_2[n] = \sum_{k=0}^N w_{n,k} x_1[n-k] = \sum_{k=0}^N w_{n,k} x[2n-2k] \quad (4.1)$$

where $w_{n,k}$ are the filter coefficients.

The detail signal, x_h contains, mainly the highly varying components including the microcalcifications and is given by:

$$x_h[n] = x_2[n] - \hat{x}_2[n] \quad (4.2)$$

The filter coefficients are updated using an LMS-type adaptive algorithm:

$$w_{n+1,k} = w_{n,k} + \mu x_h[n] x_1[n] \quad (4.3)$$

where μ is the adaptation constant. Experimentally, the value of the step size μ is set to be 10^{-6} . In the prediction, the number of filter coefficients is set to 10 which is the maximum microcalcification width on our mammogram database. The initial filter coefficients have the same weight.

The synthesis stage can perfectly reconstruct the signal original signal, x_n given only the signals x_l and x_h without any side information. It should be noted that the adaptation parameters for updating the prediction filters in the analysis stage must be readily available in the synthesis stage, as well.

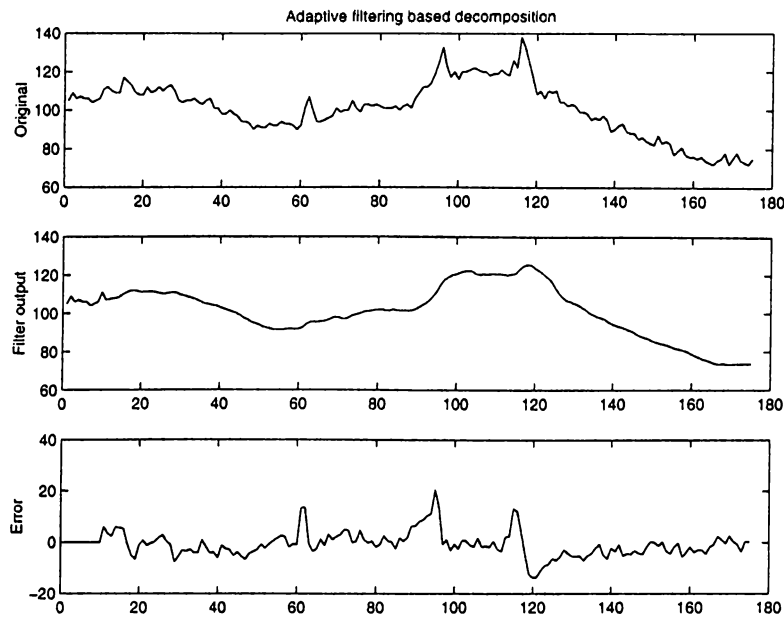


Figure 4.4: Adaptive filtering based subband decomposition for microcalcification segmentation.

Figure 4.4 shows the results of applying an adaptive filtering based subband decomposition structure for the breast structure removal. In this figure, $x[n]$ is a line of a part of a mammogram image containing 3 microcalcifications. In the detail image these microcalcifications are more apparent.

Figure 4.5 shows the effect of using different breast structure removal methods. Figure 4.5 (a) shows the a line of mammogram image. All the other images are the detail images which are obtained by bandpass filtering in Figure 4.5 (b), adaptive filtering in Figure 4.5 (c), nonlinear subband decomposition in Figure 4.5 (d) and adaptive filtering based subband decomposition in Figure 4.5 (e). It can be observed from these figures that the detail images are similar and they produce high values at the locations of microcalcifications. The number of samples in the detail image Figure 4.5 (e) is half of those of the other detail images because of downsampling operation in the decomposition structure.

The resultant detail image is the input for the statistical outlier detection method of the microcalcification segmentation scheme which will be discussed in the next section.

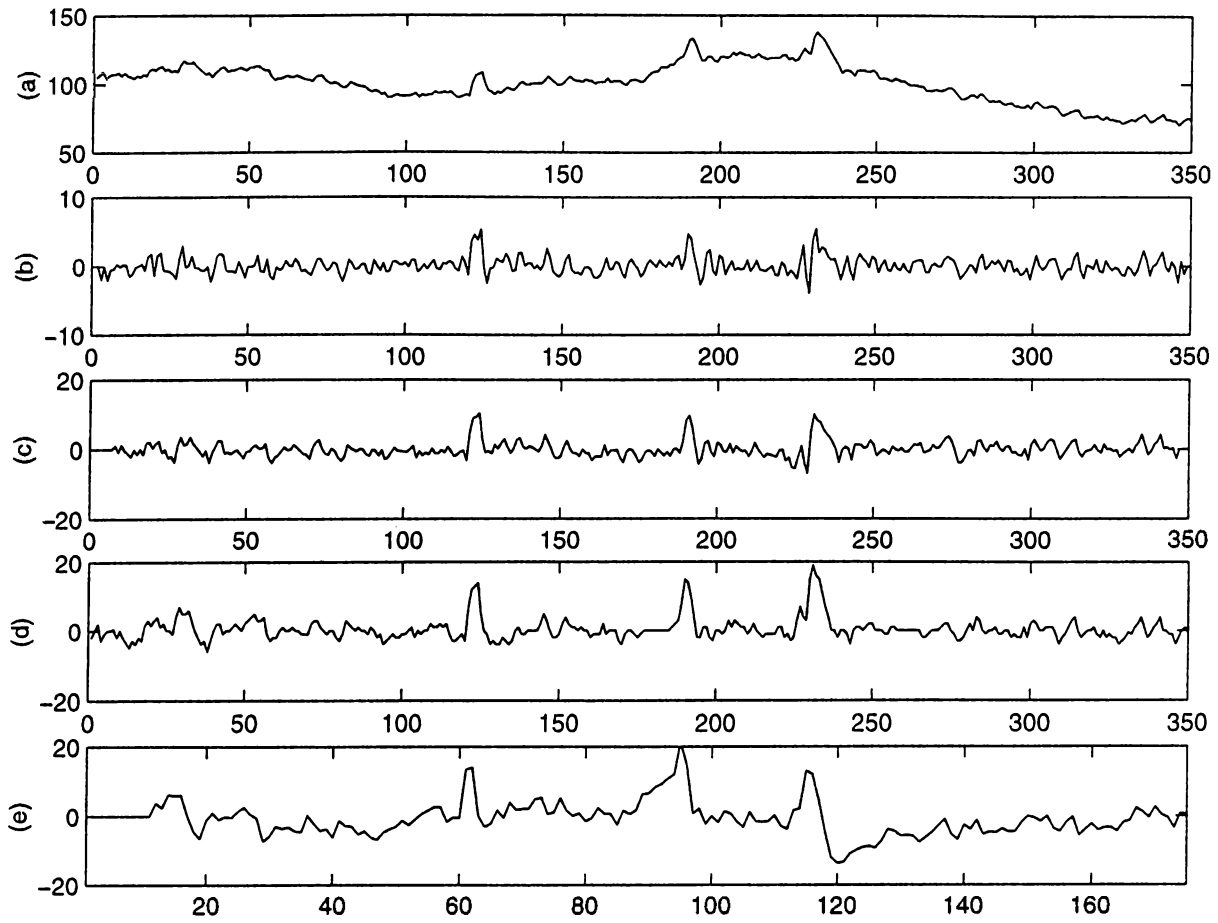


Figure 4.5: Comparison of detail images produced by different breast structure removal operations. (a) Original line of mammogram image, (b) bandpass filtering, (c) adaptive filtering, (d) nonlinear subband decomposition (e) adaptive filtering based subband decomposition

4.1.2 Boxplot Outlier Labeling Method

An outlier is “an observation (or subset of observations) which appears to be inconsistent with the remainder of that set of data.” [44]. Therefore, the microcalcification segmentation problem is equivalent to outlier detection in the detail subimage. Generally, due to the random nature of data, identifying and handling individual outliers is not an easy task. Nevertheless, there are numerous techniques available to detect and handle outlier locations [38].

In this work, we used the boxplot outlier labeling method [38] which is available in most of the statistical software packages. In this method data, \mathbf{x} , is first rank ordered, $\mathbf{x} = \{x_{[1]}, x_{[2]}, \dots, x_{[n]}\}$. Next, the lower quartile, Q_1 and the upper quartile Q_3 values are determined through the following formulae in Equations 4.4-4.6.

$$f = \frac{\lfloor (n+1)/2 \rfloor + 1}{2} \quad (4.4)$$

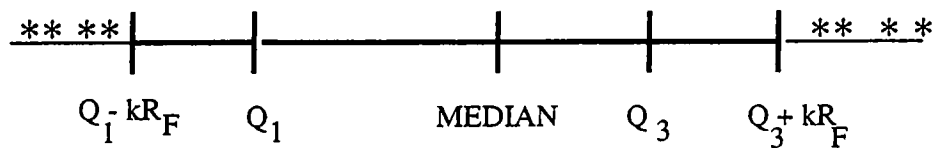
$$Q_1 = x_{[f]} \quad (4.5)$$

$$Q_3 = x_{[n+1-f]} \quad (4.6)$$

where $\lfloor (n+1)/2 \rfloor$ represents the greatest integer less than or equal to $(n+1)/2$. The *interquartile range* R_F is defined to be $Q_3 - Q_1$.

The boxplot method determines the outliers to be the part of data which is outside the range $(Q_1 - kR_F, Q_3 + kR_F)$. The parameter k is determined for the data set under consideration in a statistical manner and is usually taken to be 1.5 or 3.0 [38]. Figure 4.6 illustrates the definition of the boxplot outlier labeling method.

Figure 4.7 (a) shows a horizontal line of mammogram image which is known to contain a microcalcification. Figure 4.7 (b) depicts the difference between the original



* : OUTLIERS

Figure 4.6: Illustration of the outlier detection by the boxplot outlier labeling method described in Section 4.1.2.

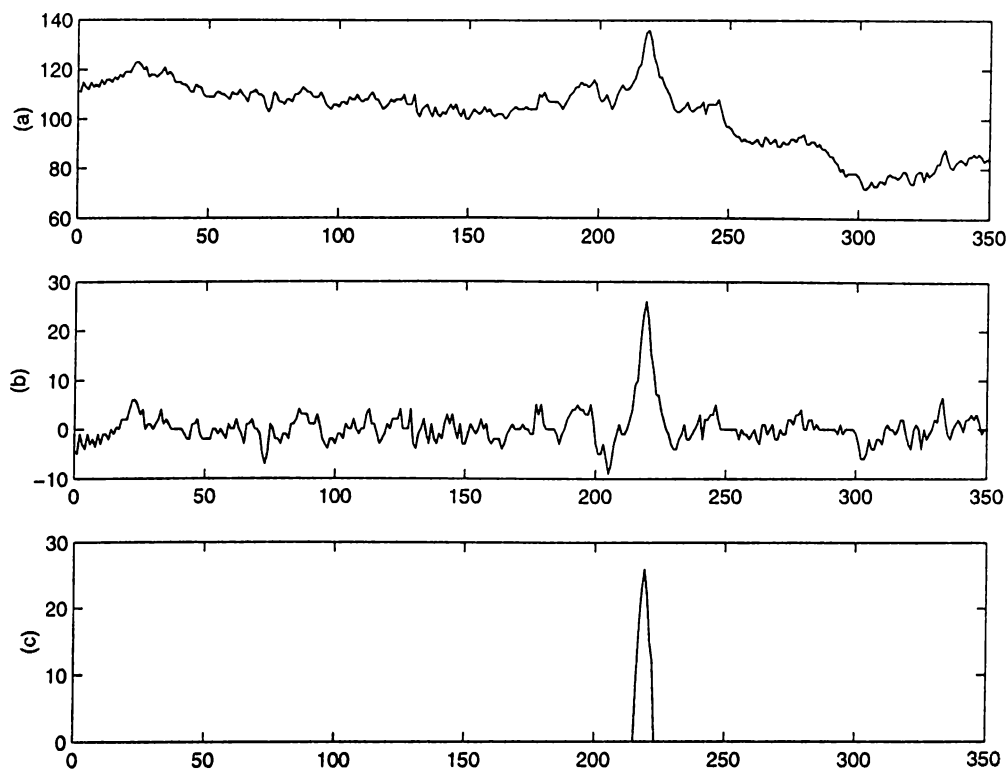


Figure 4.7: Microcalcification segmentation using outlier detection: (a) A horizontal line of the mammogram image which is known to contain a microcalcification, (b) high-band sub-signal x_h , (c) output of the outlier detection method.

signal and its median filtered version. This difference plot corresponds to the high-subband of the nonlinear decomposition structure. The boxplot outlier labeling method is applied to the high subband signal. Figure 4.7 (c) illustrates the output of the outlier detection scheme. Similar results are obtained in two dimensions. For instance, Figure 4.8 (a) shows a part of a mammogram image with a cluster of microcalcifications. In Figure 4.8 (b), the output of the microcalcification segmentation scheme is shown. This segmentation scheme employs a median filter based nonlinear subband decomposition as well as boxplot outlier labeling.

The output of the boxplot outlier detection method produce the segmented microcalcifications. These microcalcifications can either be used in the three-dimensional reconstruction [18, 19] or in mammogram image enhancement which is discussed in the next section.

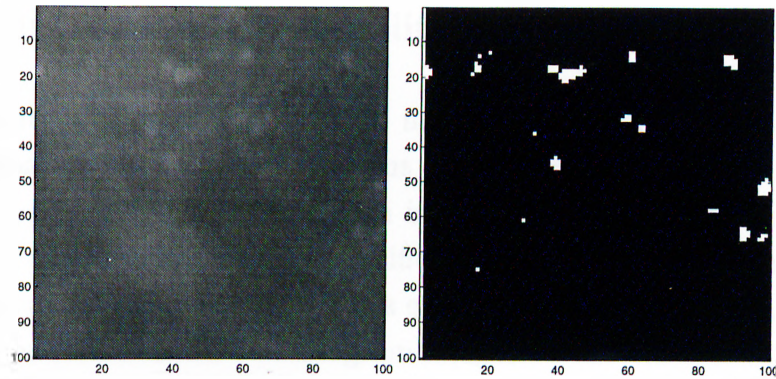


Figure 4.8: (a) A region of a mammogram image containing microcalcifications, (b) output of the segmentation.

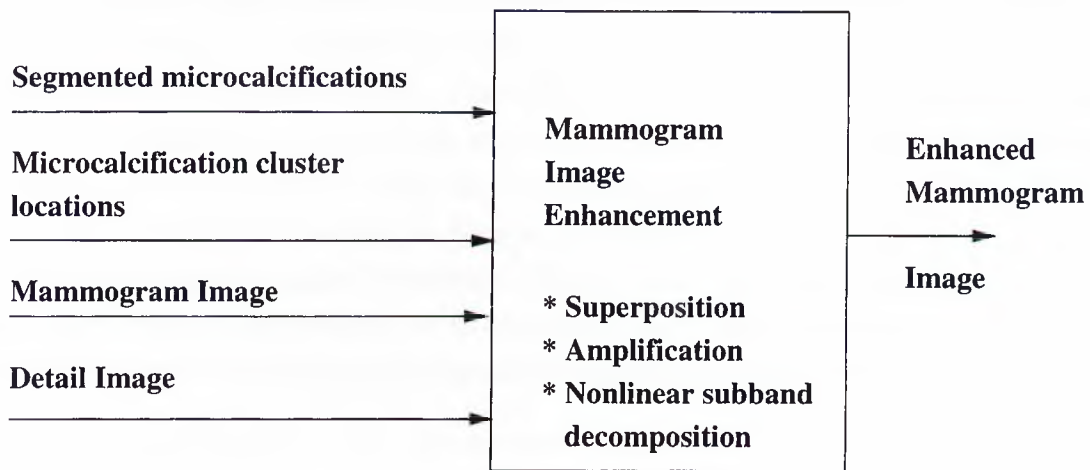


Figure 4.9: Mammogram image enhancement.

4.2 Mammogram Image Enhancement

It is desired that segmented microcalcifications be readily noticeable in an enhanced version of the original mammogram image. Therefore, the output of the microcalcification segmentation can be combined with the original mammogram image to get an enhanced version of the mammogram. We propose three different approaches: *superposition*, *amplification* and nonlinear subband decomposition based enhancement. Figure 4.9 illustrates the enhancement operation. In Section 4.2.1 superposition and amplification based enhancement schemes are discussed. Section 4.2.2 explains the use of nonlinear subband decomposition structures in mammogram image enhancement.

4.2.1 Superposition and Amplification Based Enhancement

In the superposition approach, segmented microcalcifications are superimposed to the original mammogram image at the locations of microcalcifications. In the amplification based approach, the original mammogram image pixel values are weighted by a fixed weight, again at the locations of microcalcifications. We will first observe the effects of these operations on one dimensional signals extracted from mammogram images. Then, the results will be examined in mammogram images.

Figure 4.10 illustrates the steps of superposition based mammogram image enhancement on a horizontal line of a mammogram image. In particular, Figure 4.10 (a) depicts the original line of a mammogram image which is known to contain three microcalcifications. The difference between the original signal and its median filtered version is shown in Figure 4.10 (b). This difference plot corresponds to the detail-signal, $y_d[n]$, of the nonlinear decomposition structure. Figure 4.10 (c) illustrates the output of the outlier detection scheme. Three microcalcifications are successfully segmented. The microcalcifications are enhanced in Figure 4.10 (d). Similarly, the mammogram image enhancement by amplification is shown in Figure 4.11. The amplification weight is 20%. Figure 4.12 gives a comparison of the enhancement result obtained by two different methods. Both methods enhance the signal at locations of microcalcifications successfully.

Previous segmentation and enhancement operations are all performed over one dimensional signals that are extracted from mammogram images with microcalcification clusters. Actually, the results can be generalized to two dimensions. For instance, Figure 4.13 illustrates the enhanced images for the mammogram image in Figure 4.8 (a) using two approaches: superposition and magnification.

In case enhancement of the tissue around the microcalcification regions is also desired, the final image can be displayed after scaling so that the full dynamic range of the display device is employed. This operation is called *contrast stretching* [53]. For the image, $x[m, n]$ the contrast stretching operation produces the output, $x_{CS}[m, n]$:

$$x_{CS}[m, n] = \frac{(x[m, n] - x_{min})}{x_{max} - x_{min}} \times 255 \quad (4.7)$$

where x_{max} and x_{min} are the maximum and minimum pixel intensities of the image, $x[m, n]$, respectively. 255 represents the maximum intensity value for the 8 bit images (so, $2^B - 1$, should be used instead for B bit images). Figure 4.14 shows the results of

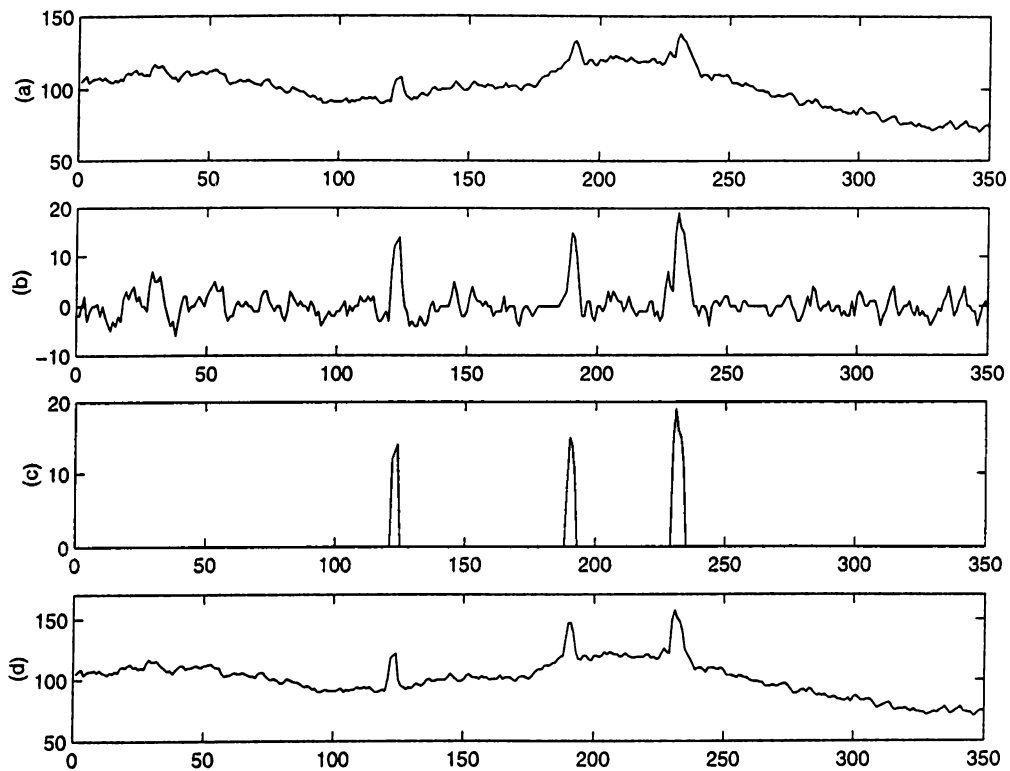


Figure 4.10: Superposition based mammogram image enhancement: (a) A horizontal line of the mammogram image, (b) the detail signal, $y_d[n]$ obtained by nonlinear subband decomposition, (c) output of the outlier detection method, (d) microcalcifications are enhanced by superposition.

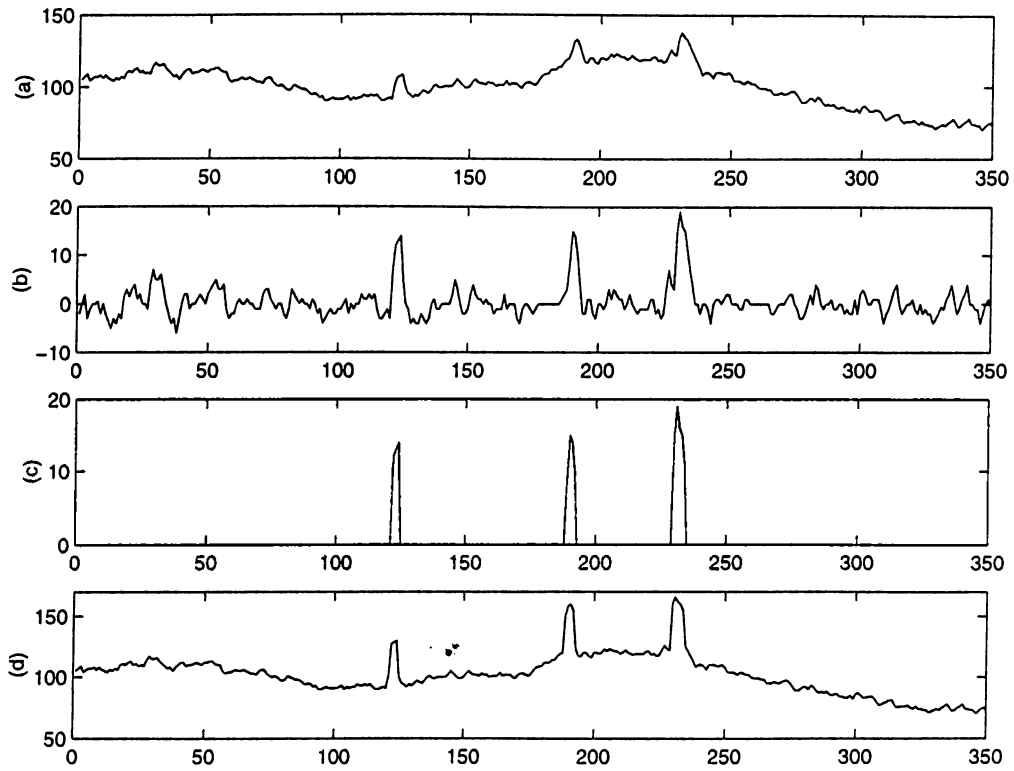


Figure 4.11: Amplification based mammogram image enhancement: (a) A horizontal line of the mammogram image, (b) the detail signal, $y_d[n]$ obtained by nonlinear subband decomposition, (c) output of the outlier detection method, (d) microcalcifications are enhanced by amplification.

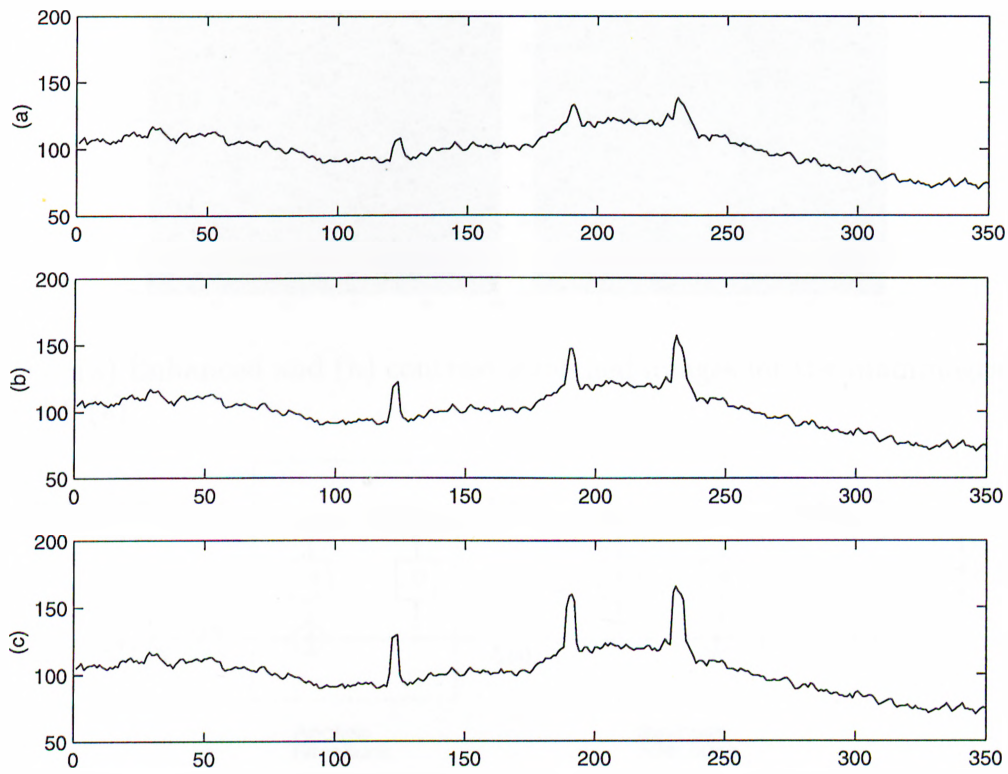


Figure 4.12: Comparison of mammogram image enhancement schemes: (a) A horizontal line of the mammogram image, (b) mammogram image enhancement by superposition, (c) mammogram image enhancement by amplification.

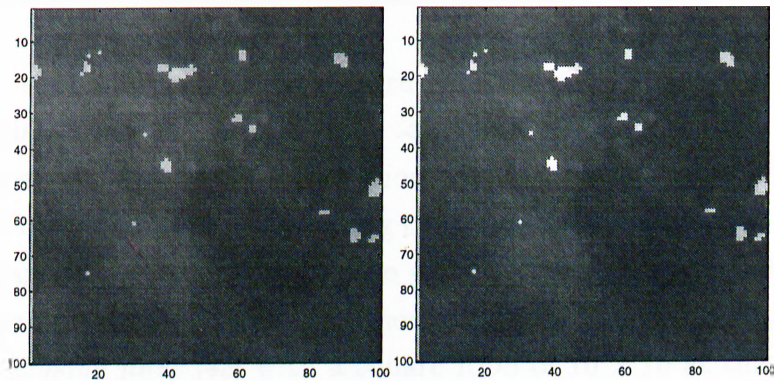


Figure 4.13: Enhanced Images (a) Microcalcifications are superimposed on the mammogram image, (b) Mammogram image is magnified at the locations of microcalcifications.

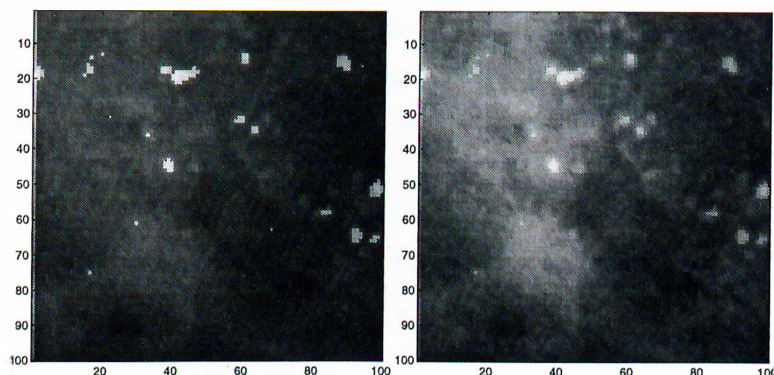


Figure 4.14: (a) Enhanced and (b) contrast stretched images for the mammogram image in Figure 4.8 (a).

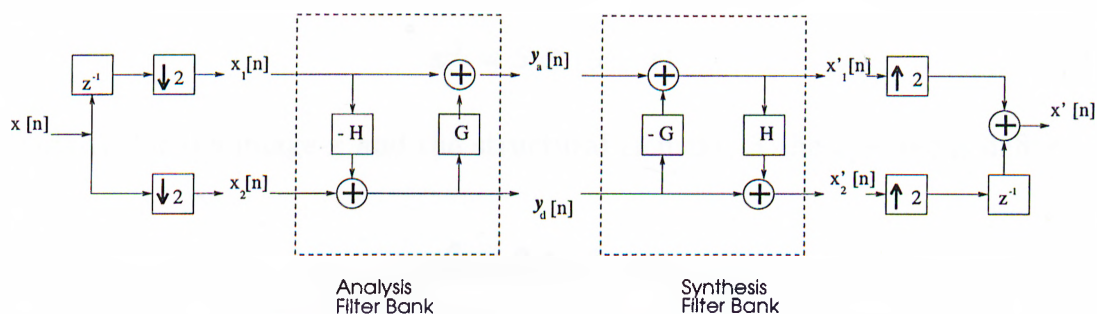


Figure 4.15: Nonlinear Subband Decomposition Structure.

such a contrast stretching algorithm applied to an enhanced mammogram image.

4.2.2 Nonlinear Subband Decomposition Based Enhancement

In the nonlinear subband decomposition structure shown in Figure 4.15, the H filter is chosen as a median filter with a ROS of 21×21 , as we discuss in Section 2.5. Only the detail image, $y_d[m, n]$ is utilized for detection purposes. Equation 2.10 shows that the image $y_a[m, n]$ is obtained by superimposing the original with a nonlinear filtered version of the detail-image $G(y_d[m, n])$. The image $y_a[m, n]$ can be considered as an enhanced image for an appropriate selection of the nonlinear function G . In this application, G is chosen as the *closing filter* [43] with a square ROS of 10×10 at the $100\mu m$ scanning rate. The ROS of the closing filter is chosen in such a way that mainly microcalcifications remain after this nonlinear filtering operation.

Closing filter is a morphological, nonlinear filtering operation. It is defined in

terms of other nonlinear operations erosion, \ominus and dilation, \oplus . Let $x[m, n]$ be the image to be filtered and $S[m, n]$ be the region of support of the filter (also called the structural element). Erosion and dilation of $x[m, n]$ in $S[m, n]$ are defined as below, respectively [47] :

$$S[m, n] \ominus x[m, n] = \min_{(k, l) \in S} x[m - k, n - l] \quad \text{for every } (k, l) \in S \quad (4.8)$$

$$S[m, n] \oplus x[m, n] = \max_{(k, l) \in S} x[m - k, n - l] \quad \text{for every } (k, l) \in S \quad (4.9)$$

After these definitions, for the image x and the structural element, S the closing, x_C^S is defined as

$$x_C^S = S \ominus (S \oplus x) \quad (4.10)$$

Similarly, for the image x and the structural element, S the *opening* is defined as

$$x_O^S = S \oplus (S \ominus x) \quad (4.11)$$

The effects of median and closing type nonlinear operations can be observed in Figures 4.16 and 4.17. Figure 4.16 illustrates a line of mammogram image containing a rather visible microcalcification. After the median filtering, this microcalcification is eliminated. The output of the median filter represents the mammogram background structure corresponding to the ordinary breast tissue. Most of the noise as well as microcalcifications are not present in the output. In the difference image, which is obtained by subtracting the median filtered image from the original mammogram image, mainly the microcalcification is observed.

Figure 4.17 illustrates the effects of the closing operation on the difference image. The input to the dilation filter is the difference image. The dilation filter in Equation 4.9 eliminates the noise but the microcalcification is made larger than its normal size. Next, the erosion filter in Equation 4.8 with a rectangular structure element of length 10, approximately resumes the actual size of the microcalcification. Therefore, the closing filter is effective in singling out microcalcifications on the mammogram. Almost all of the small ripples due to noise are eliminated while the microcalcification is retained similar to the previous cases.

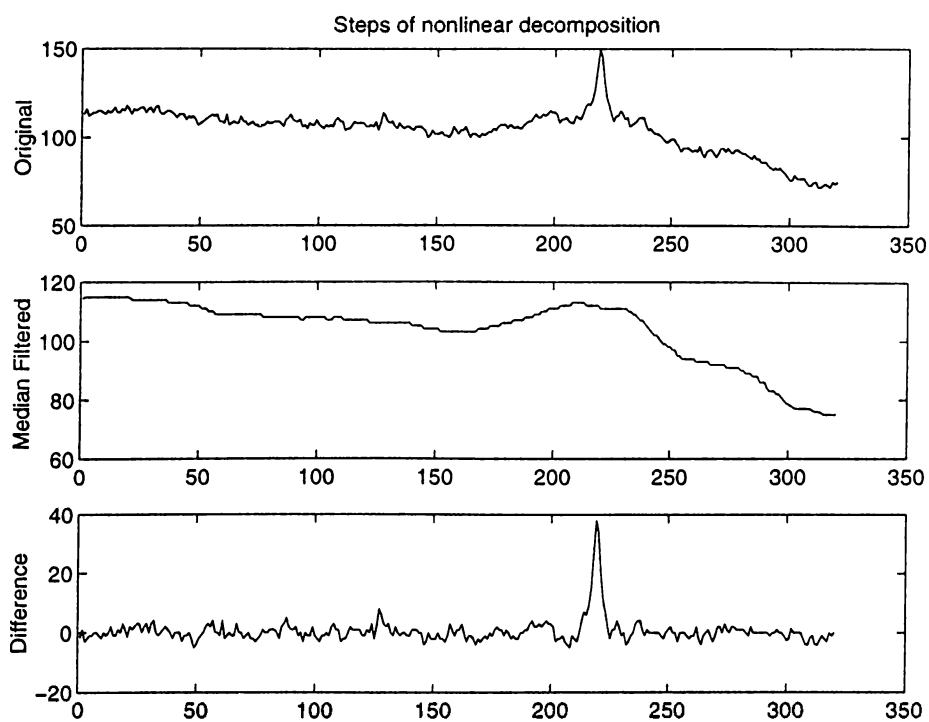


Figure 4.16: Median filter based nonlinear subband decomposition.

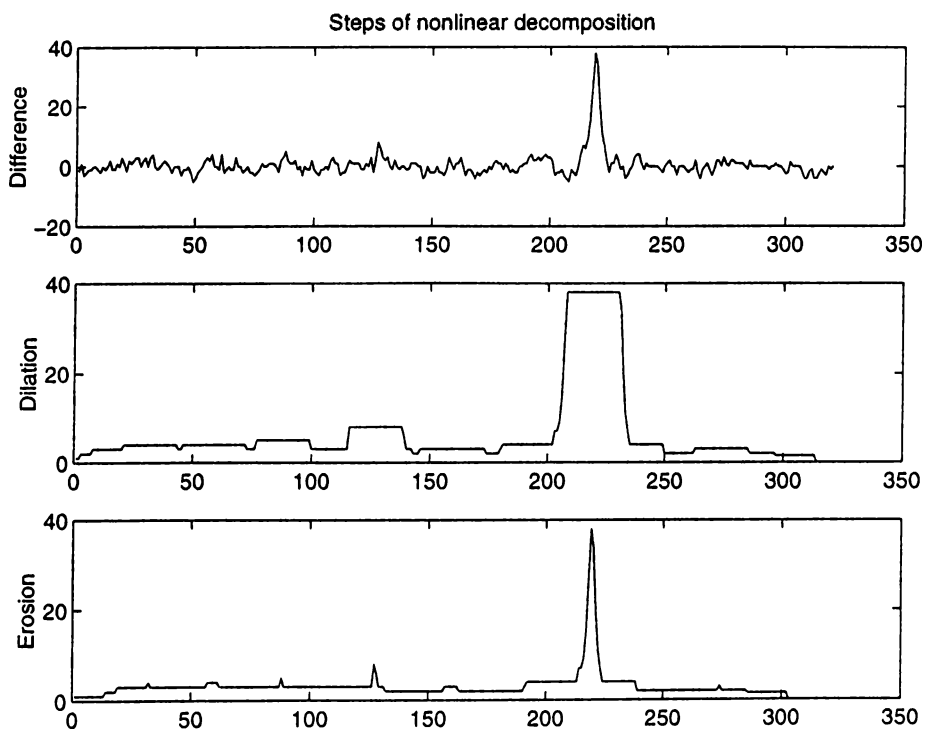


Figure 4.17: Microcalcification segmentation using the closing filtering on the difference image.

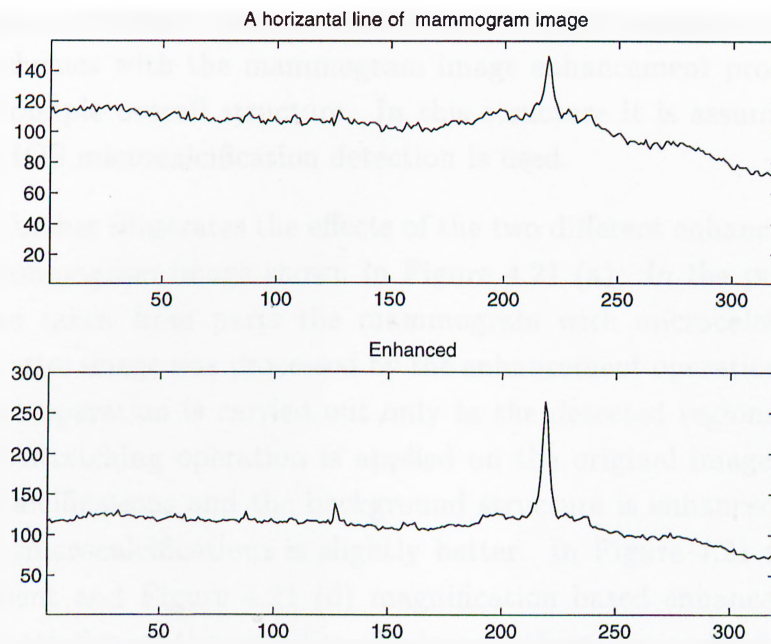


Figure 4.18: Enhancement of the mammogram image by nonlinear subband decomposition.

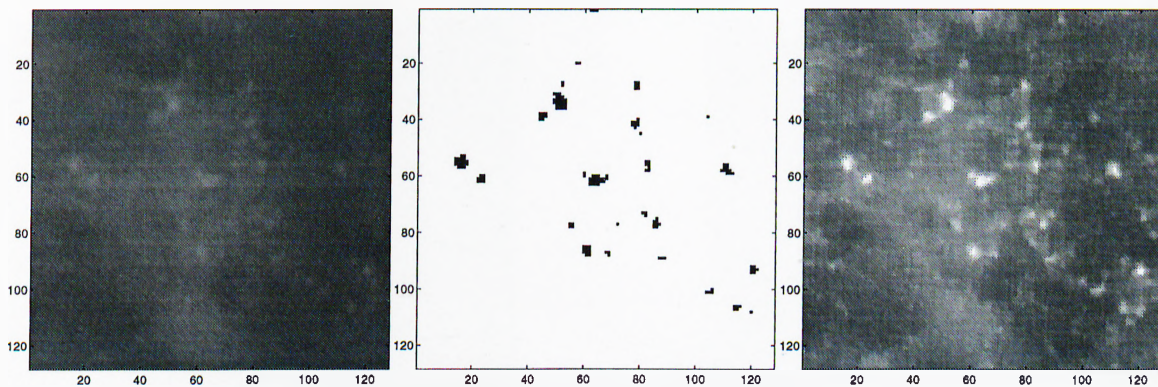


Figure 4.19: Enhancement of mammogram image by nonlinear subband decomposition: (a) A region of a mammogram image containing microcalcifications, (b) output of the segmentation (c) enhanced mammogram image.

Figure 4.18 illustrates the output of the enhancement operation in one dimension using the nonlinear subband decomposition structure. The H filter is chosen as the median filter and G filter is the closing filter. The lengths of these one dimensional filters are 21 and 10, respectively. In Figure 4.19, the result of the mammogram image enhancement is illustrated in two dimensions. The output of the microcalcification segmentation is also included in this figure.

As an overall structure, we can combine the microcalcification detection and segmentation schemes with the mammogram image enhancement process. Figure 4.20 illustrates an example overall structure. In this structure it is assumed that adaptive filtering based HOS microcalcification detection is used.

Figure 4.21 further illustrates the effects of the two different enhancement operations on part of a mammogram image shown in Figure 4.21 (a). In the previous examples, the images were taken from parts the mammogram with microcalcification clusters. Therefore, the entire image was processed by the enhancement operation. In Figure 4.21, the enhancement operation is carried out only in the detected regions. In Figure 4.21 (b) the contrast stretching operation is applied on the original image. In this picture both the microcalcifications and the background structure is enhanced. Therefore, the visibility of the microcalcifications is slightly better. In Figure 4.21 (c) superposition based enhancement and Figure 4.21 (d) magnification based enhancement operations are applied. In both figures the visibility of microcalcifications is significantly enhanced.

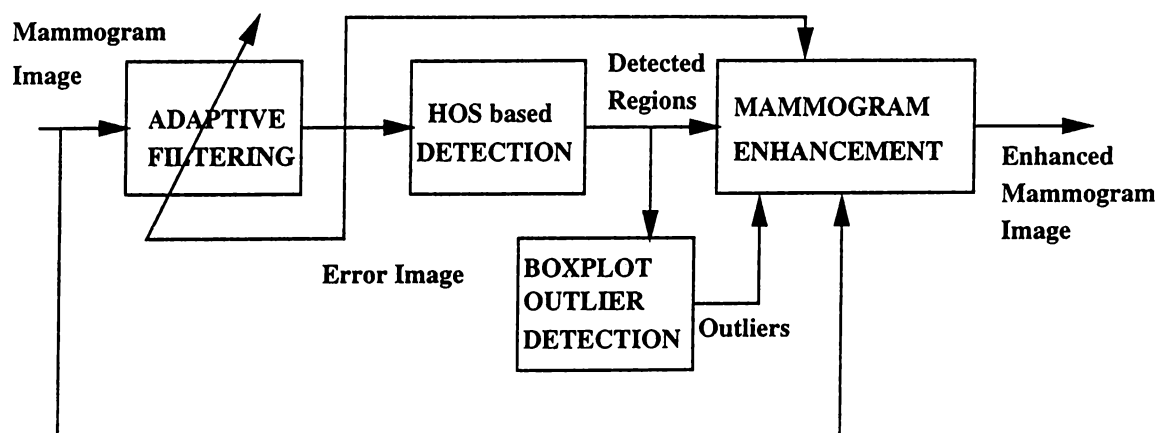


Figure 4.20: Mammogram image enhancement scheme.

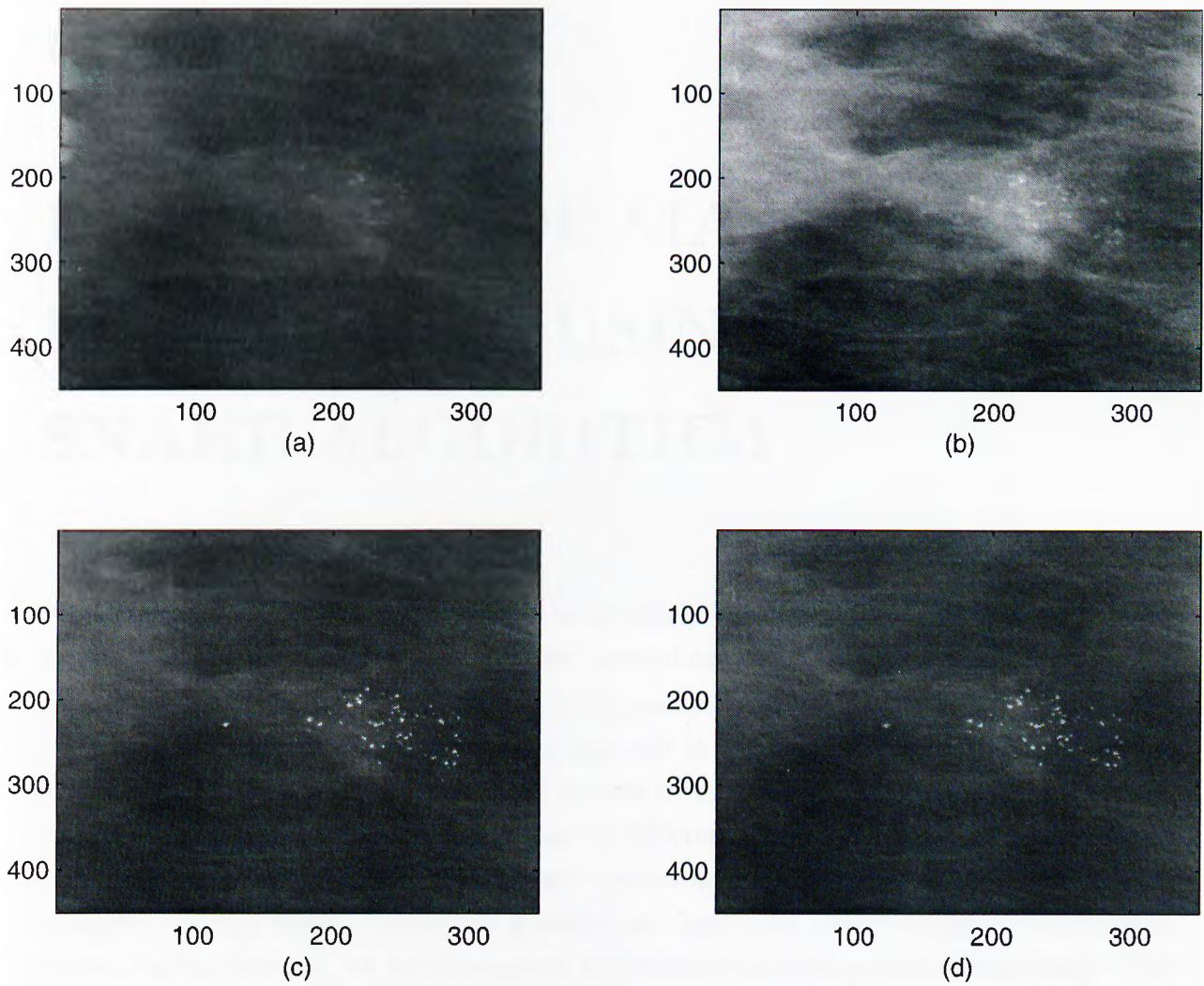


Figure 4.21: Results of mammogram image enhancement: (a) Part of a mammogram image to be enhanced (b) Output of the contrast stretching operation (c) Superposition based enhancement (d) Magnification based enhancement.

Chapter 5

DETECTION OF MASS LESION BOUNDARIES USING THE SNAKE ALGORITHM

While microcalcifications are regarded as an early sign of breast cancer, two types of lesions, namely mass and stellate lesions, are indicators of cancer. In this chapter, the detection of mass lesion boundaries using the snake algorithm is discussed. Detection of boundaries of mass lesions play an important role in the classification of these tumors as malignant or benign. Additionally, the growth of tumor size in time can be monitored more accurately on mammograms taken at different times. In this chapter, we first introduce a recently developed boundary detection scheme. This scheme detects the boundary of the lesion by region growing on fuzzy set pre-processed mammogram images. In our scheme, we use histogram equalization as the pre-processing stage. This stage enhances the mass lesions which usually have a brighter appearance than their surrounding pixels. In the enhanced image, the snake algorithm is used to detect the boundary of the lesion.

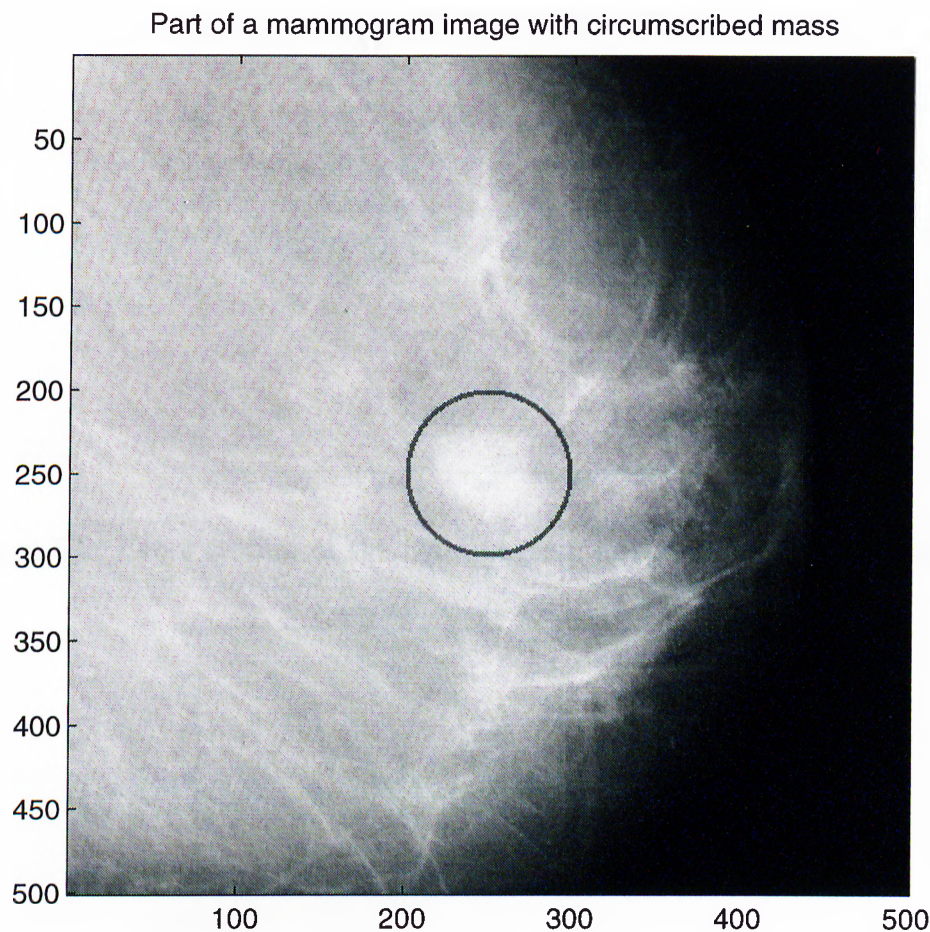


Figure 5.1: Part of a mammogram image with a circumscribed mass lesion.

5.1 Mass Lesion

A mass lesion appears on the mammogram as an almost uniform density, roughly elliptical disk. It is brighter than its surrounding area and its edges are fuzzy. Figure 5.1 shows a region of mammograms containing a mass lesion. The lesion is located at the center of the image. The circle around the mass indicate the extent of the malignancy. The size and shape of the masses differ from one case to another. In most cases, however, masses look very much like the normal breast parenchymal tissue. Hence, their detection is not easy for radiologists since they may examine many mammograms each day and only a tiny fraction of them contain abnormalities such as mass lesions.

Figures 5.2 and 5.3 show the horizontal and vertical cross sections of the mammogram image in Figure 5.1. The cross sections are taken at the location of the mass lesion and

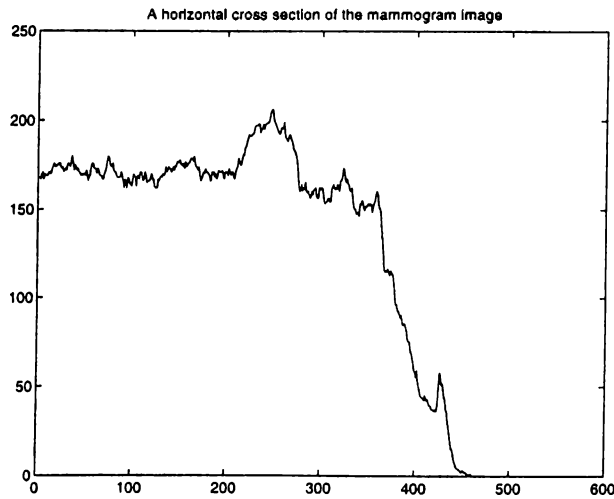


Figure 5.2: Cross section of the mammogram image in horizontal direction.

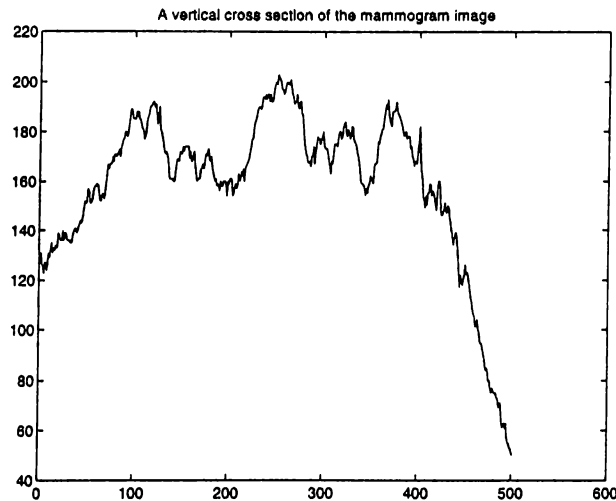


Figure 5.3: Cross section of the mammogram image in vertical direction.

the mass is located in the middle of these plots. These figures indicate that the region with the mass has a high contrast in both directions. However, this does not have to be the case, in general.

After detecting the masses, a lesion classification is carried out according to the shape of the mass. The important factor in the classification are shape-based features such the circularity, the variation of the radial length, and so on. Well-circumscribed, compact and roughly elliptical tumors are usually benign. A tumor, on the other hand, with blurred boundary, irregular shape and with spicules radiating from the center (stellate) are usually malignant.

We propose an algorithm for the accurate delineation of the boundaries of the mass lesions. This algorithm can be utilized both in the mass lesion detection and temporal examinations of mammograms with a mass lesion. In Section 5.2, a recently developed breast boundary detection by fuzzy set pre-processing and region growing is reviewed [59]. Our boundary detection scheme is based on the *snake algorithm* [61, 62]. The snake algorithm is reviewed in Section 5.3. Our mass lesion boundary detection algorithm is described in Section 5.4.

5.2 Breast Boundary Detection by Fuzzy Set Pre-processing and Region Growing

In a recent related work, breast tumor boundary is detected by fuzzy set based pre-processing and region growing [59]. The fuzzy set based pre-processing aims at increasing the pixel values within the mammogram image with values in the range similar those of the mass lesion. This produces an enhanced image, on which a region growing algorithm is applied. In Section 5.2.1 the fuzzy set based pre-processing is introduced. Section 5.2.2 reviews the region growing algorithm and gives a boundary detection example.

5.2.1 Fuzzy Set Pre-processing

In traditional set theory, an object is either a member of a set or not. For *fuzzy* sets there are flexible membership functions. The membership function, Γ , takes the elements in the set and assigns them values between 0 and 1 [60].

In [59], the region of interest (ROI) containing the mass lesion is enhanced by means of an appropriate membership function, Γ . This function evaluates the similarity between the seed pixel (chosen inside the mass lesion) and other pixels inside the ROI.

The membership function used in [59] is

$$\Gamma[m, n] = \frac{1}{1 + \beta|x[m, n] - S|} \quad (5.1)$$

where $x[m, n]$ represents the pixel value of the mammogram image at location (m, n) and S represents the seed value. The constant, β defines the opening of the membership

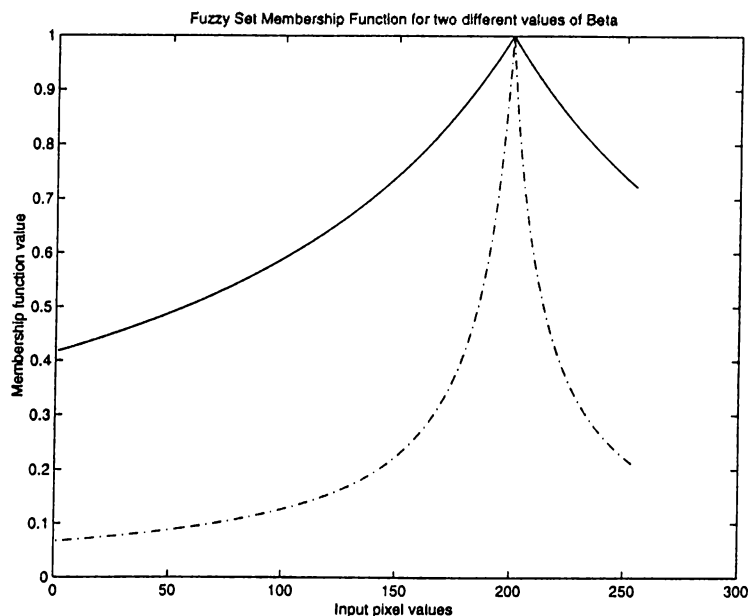


Figure 5.4: Membership functions for two different values of β . $\beta = 0.007$ (Solid line), $\beta = 0.07$ (Broken line).

function. The smaller the value of β , the wider the opening of the function. Figure 5.4 illustrates the membership functions for two different β values. In this plot it is assumed that the seed pixel value S is equal to 200. In [59], β is chosen as 0.007.

The image shown in Figure 5.5(a) is processed by the fuzzy-set based pre-processing. The output of the processed image is given in Figure 5.5(b). The pre-processed image is then linearly converted to a grey-level image whose pixel values range between 0 and 255. The pre-processed image is then input to the region growing algorithm which will be reviewed in the next section.

5.2.2 Region Growing Algorithm

The region growing algorithm is applied on the fuzzy-set pre-processed image to find the boundaries of the breast tumor. The algorithm works in a recursive manner. The inputs to the algorithm are the mammogram image, a location (a seed pixel) within the boundaries of the mass lesion and a threshold, T . The output of the algorithm is a binary image in which the extent of the mass lesion is displayed.

The main parameters in the region growing algorithm are m (mean), t (total), and c

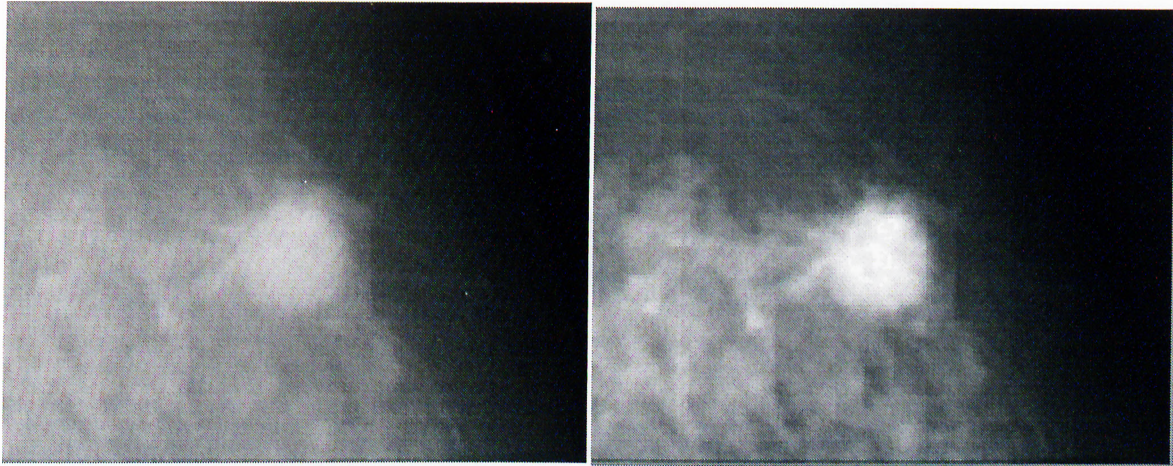


Figure 5.5: (a) Part of a mammogram image containing a mass lesion (b) Fuzzy Set based pre-processing of (a).

(count). The parameter m is the mean value of the marked pixel values, the parameter t is the sum of the pixel values in the marked region, and the parameter c is the count of the number of pixel values in the marked region. Initially, the parameters m and t are equal to the value of the seed pixel, and the parameter c is equal to 1.

The region growing algorithm runs over all pixels within the image. At each iteration, first the current pixel value in the output image is checked. If it is equal to zero, this indicates that either (i) this pixel has not been visited yet, or (ii) it has been visited but the absolute value of the difference between the pixel value and the current m (given by t/c) is greater than the threshold, T . If the absolute difference is less than a set threshold, this pixel value is included in the marked region and the corresponding location in the output image is set to 1. Then, the parameters t and c are updated using the included pixel value. Next, the algorithm runs in four directions (north, south, east, and west) in a recursive manner. Figure 5.6 illustrates the output of the region growing algorithm for the input image given in Figure 5.5(a). In the next section, we propose an alternative snake based boundary detection scheme.

5.3 The Snake Algorithm

Snakes are deformable contour models increasingly used in image segmentation [61, 62]. They are planar curves. The shape and location of the curve is determined according to

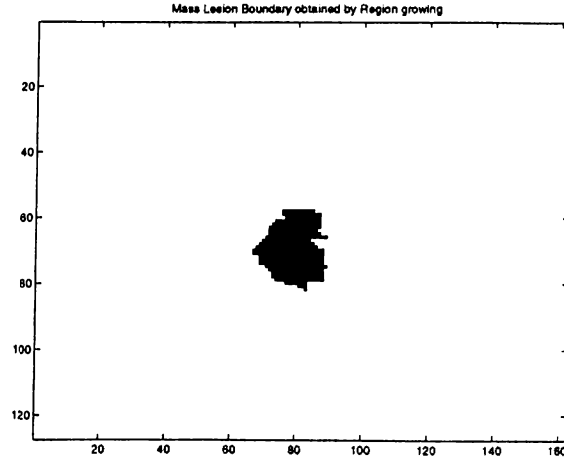


Figure 5.6: Output of the region growing algorithm for the detection of the mass lesion boundaries.

an objective function. Snakes are influenced by image structure and pulled toward the edges and lines on the image. The energy of a snake is defined in a way that its total energy becomes minimum when the snake lies around the region of interest. The total energy of the snake around a closed contour $v(s)$ is defined as:

$$E(v(s)) = \oint_v (E_{int}(s) + E_{ext}(s)) ds \quad (5.2)$$

where E_{int} and E_{out} represent the internal and external energies of the snake, respectively.

The internal energy, E_{int} is determined according to the length and bending of the snake and defined as

$$E_{int}(s) = \alpha \frac{dv}{ds} + \beta \frac{d^2v}{ds^2} \quad (5.3)$$

where the first term denotes the length energy, E_{length} and the second term denotes the bending energy, $E_{bending}$. The weights, α and β control the relative importance of these energy terms in the total energy.

In digital implementation, the length energy is computed simply as the sum of the distances between *snaxels* which are the control points of the snake curve. The curve is determined by the snaxel points and the pixels on the lines connecting the snaxels. In this study the number of snaxels is experimentally determined and a first order (linear) interpolation is used to draw the entire snake curve encircling regions of interest which are mass lesions.

If snaxels on the image, s_i are located at (m_i^*, n_i^*) , for $i = 1, \dots, N$ then the length energy, E_l is computed as

$$E_l = \sum_{i=1}^N \sqrt{(m_i^* - m_{i+1}^*)^2 + (n_i^* - n_{i+1}^*)^2} \quad (5.4)$$

where $m_{N+1}^* = m_1^*$, $n_{N+1}^* = n_1^*$ as the snake is a closed contour.

The bending energy, E_b controls the smoothness of the snake curve. A suitable measure for the smoothness is the second derivative along the contour. The bending energy can be approximated in digital implementation as

$$E_b = \sum_{i=1}^N \sqrt{(m_{i-1}^* - 2m_i^* + m_{i+1}^*)^2 + (n_{i-1}^* - 2n_i^* + n_{i+1}^*)^2} \quad (5.5)$$

where $m_{N+1}^* = m_1^*$, $n_{N+1}^* = n_1^*$, $m_0^* = m_N^*$, $n_0^* = n_N^*$.

The external energy, E_{ext} , represents the energy created by the image structure depending on the location of the snake on the image and it is defined as

$$E_{ext} = w_n E_n + w_e E_e \quad (5.6)$$

where the first term, E_n defines the line energy, the second term, E_e defines the edge energy, and the weights w_n, w_e determine the contribution of line and edge energies to the total energy, respectively. The line energy is computed simply by adding pixel intensity values, $x[m, n]$ on the snake curve.

$$E_n = \sum_{j=1}^M x[m_j, n_j] \quad (5.7)$$

where the index j runs over all the M pixels along the snake curve.

The second external energy component, E_e is basically the gradient approximation of the underlying image along the snake curve.

$$E_e = \sum_{j=1}^M [(x[m_{j+1}, n_j] - x[m_{j-1}, n_j])^2 + (x[m_j, n_{j+1}] - x[m_j, n_{j-1}])^2] \quad (5.8)$$

where the index j runs over all the M pixels along the snake curve. This is not the only form of gradient approximation, however for our purposes it is satisfactory.

1. Get the image $x[m, n]$.
2. Get the initial position of the snaxels, $v[i] = [m[i], n[i]]$, $i = 1, \dots, N$ (number of snaxels).
3. Calculate the total energy of the snake curve, E_{total} .
4. The total energy, E_{total} , is assigned the minimum energy, E_{min} , i.e. $E_{min} = E_{total}$.
5. For each snaxel $v[i]$, $i : 1 \rightarrow N$,
 - 5.1 $E_{min} = E_{total}$.
 - 5.2 For M pixels in the neighborhood of each snaxel, $j : 1 \rightarrow M$,
 - 5.2.1 Calculate the length energy, E_l as in Equation 5.4.
 - 5.2.2 Calculate the bending energy, E_b as in Equation 5.5.
 - 5.2.3 Calculate the line energy, E_n as in Equation 5.7.
 - 5.2.4 Calculate the edge energy, E_e as in Equation 5.8.
 - 5.2.5 $E[j] = E_l + E_b + E_n + E_e$.
 - 5.2.5.1 If $E[j] < E_{min}$,
 - 5.2.5.1.1 The minimum energy is replaced by the new value $E_{min} = E[j]$.
 - 5.2.5.1.2 The snaxel point is replaced by the image pixel, $j = j_{min}$.
 - 5.2.5.1.3 Move the snaxel v_j to $v_{j_{min}}$.
 - 5.3 Calculate the angle, ϕ between two lines connecting three snaxels, $\phi = \text{angle}(i-1, i, i+1)$.
 - 5.4 If $\phi < 90^\circ$,
 - 5.4.1 The snaxel v_i is moved to in between v_{i-1}, v_{i+1} until the angle becomes a wide angle.
 - 5.5 Calculate the distance, d between snaxel pairs $d = \text{distance}(v_i, v_{i+1})$.
 - 5.6 If $d < T(\text{threshold})$,
 - 5.6.1 A new snaxel v_i^* is added in between the snaxels v_i, v_{i+1} .

Table 5.1: The snake algorithm.

Our application is based on the fast greedy snake algorithm described in [64]. The snake algorithm is summarized in Table 5.1. In our algorithm, the important parameters that affect the convergence of the algorithm are the energy coefficients, the search radius and the number of *snaxels* which are the control points of the snake curve. The parameters α , β , w_n , w_e in energy equations are set in such a way that the energy should be minimum on the region of interest.

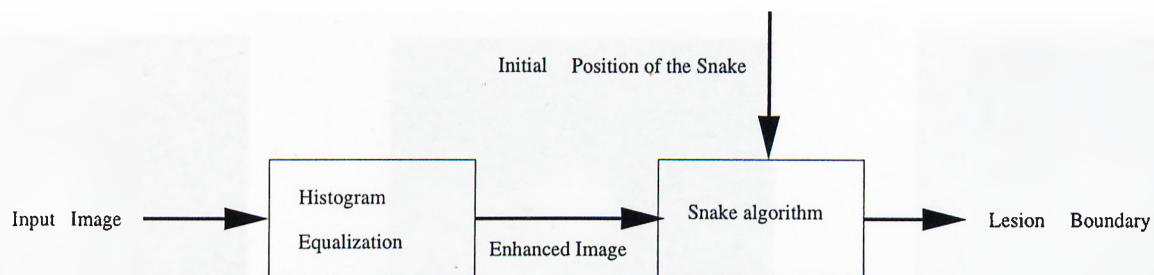


Figure 5.7: The mass lesion boundary detection algorithm.

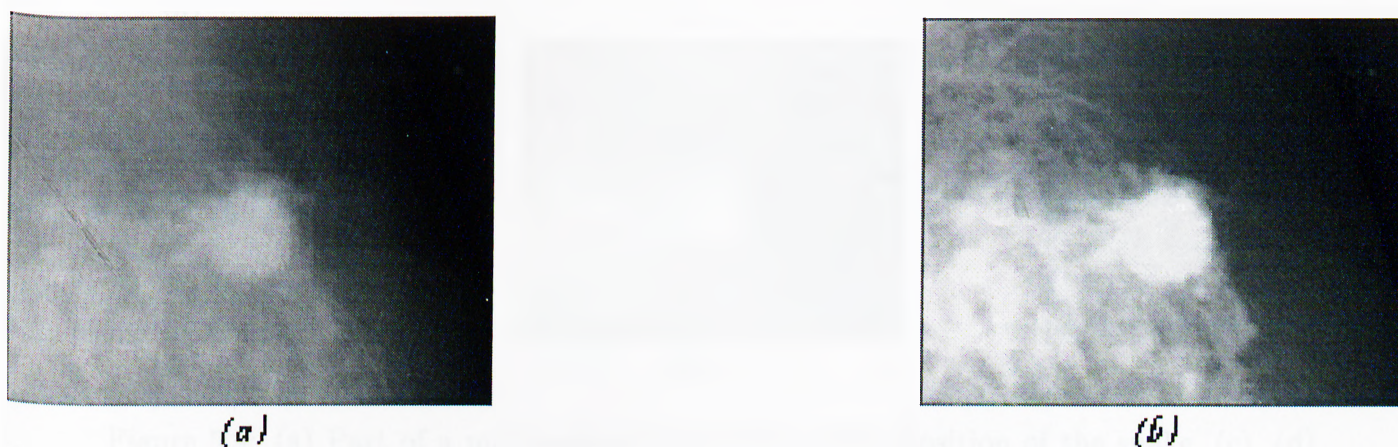


Figure 5.8: (a) Part of a mammogram image containing a mass lesion, (b) after histogram equalization.

5.4 Detection of Mass Lesion Boundaries using the Snake Algorithm

The boundary detection scheme follows the steps given in Figure 5.7. In the pre-processing stage, the image is enhanced through histogram equalization [53]. The mass lesions usually have higher contrast relative to the surrounding pixel values. If this contrast is increased, then a better boundary detection performance can be achieved. One way of increasing the contrast is through histogram equalization. Figure 5.8 illustrates the effect of histogram equalization on part of a mammogram image. As it can be observed from this figure, the contrast of the mass lesion is increased.

The next step in the boundary detection is the snake algorithm. The initial positions of the snaxels are supplied by the user. In our application, the fast greedy algorithm is

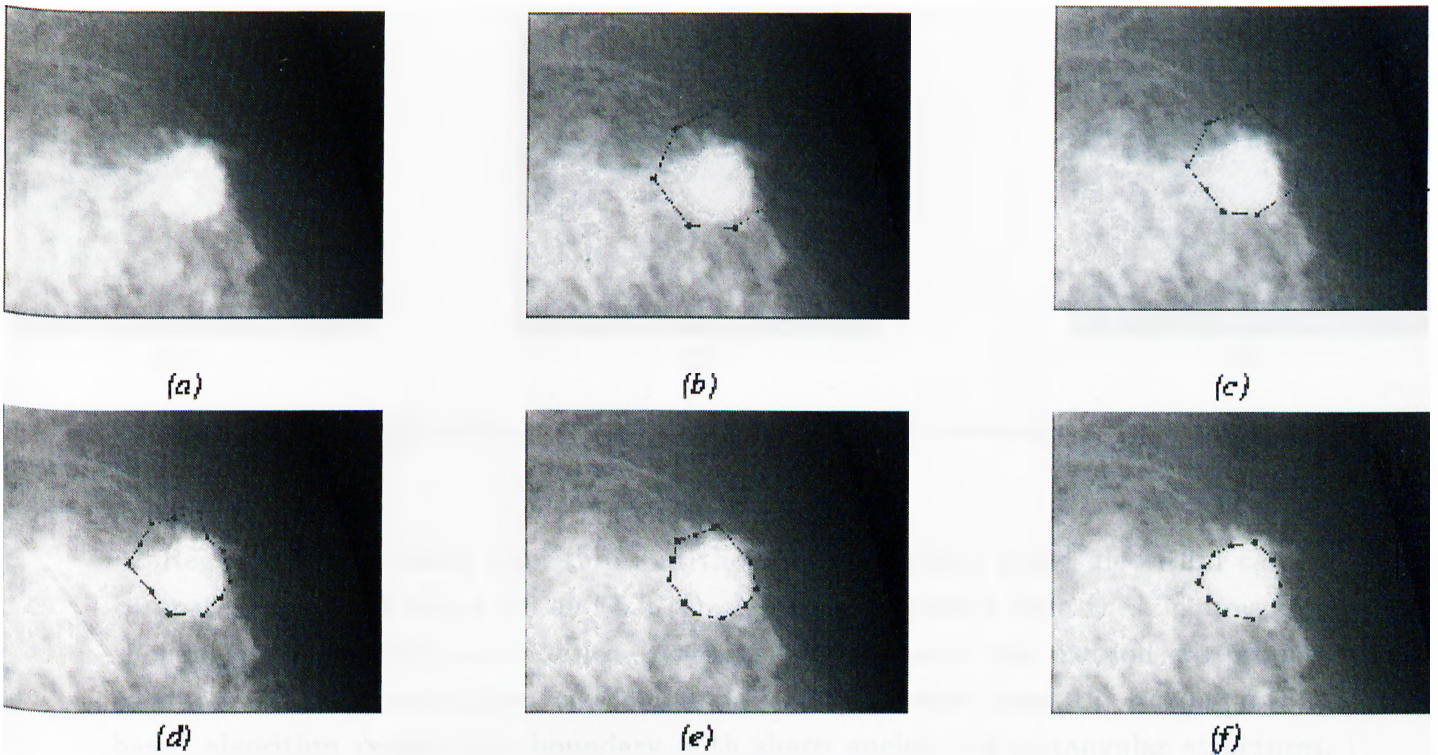


Figure 5.9: (a) Part of a mammogram image (b) Initial position of the snake, (c), (d), (e), (f) The position of the snake at each iteration.

modified for the boundary detection problem. These modifications are summarized in the steps, 5.3 and 5.5 of the algorithm shown in Table 5.1. The first modification is that the angle between the two lines connecting neighboring three snaxels is always kept as a wide angle. At each iteration, these angles are computed and when they are less than 90 degrees, the current snaxel is moved until the angle becomes a wide angle. The second modification concerns the number of snaxels. If the distance between two snaxels exceed a preset distance value, a new snaxel is created in between. These two modifications result in a smooth snake. The values of the constants needed for the snake algorithm are experimentally determined to be $\alpha = 0.1$, $\beta = 0.4$, $w_e = -1$, $w_n = 0.2$. The width of the search window size is set to 8 pixels.

Figures 5.9 and 5.10 indicate that the boundary detection algorithm successfully detects the boundaries of mass lesions [67]. In Figure 5.9, though the snake is initially placed quite outside the mass lesion, the snake encircles the mass region approximately even after the first iteration. Figure 5.10 shows the mass region indicated by the radiologist and the output produced by the snake algorithm.

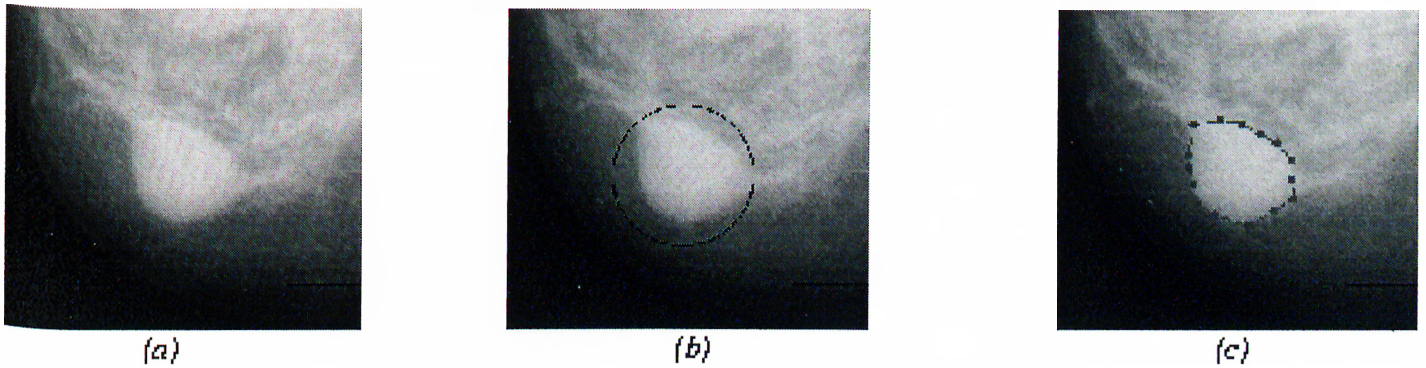


Figure 5.10: (a) Original image (b) Region marked by the radiologist (c) Output of the snake algorithm.

Region growing based algorithm and the snake algorithm based algorithm can be compared through Figures 5.6 and 5.9 (f). It can be observed from these figures that though similar results are obtained by these two methods, the method we propose produces a more smooth curve for the boundary. On the other hand, the region growing based algorithm results in a boundary with sharp angles and rectangular structures. However, a soft boundary is more consistent with the morphological structure of the mass lesions because these abnormalities appear as circular or oval blobs with smooth edges on mammograms [42].

The computational complexity of the dynamic programming based snake algorithm is $O(N \times M^2)$ at each iteration, where N is the number of snaxels in the image and M is number of pixels in the search window [63]. The computational complexity of our application based on the fast greedy algorithm is, on the other hand, only $O(N \times M)$ [64]. This brings in significant computational savings. Furthermore, the algorithm can be implemented faster in a multiresolutional framework as described in Appendix C. The region growing algorithm uses a breadth-first search algorithm, i.e., four neighboring pixels are searched in order to grow the search. Therefore, the computational complexity of this algorithm is $O(P)$, where P is the number of pixels within the boundaries of the mass lesion.

In [68] we use the snake algorithm for the identification of relative protein bands in polyacrylamide gel electrophoresis (PAGE) images which are frequently used in protein research. The snake algorithm was applied in a multiresolutional framework. Experimental studies have shown that the results are more accurate and the method involves less computational complexity if the snake algorithm is applied in this

framework. Appendix C gives a detailed explanation of this framework and the detection results.

Chapter 6

CONCLUSIONS

In this thesis, we propose computer-aided diagnosis methods for the detection and analysis of microcalcification clusters and for the detection of boundaries of mass lesions in mammogram images. Studies indicate that CAD systems increase the performance of radiologists [9], and they will be an important feature of the next generation Picture Archiving and Communication Systems (PACS).

We initially analyzed existing microcalcification detection schemes and we showed that most of these methods first employ a simple bandpass filter to process the mammogram image. Afterwards, they use a simple threshold to detect the microcalcifications which appear as outliers. Instead of simple thresholding, we introduced higher order statistical tests for microcalcification cluster detection. In our algorithm, the image is first bandpass filtered, then the resultant filtered image is divided into overlapping square regions. It is experimentally observed that in regions with no microcalcifications the Gaussian distribution is a good model for the filtered image. In regions with microcalcifications, on the other hand, the distribution is non-Gaussian because of the impulsive nature of microcalcifications. In each square region third and fourth order statistics, skewness and kurtosis values are estimated. Since microcalcifications make the distribution skewed, the tails of the distribution is heavier, and hence these statistics produce high values. Regions with skewness and kurtosis values higher than those thresholds are marked as suspicious regions. Threshold values for skewness and kurtosis are estimated from a training set. In our experiments using this method all of the 105 microcalcification clusters in the Nijmegen mammogram image database are detected

with an average of 3.3 false alarms per mammogram image.

Instead of simple bandpass filtering, adaptive filtering can be used to pre-process the mammogram images. We observed that adaptive prediction is effective to remove the regular breast tissue and the error image contains outliers corresponding to microcalcifications. In our method we use a two-dimensional (2-D) adaptive predictor and a Gaussianity test (OCM) recently developed by Ojeda *et al.* for causal invertible time series. Similar to the previous approach, we divide the image into overlapping square regions and the OCM test statistic of the prediction errors is computed to determine whether the current region contains samples from a Gaussian distribution. Since microcalcifications are isolated bright spots, the prediction sequence deviates from Gaussianity around microcalcification locations. The OCM test is based on the second and third order statistics. The false detection rate of this scheme is 2.3 per image for the same mammogram database. We also analyzed the OCM test using the influence function and sensitivity curve concepts and found out that the OCM test has high sensitivity to outliers.

For our purposes we require a Gaussianity test with high sensitivity so that it can detect microcalcifications which demonstrate outlier characteristics in a better way. Fourth order statistical parameters are also widely used in Gaussianity tests. We designed a test statistic using the second and fourth order moments. The sensitivity analysis shows that the new test statistic has higher sensitivity to outliers than the OCM test. Experimental studies have also shown that this test has better detection performance when combined with the OCM test. It reduces the false alarm rate and the number of single bright spots. In our experiments with the mammogram database containing 40 images, the false alarm rate decreased from 2.3 per image to 1.125 per image. This experimentally justifies the effectiveness of the new Gaussianity test for the microcalcification detection. This result is expected as both the third and the fourth order moments are involved in the detection process. A wavelet decomposition based scheme which uses the same database in the experiments detects all the clusters correctly with an average of 8 false alarms per image. When compared to this scheme, our scheme produces significantly better detection results.

In our microcalcification detection algorithms, the detection is always carried out in overlapping square regions. The benefits of this approach are manifold. First, it enables the use of parallel algorithms for detection purposes. Computations in each region are independent from each other. Another advantage is that within the detected

square regions (instead of the entire image), computationally expensive nonlinear filtering operations and outlier labeling methods can be used in order to segment and obtain individual microcalcification locations. Additionally, mammogram images can be enhanced by superimposing detected abnormalities onto the original mammogram image. We have shown examples of detection and enhancement methods.

Another indication of cancer on mammogram images is the mass lesion. The shape and exact extent of mass lesions can be obtained by snake algorithms. When approximately placed around a mass lesion, the snake iteratively converges to and finally encloses the boundary of the mass lesion. This boundary detection scheme can be combined with another mass detection algorithm which is designed to find only the location but not the extent of the mass lesions. A comparison of the automatically detected mass lesion boundaries on mammograms taken at different time periods can also provide valuable information to radiologists in their diagnosis.

As future work, the adaptive filtering methodology can be adopted to the problem of mass and stellate lesion detection. The mass lesions (and the central part of stellate lesions) are usually smoother regions relative to the surrounding pixel values. Therefore, the output of the adaptive filter is expected to produce small prediction error values in these regions. A suitable set of features can be derived from these error values and these features can be used to detect and segment these abnormalities.

The classification of detected microcalcifications as benign or malignant can be another follow-up work. The classification is usually based on the shape of individual microcalcifications as well as their orientation, shape and intensity variations on the original mammogram image. Another classification scheme can be designed which will classify the abnormalities using the features extracted from subband images or adaptive filter prediction errors. A set of rules needs to be derived in collaboration with radiologists. These rules must be combined and correlated with the computer extracted features to develop a classification tool.

Appendix A

Bandpass Filter Equivalents of Subband Decomposition Structures

Wavelet based subband decomposition has been used in several computer-aided diagnosis methods [6],[10]–[12]. In these methods, first the mammogram image is wavelet transformed. A set of subband images are selected and weighted to enhance the abnormalities. Next, the reconstructed image is thresholded to extract the abnormalities. Figure A.1 illustrates a two-level subband decomposition structure. In this appendix, we show that weighting selected subband images followed by reconstruction is essentially equivalent to bandpass filtering.

Yoshida *et al.* have investigated the effect of different Least Asymmetric Daubhechies' filters with different filter lengths [10]. They conclude that an 8-tap Least Asymmetric Daubhechies' (LAD8) filter gives the best detection results, evaluated using the ROC methodology. The filter coefficients are given in Table A.1. The mammogram image is decomposed up to the third level and ten subimages at various resolutions are obtained. Finally, the second and the third level images are used in the reconstruction. This covers the frequency range $[\frac{\pi}{8}, \pi]$ if the frequency domain is divided in an ideal manner. Therefore, Yoshida's subband decomposition is basically highpass filtering with passband $[\frac{\pi}{8}, \pi]$. Figure A.2 illustrates the amplitude response of the equivalent filter.

In [6], again the same filter (LAD8) is used. The mammogram image is decomposed to seven levels, and each level is weighted by a number. The weights are determined by

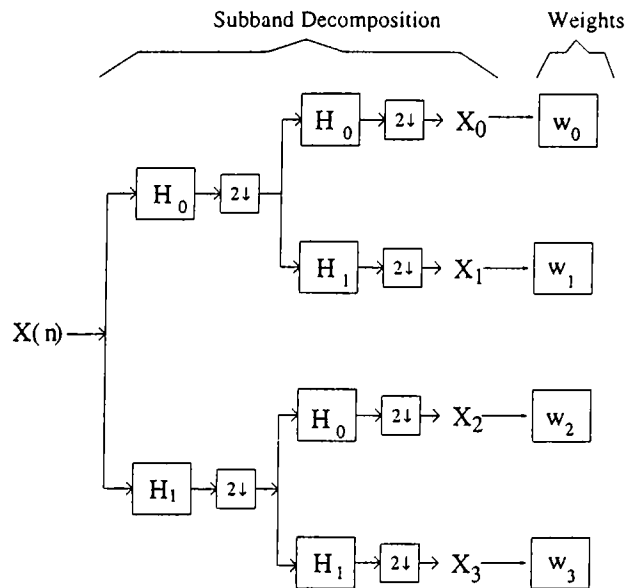


Figure A.1: Binary tree structured 2-level subband decomposition and weighting. The subsignal X_0 contains $[0, \frac{\pi}{4}]$, X_1 contains $[\frac{\pi}{4}, \frac{\pi}{2}]$, X_2 contains $[\frac{3\pi}{4}, \pi]$, X_3 contains $[\frac{\pi}{2}, \frac{3\pi}{4}]$, frequency ranges of the original signal, $X(n)$.

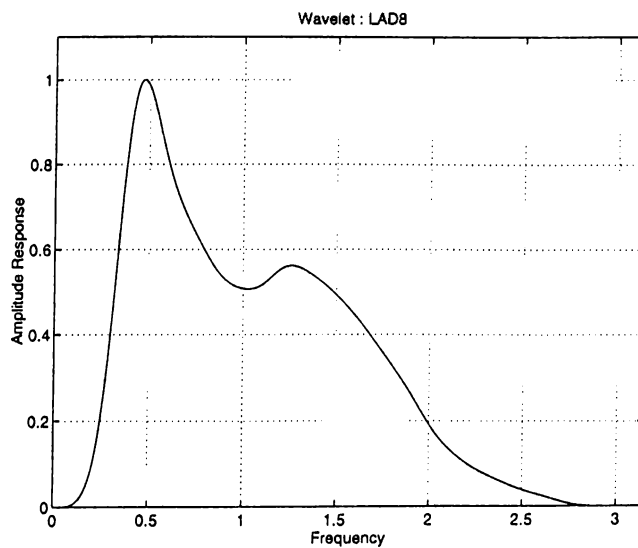


Figure A.2: The overall filter amplitude response using the LAD8 wavelet. Only the the 2nd and 3rd scales are included in the final image [10].

$h[0]$	$h[1]$	$h[2]$	$h[3]$	$h[4]$	$h[5]$	$h[6]$	$h[7]$
-0.1071	-0.0419	0.7037	1.1367	0.4212	-0.1403	-0.0178	0.0456

Table A.1: 8-tap Least Asymmetric Daubhechies' filter coefficients.

w_1	w_2	w_3	w_4	w_5	w_6	w_7
-6.5	9.2	8.8	0.8	0.2	-0.3	0.4

Table A.2: Optimized weights of the wavelet scales.

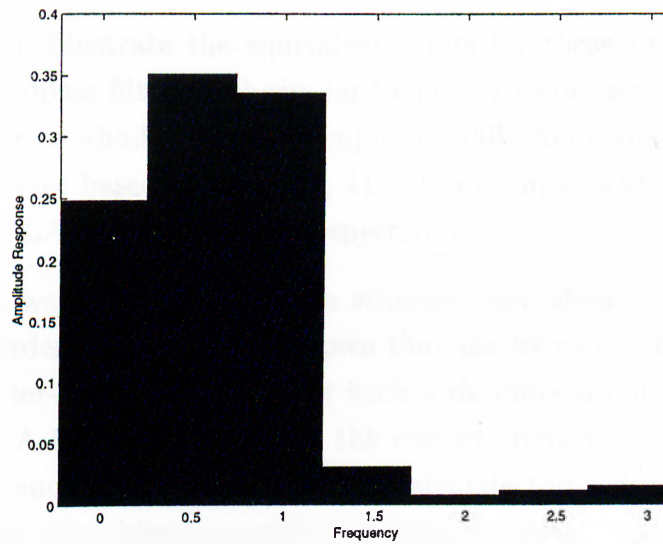


Figure A.3: The ideal filter amplitude response obtained using the weights in Table A.2.

an optimization procedure which uses the Powell's conjugate gradient method for the minimization. The optimal weights are given in Table A.2. Figure A.4 illustrates the equivalent bandpass filter for the subband decomposition structure. Figure A.3 shows the ideal frequency response that would be obtained if the subband decomposing wavelet filters could divide the frequency axis equally. This figure is obtained using the weight functions in Table A.2. The frequency response plotted in Figure A.4 approximates the ideal response shown in Figure A.3.

Strickland and Hahn use the biorthogonal spline wavelet with a filter of length nine [11]. The coefficients of this filter are shown in Table A.3. In another work, Wei *et al.* uses the Least Asymmetric Daubechies' wavelet with 4 coefficients (LAD4) [12].

$h[0]$	$h[\pm 1]$	$h[\pm 2]$	$h[\pm 3]$	$h[\pm 4]$
0.6029	0.2669	-0.0782	-0.0169	0.0267

Table A.3: 9-tap Biorthogonal spline wavelets.

$h[0]$	$h[1]$	$h[2]$	$h[3]$
0.4830	0.8365	0.2241	-0.1294

Table A.4: 4-tap Least Asymmetric Daubechies' filter coefficients.

Figures A.5 and A.6 illustrate the equivalent filters for these two detection schemes. Notice that FIR bandpass filters with similar frequency responses can be designed using ordinary filter design methods [15] and computationally more efficient methods can be obtained as the wavelet based methods [6, 11, 12] are implemented using LAD8, 9-tap biorthogonal spline, LAD4 linear filters, respectively.

In dealing with wavelet decomposition schemes, one should be careful about the choice of subband orders. We have also shown that the frequency bands of the subband signals have a counter-intuitive order after such a decomposition. An example can be observed in Figure A.1. In Appendix B, the correct frequency order of the subband signals is described and an efficient method to calculate the order for a tree-structured subband filter bank with arbitrary number of stages is given.

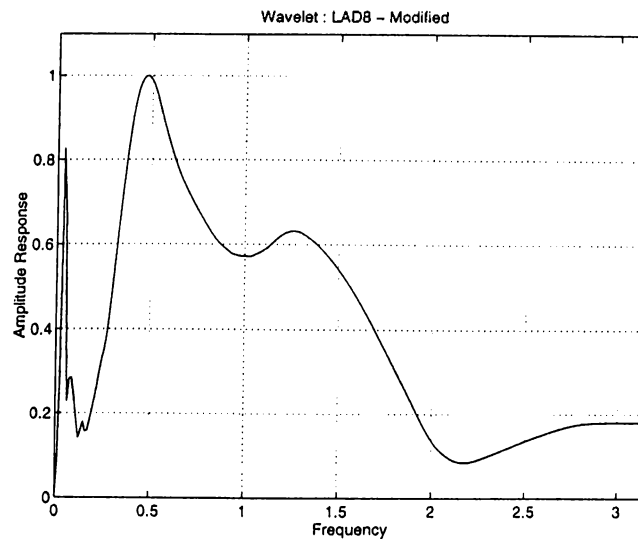


Figure A.4: The overall filter amplitude response using the LAD8 wavelet: Weighted scales [6].

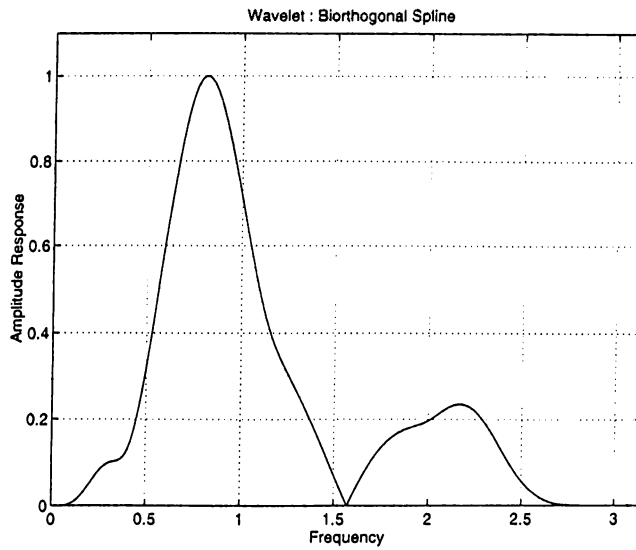


Figure A.5: The overall filter amplitude response using the Biorthogonal Spline wavelet and including the 2nd and 3rd scales [11].

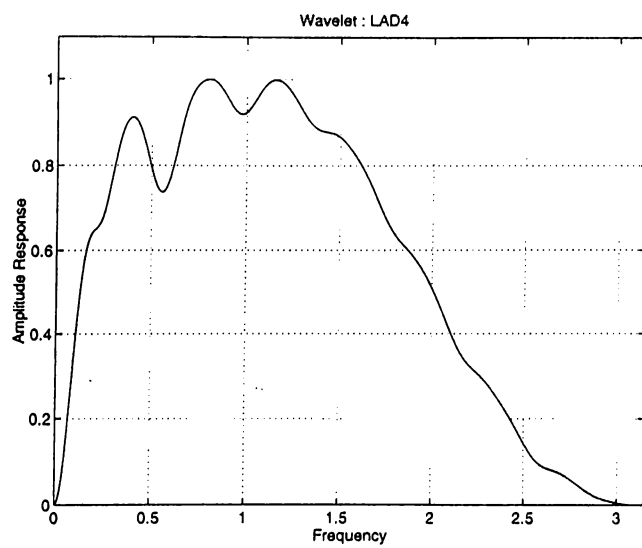


Figure A.6: The overall filter amplitude response using the LAD4 wavelet and including the first 4 scales [12].

Appendix B

Frequency Band Characteristics of Tree-Structured Filter Banks

A subband decomposition filter bank can be recursively used in a tree structure to divide the frequency domain into various subfrequency bands. The frequency bands of the subband signals have a counter intuitive order in such a decomposition. In this appendix, the correct frequency order of the subband signals is described and an efficient method to calculate the order for a tree-structured subband filter bank with arbitrary number of stages is given. It is also shown that the relation between the frequency content and the index of a subband signal can be expressed by an extension of the Gray code [69].

Subband decomposition is widely used in signal analysis and coding [70] - [74]. A large order multi-channel filter bank can be constructed by cascading filter banks with smaller orders. For example, the tree-structured 4-channel filter bank shown in Figure B.1(a) is constructed from two-channel filter banks in two stages. A tree can be formed from binary (two-channel) or m-ary Perfect Reconstruction (PR) filter banks. The frequency contents of the resultant subband signals do not have a natural increasing order for tree structured subband decomposition. The counter intuitive ordering is not emphasized in most of the books on this subject. There are even incorrect band partitioning illustrations in the literature [70] - [72].

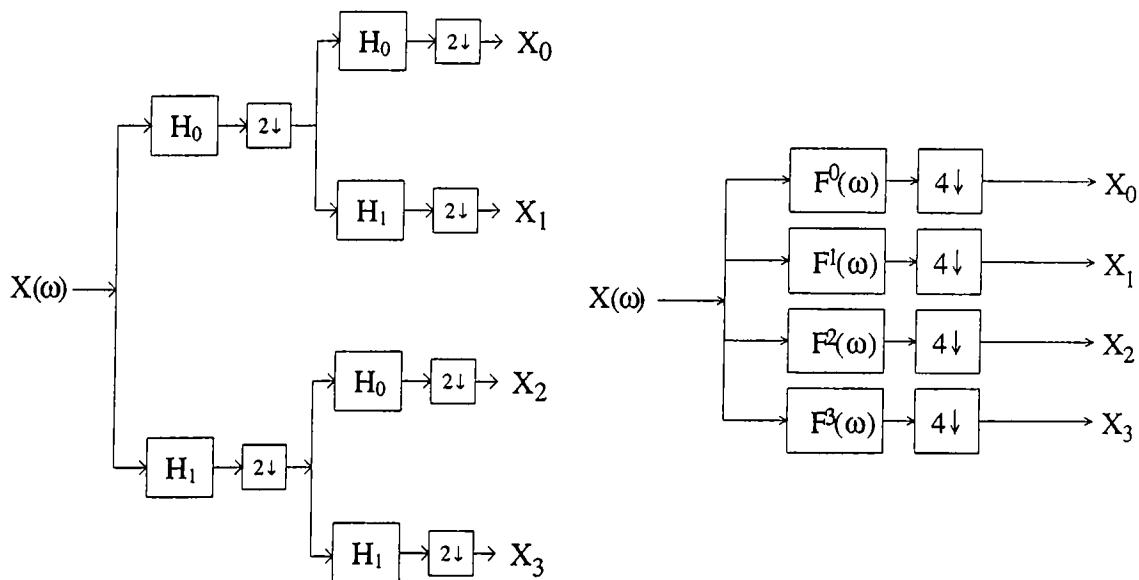


Figure B.1: Binary tree-structured 2-level subband decomposition.

B.1 Binary Tree-structured Subband Filtering

In the 4-channel filter bank structure of Figure B.1(a), $H_0(\omega)$ and $H_1(\omega)$ stands for the low pass and the high pass filters, respectively. An equivalent structure is shown in Figure B.1(b). The two-stage operation in Figure B.1(a) is equivalent to a single stage operation consisting of filtering $x[n]$ by the convolution of filters on the signal path and down-sampling the filtered signal by $2^2 = 4$. The frequency response of the equivalent filter in the first branch is given by

$$F^0(\omega) = H_0(\omega)H_0(2\omega) \quad (\text{B.1})$$

In general the frequency response of $f^k[n]$ in an N stage partition is given by

$$F^k(\omega) = H_{i_0}(\omega)H_{i_1}(2\omega)\dots H_{i_{N-1}}(2^{\ell-1}\omega), \quad k = 0, 1, \dots, N - 1 \quad (\text{B.2})$$

where $k = 2^{\ell-1}i_0 + 2^{\ell-2}i_1 + \dots + i_{N-1}$ and $i_j = 0, 1$.

In Figure B.1 and B.2, the third branch filter $F^2(\omega)$ covers the frequency range $[\frac{3\pi}{4}, \pi]$ whereas the fourth branch filter $F^3(\omega)$ covers the frequency range $[\frac{\pi}{2}, \frac{3\pi}{4}]$. The output signals $X_0(\omega) - X_3(\omega)$ split the frequency band into four regions, but the index ordering from the lowest frequency to the highest frequency is : 0, 1, 3, 2. This sequence represents the Gray code (or minimum change code) ordering [75] where only one bit in the binary

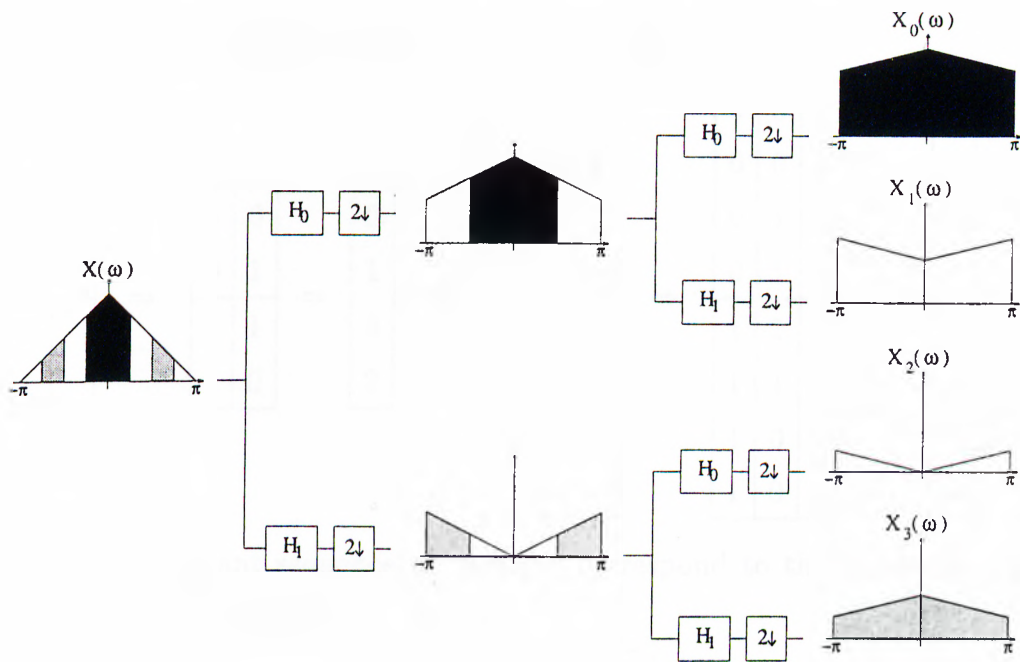


Figure B.2: 4-channel decomposition of a signal.

representation of the number changes between two consecutive numbers. This rule is also valid for higher levels of decomposition.

Consider the generation of binary Gray code in 3 digits. We start with a binary pair in a column $[0 \ 1]^T$. Next, we construct the second digit column by inserting zeros and ones as many times as the number of digits on the right column, i.e. two zeros and two ones. After this stage, the rest of the right column is constructed by warping around the first elements, i.e. the digits are written in the reverse order. The leftmost column is now generated by inserting zeros and ones as many times as the number of digits on the right columns, i.e. four zeros and four ones. At the last stage, the right columns are

filled by periodically warping around the already filled columns :

$$\begin{array}{|c|c|} \hline 0 & 0 \\ \hline 0 & 1 \\ \hline 1 & \\ \hline 1 & \\ \hline \end{array} \Rightarrow \begin{array}{|c|c|} \hline 0 & 0 \\ \hline 0 & 1 \\ \hline 1 & 1 \\ \hline 1 & 0 \\ \hline \end{array} = \begin{array}{|c|} \hline 0 \\ \hline 1 \\ \hline 3 \\ \hline 2 \\ \hline \end{array} \Rightarrow \begin{array}{|c|c|c|} \hline 0 & 0 & 0 \\ \hline 0 & 0 & 1 \\ \hline 0 & 1 & 1 \\ \hline 0 & 1 & 0 \\ \hline 1 & & \\ \hline 1 & & \\ \hline 1 & & \\ \hline 1 & & \\ \hline \end{array} \Rightarrow \begin{array}{|c|c|c|} \hline 0 & 0 & 0 \\ \hline 0 & 0 & 1 \\ \hline 0 & 1 & 1 \\ \hline 0 & 1 & 0 \\ \hline 1 & 1 & 0 \\ \hline 1 & 1 & 1 \\ \hline 1 & 0 & 1 \\ \hline 1 & 0 & 0 \\ \hline \end{array} = \begin{array}{|c|} \hline 0 \\ \hline 1 \\ \hline 3 \\ \hline 2 \\ \hline 6 \\ \hline 7 \\ \hline 5 \\ \hline 4 \\ \hline \end{array} \quad (\text{B.3})$$

Notice that the resultant sequence of numbers correspond to the frequency regions of the subband signals (Figure B.2).

B.2 Arbitrary Tree-Structured Subband Filtering

A PR subband tree can have different number of branches at each stage. In the case of trees with m-ary branches, the frequency contents of the subsignals can be determined by an extension of the Gray code. In this case, the m-ary minimum change code can be constructed by changing only one digit in the m-ary representation of the number.

In the construction of the minimum change codes, the sequence of the right digits in the m-ary representation gets periodically warped. This indicates that the ordering gets shuffled after two stages in the tree. In a tree-structured subband decomposition, the same frequency warping can be observed (Figure B.2).

In the most general case, the hybrid minimum change codes should be used. These codes are constructed by changing only one digit of the hybrid m-ary representation of the number. For instance, if the first stage is binary and the second stage is ternary, then the new code is generated by one digit changes of mod-2 in the most significant digit and one digit changes of mod-3 in the least significant digit. This algorithm can be visualized in a tree-structured manner as in Figure B.3. In this figure, the tree is generated by recursively attaching ternary branches. When a node is labeled with an "R", that means the labels of the branch which is emitted from that node is in reverse order. The final index is determined by tracing the digits starting from the top to the

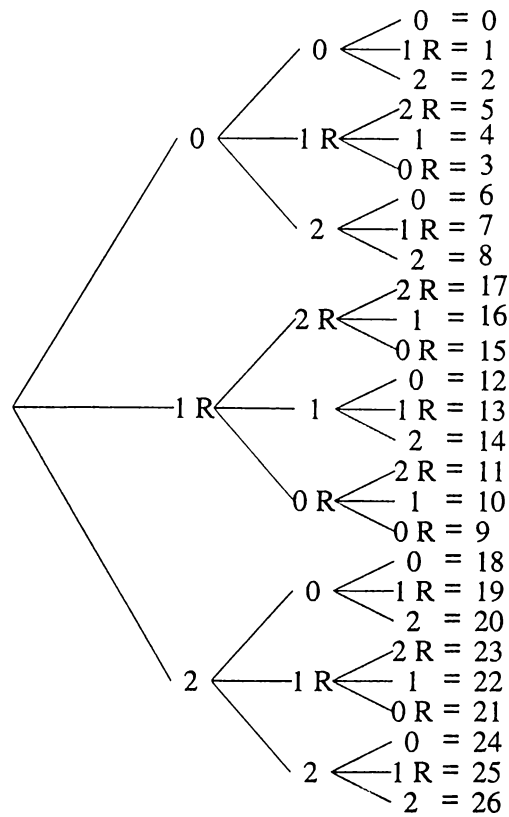


Figure B.3: Tree structure generation of a ternary Gray code.

bottom of the tree.

If the subband tree is composed of layers of m-ary and n-ary branches, the codeword generation works in a similar way. Each digit for the codeword is in modulo-m for the layer corresponding to the m-ary branch and it is in modulo-n for the layer corresponding to the n-ary branch. Suppose the first branch is ternary, and it is followed by binary branches at each node. This time, the code generation is as follows :

$$\begin{array}{|c|} \hline 0 \\ \hline 1 \\ \hline \end{array} \Rightarrow \begin{array}{|c|c|} \hline 0 & 0 \\ \hline 0 & 1 \\ \hline 1 & \\ \hline 1 & \\ \hline 2 & \\ \hline 2 & \\ \hline \end{array} \Rightarrow \begin{array}{|c|c|} \hline 0 & 0 \\ \hline 0 & 1 \\ \hline 1 & 1 \\ \hline 1 & 0 \\ \hline 2 & 0 \\ \hline 2 & 1 \\ \hline \end{array} = \begin{array}{|c|} \hline 0 \\ \hline 1 \\ \hline 3 \\ \hline 2 \\ \hline 4 \\ \hline 5 \\ \hline \end{array} \tag{B.4}$$

Visually, this corresponds to the tree in Figure B.4. When different number of branches

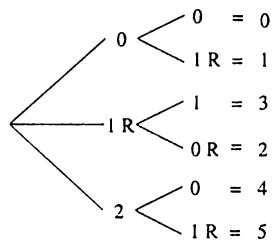


Figure B.4: A hybrid tree structure.

exist at the same layer in the decomposition, the calculation of the frequency order is carried out separately for each branch.

Appendix C

Identification of Relative Protein Bands in Polyacrylamide Gel Electrophoresis (PAGE) Using Multiresolution Snake Algorithm

Polyacrylamide Gel Electrophoresis (PAGE) is one of the most widely used techniques in molecular biology [76]. Denaturing Sodium Dodecyl Sulfate Polyacrylamide Gel Electrophoresis (SDS-PAGE) is an important method used for the separation of proteins based on the migration of negatively charged proteins depending on their molecular weight in an electrical field. Its advantage is that proteins can be visualized as well as separated. The SDS-PAGE technique provides information about the degree of purity of a particular protein in a protein mixture applied on a certain lane of the PAGE during protein purification process. Each band in the SDS-PAGE image represents a different protein.

In the protein purification process, it is important to determine the efficiency of each purification step in terms of percentage of protein of interest found in the protein mixture. This appendix provides a rapid and reliable way to determine the percentage. Generally, the percentage is determined by eye and the results are quite subjective. In the currently available computer-assisted gel analysis systems, the analysis is usually based on the one

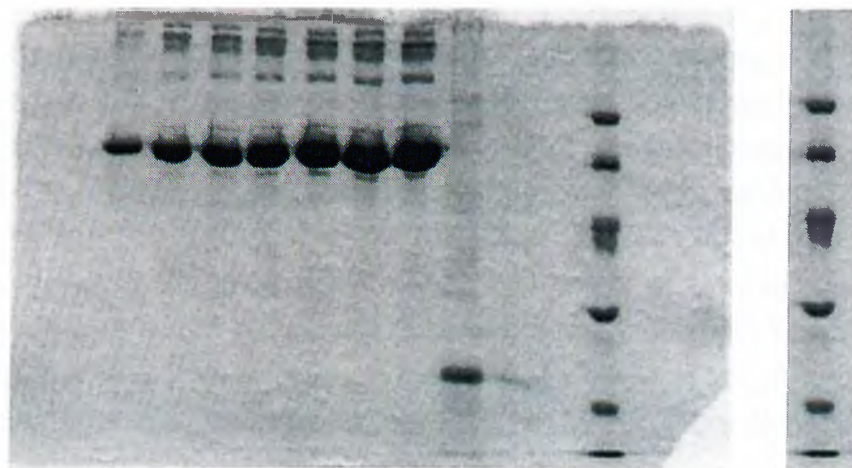
dimensional profile of manually (by computer mouse) extracted lanes. The band of the protein of interest is determined from the peak points in the horizontal profile and the areas of the rectangular regions are measured. Finally, these measurements are used for purification efficiency calculation. However, rectangular approximations are not accurate representations of the ellipse like protein regions.

In our scheme, the region of interest containing the significant protein is detected using the snake algorithm [61]. A snake is loosely placed around the protein band as an ellipse. Then, the snake shrinks itself until it closely encircles and fits around the protein band. The final position of the snake determines the extent of the protein. The iterative snake algorithm is implemented in a multiresolutional framework. The snake is initialized on a low resolution image. Then, the final position of the snake at the low resolution is used as the initial position in the higher resolution image. The area of the protein is estimated as the area enclosed by the final position of the snake.

C.1 Methods

Figure C.1(a) shows a typical SDS-PAGE gel image. The vertical lines containing several protein bands in this gel image are called lanes and one of them is shown in Figure C.1(b). The SDS-PAGE image is composed of three parts. The background does not carry any useful information. The second part corresponding to the images of protein bands have darker appearance. The proteins of interest appear as dark bands and constitute the third part. The ratio of total area of the purified protein band region to the total area of other proteins demonstrates the efficiency of each purification step. The histograms of the three regions corresponding to the significant protein, other proteins and the background on a typical lane are given in Figure C.2. The histograms of the regions are obtained by manually segmenting the SDS-PAGE image.

The regions containing protein of interest are nearly ellipse like regions which have the smallest gray level on the image. Thus, the boundary of such a region is an ellipse like closed contour having small total intensity and high gradient. Our application is again based on the fast greedy snake algorithm described in [64]. Initially six snaxels are placed evenly around a circle determined by the peaks of the one-dimensional profile.



(a)

(b)

Figure C.1: (a) Denaturing PAGE image, (b) a lane of the denaturing PAGE image.

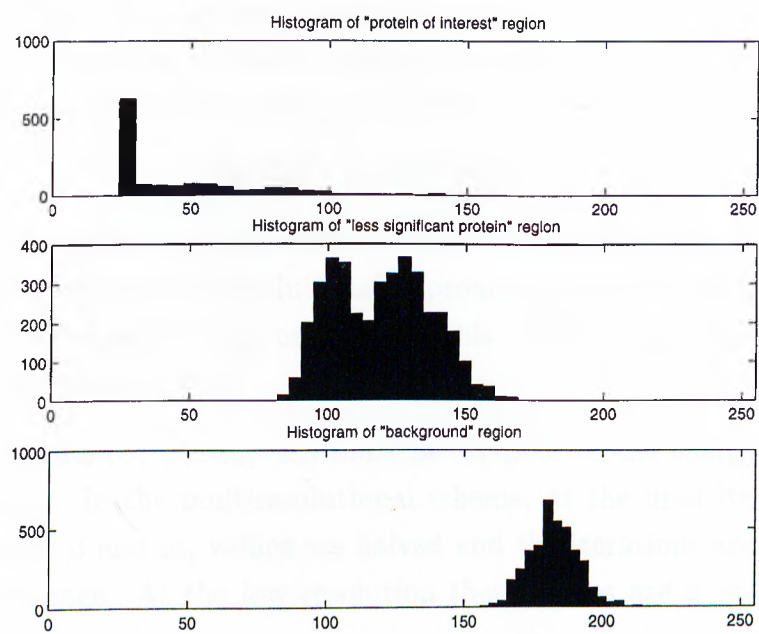


Figure C.2: Histograms of three different regions of a PAGE image.

C.2 Results

The snake algorithm is implemented in a multiresolution framework or in the wavelet transform domain [79]. The original SDS-PAGE image is first processed by the filter banks described in [74, 78] and low resolution quarter size sub-images, x_{ll} , x_{lh} , x_{hl} , x_{hh} are obtained (The indices, l and h represent, ‘low’ and ‘high’ subband, respectively). The snakes are initialized on the low-low sub-image, x_{ll} . The initial form of the snakes are circles centered at the peak points of the 1-D profile of the lane image. Another initialization is based on the x_{lh} , x_{hl} , x_{hh} sub-images which contain the edge information about the original SDS-PAGE image. Therefore, the edges of the protein band region can be detected from these sub-images and used as the initial positions of the snakes.

After the initialization on the low resolution image, the snake adapts itself to the contour around the protein band in an iterative manner. The final snake obtained on the low resolution image is used as the initial estimate on a finer resolution SDS-PAGE image. This process is repeated until the snake has closely covered the protein band region in the original full-resolution SDS-PAGE image.

The behavior of the different energy components and the total energy of a snake at several iterations at different resolutions are given in Figure C.3 for the SDS-PAGE image shown in Figure C.1. At the beginning of the convergence process, the slope of the total energy of the snake in the low resolution image, E_{low} is higher than that of the snake in the high resolution image, E_{high} as shown in Figure C.3(d). In other words,

$$\left| \frac{E_{low}[k+1]}{E_{low}[k]} \right| > \left| \frac{E_{high}[k+1]}{E_{high}[k]} \right| \quad (C.1)$$

This means that the snake converges faster on the low resolution image. This observation verifies the validity of the multiresolutional approach. In our simulation studies we use only one level of sub-band decomposition but this methodology can be considered in multiple resolution levels as well.

The energy weights (α , β , w_n , w_e) must be adapted to the energy level changes in different resolutions. In the multiresolutional scheme, at the final iteration of the low resolution image, α , β and w_n values are halved and the iterations are continued in the higher resolution image. At the low resolution these values are $\alpha = 4$, $\beta = 4$, $w_n = 0.2$, $w_e = -0.1$.

Figure C.4 shows an original lane of the image as well as the final positions of different snakes obtained using different methodologies. The result in Figure C.4(c) is obtained

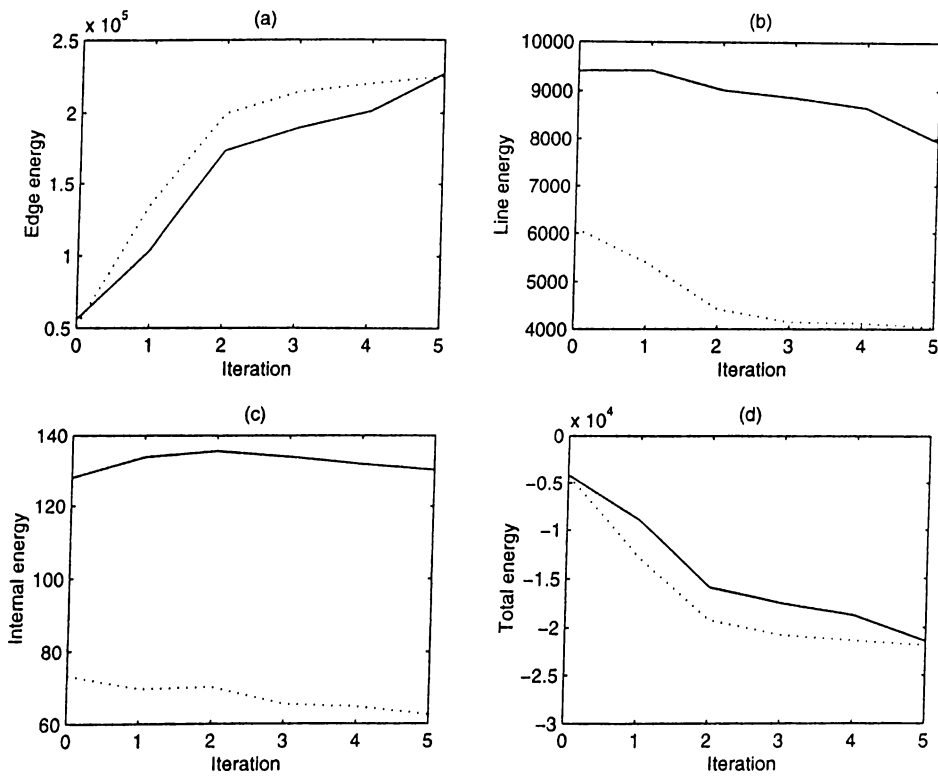


Figure C.3: Change of different energy components. Solid lines indicate the energy changes in the high-resolution image and dashed lines show the energy changes in the lower-resolution image.

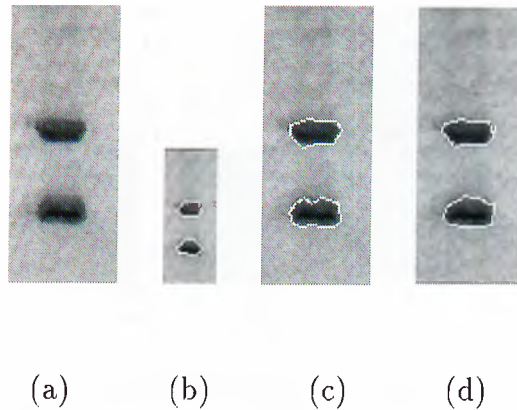


Figure C.4: Protein of interest is enclosed within the snake : (a) Original lane image (b) Snake obtained using only the low-resolution image (c) Snake obtained using only the high-resolution image (d) Snake obtained using the multi-resolutional approach.

after six iterations of the snake algorithm on the original image. Figure C.4(d) shows the result of the multi-resolutional approach. The snake obtained at the low resolution after two iterations (shown in Figure C.4(b)) is used as the initial position of the snake in the high resolution image. Another three iterations in the high resolution image result in Figure C.4(d). The comparison of Figures C.4(c) and (d) indicates that the final snake converges better to the boundary of the protein area if a multi-resolutional approach is used. Additionally, the number of computations required in the multi-resolutional approach is smaller.

Figure C.5 shows the results of the initialization procedure based on the edge information extracted from x_{lh} , x_{hl} , x_{hh} sub-images. Figure C.5(A) depicts the initial position of the snake at the sub-image x_{ll} . The six snaxels are located on the extracted edges of the protein region. This snake takes the form shown in Figure C.5(b) after only one iteration. This form is very close to the final position of the snake on the low-resolution image obtained with the other initialization procedure based on the 1-D profile of the lane image. Figure C.5(c) shows the final position of the snake on the high resolution image after two iterations. There is no significant difference between this result and the result shown in Figure C.4(d) obtained with the other initialization procedure. Edge information based initialization procedure produce similar results with less number of iterations. However, this initialization procedure requires the extraction of edges from the sub-images.

The ratio of the amount of protein of interest to the amount of insignificant proteins

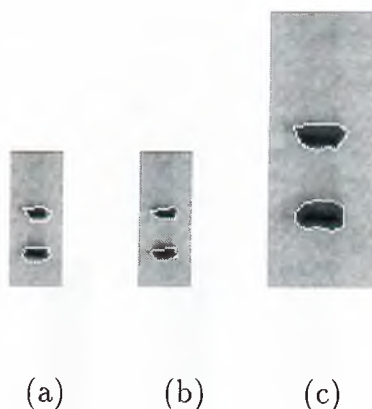


Figure C.5: Results of the initialization process : (a) Initial position of the snake located on the extracted edge (b) The snake in (a) after one iteration on low-resolution image (c) Snake obtained using the multiresolutional approach with the initial snake in (c).

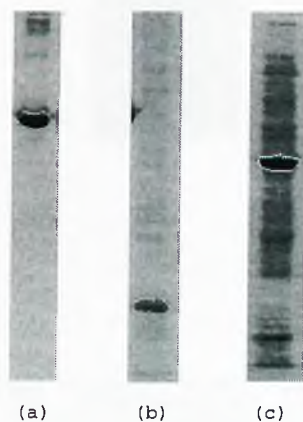
is estimated by the formula

$$100 \times \frac{A_S}{A_T} \quad (\text{C.2})$$

where A_S is the area of the region enclosed by the snake, that is the region of protein of interest; A_T is the total area of the protein band images. The area, A_T is estimated by counting the number of pixels representing all protein band regions which have gray level values smaller than a threshold value. The threshold is calculated using the one-dimensional vertical profile of lanes. The profile is calculated by taking the average of pixel intensity values along the horizontal direction and the threshold is determined according to the maximum gray level in the profile. The effect of noise in the image is reduced by the averaging operation. Once the peak values are determined according to the initial threshold, the snake algorithm determines the boundaries automatically.

Using this methodology, the percentage of protein of interest is estimated in the examples shown in Figure C.6 (a), (b), (c). In all three images, the snake closely encircles the band of protein of interest. The percentages are found to be 82.73%, 80.72%, 22.35%, for the lanes in Figure C.6 (a), (b), (c), respectively. The percentages are estimated as 90%, 80%, 20% by eye, respectively. These are tabulated in in Figure C.6 (d). In the first example (Figure C.6 (a)) our software provides more accurate concentration estimates of protein of interest.

Our method outperforms a commercially available software program which determines the bands by thresholding and rectangular approximation. In an additional experiment, we compared the protein band ratios using our algorithm and the commercial



LANE	OUTPUT OF OUR PROGRAM(%)	EYE ESTIMATE (%)
(a)	82.73	90
(b)	80.72	80
(c)	22.35	20

(d)

Figure C.6: Different regions of interest for percentage calculations shown in (a) , (b), (c) Percentage calculations of our program are compared with the eye estimate of a molecular biologist.



(a)

Lane	Actual protein ratio (%)	Our program (%)	Commercial software (%)
1	17.95	20.83	24.41
2	33.33	27.33	27.77
3	12.82	11.43	18.17
4	35.90	40.40	29.64

(b)

Figure C.7: (a) Known amounts of protein bands determined by Bradford protein assay, (b) Comparisons of percentage calculations of our software and a commercial software.

software for known amounts of protein determined by Bradford protein assay [77] for each protein band separately. The results are shown and tabulated in Figure C.7. The actual percentages are 17.95%, 33.33%, 12.82%, 35.90%. Our software estimates them as 20.83%, 27.33%, 11.43%, 40.40%, compared to 24.41%, 27.77%, 18.17%, 29.64% as estimated by the commercial software. The squared values of the differences between the actual percentages, and the results of our program and the commercial program are 66.47 and 140.45, respectively. This indicates that our software provides better results than the commercially available software.

Resolution	Edge	Line	Length	Bending
High	3517	3517	648	324
Low	756	756	132	66

Table C.1: Number of computations for high and low resolution

C.3 Discussion

The advantage of this multiresolutional approach is three-fold: i) The snake algorithm converges better, ii) it brings robustness to the process, i.e., it is not easily affected by the scanning artifacts in the original SDS-PAGE image, and iii) computational cost is less as smaller images are processed in lower resolutions.

The computational complexity of our application based on the fast greedy algorithm is only $O(NM)$ where N is the number of snaxels in the image and M is number of pixels in the search window [64]. Table C.1 shows the number of times each energy component is computed on high and low resolution images at the last iteration. The total number of energy component computations in the low resolution image is reduced to approximately $\frac{1}{4}$ th of that in the high resolution image.

The multiresolutional snake framework may also find applications in other electrophoretic techniques that require comparative band image quantifications.

Bibliography

- [1] H. Chan, S. B. Lo, B. Sahiner, K. L. Lam, and M. A. Helvie, "Computer-aided detection of mammographic microcalcifications: Pattern Recognition with artificial neural network," *Med. Phys.*, vol. 22, no. 10, October 1995.
- [2] H. Chan, K. Doi, S. Galhotra, C. J. Vyborny, H. MacMahon, and P. Jokich, "Image feature analysis and computer-aided diagnosis in digital radiography, I. Automated detection of microcalcifications in mammography," *Medical Physics*, pp. 538-547, vol. 14, no. 4, Jul/Aug 1987.
- [3] T. O. Gulsrud and S. Kjode, "Optimal filter for detection of stellate lesions and circumscribed masses in mammograms," *SPIE Visual Communications and Image Processing'96*, Orlando, Florida, vol. I, pp. 430-440, 17-20 March, 1996.
- [4] R. N. Strickland and H. I. Hahn, "Wavelet Transforms for Detecting Microcalcifications in Mammograms," *IEEE Trans. on Medical Imaging*, vol. 15, no. 2, pp. 218-229, April 1996.
- [5] K. S. Woods, C. C. Doss, K. Bowyer, J. L. Solka, C. E. Priebe, and W. P. Kegelmeyer JR, "Comparative Evaluation of Pattern Recognition Techniques for Detection of Microcalcifications in Mammography," *International Journal of Pattern Recognition and Artificial Intelligence*, vol. 7, no. 6, pp. 1417-1436, 1993.
- [6] H. Yoshida, W. Zhang, W. Cai, K. Doi, R. M. Nishikawa, and M. L. Giger, "Optimizing Wavelet Transform Based On Supervised Learning For Detection of Microcalcifications in Digital Mammograms," *Proceedings of IEEE International Conference on Image Processing*, pp. 152-155 1995.

- [7] A. P. Dhawan, Y. Chitre, C. Kaiser-Bonnasso, and M. Moskowitz, "Analysis of Mammographic Microcalcifications Using Gray-Level Image Structure Features," *IEEE Trans. on Medical Imaging*, vol. 15, no. 3, pp. 246-259.
- [8] L. P. Clarke, M. Kallergi, W. Qian, H. Li, R. A. Clark, and M. L. Silbinger, "Tree-structured non-linear filter and wavelet transform for microcalcification segmentation in digital mammography," *Cancer Letters*, vol. 77, pp 173-181, 1994
- [9] H. P. Chan, K. Doi, C. J. Vyborny, R. A. Schmidt, C. E. Metz, K. L. Lam, T. Ogura, and H. MacMahon, "Improvement in radiologists' detection of clustered microcalcifications in mammograms," *Investigative Radiology*, vol. 25, pp. 1102-1110, October 1990.
- [10] H. Yoshida, K. Doi, and R. M. Nishikawa, "Automated detection of clustered microcalcifications in digital mammograms using wavelet transform techniques," *Proc. SPIE*, 2167:868-886, 1994.
- [11] R. N. Strickland and H. I. Hahn, "Wavelet Transform Matched Filters For the Detection and Classification of Microcalcifications in Mammography," *Proceedings of IEEE International Conference on Image Processing*, pp. 422-425 1995.
- [12] D. Wei, H. Chan, M. A. Helvie, B. Sahiner, N. Petrick, D. D. Adler, and M. M. Goodsitt, "Classification of mass and normal breast tissue on digital mammograms: Multiresolution texture analysis," *Med. Phys.*, vol. 22, no. 9, pp. 1501-1513, 1995.
- [13] J. Kilday, F. Palmieri, and M. D. Fox, "Classifying Mammographic Lesions Using Computerized Image Analysis," *IEEE Trans. on Medical Imaging*, vol. 12, no. 14, pp. 664-669, 1993.
- [14] H. K. Huang, *PACS Picture Archiving and Communication Systems in Biomedical Imaging*, VCH Publishers, New York, 1996.
- [15] J. S. Kim, *Two-Dimensional Signal and Image Processing*, Prentice-Hall International, N. J., 1990.
- [16] G. B. Giannakis and M. K. Tsatsanis, "Time domain tests for Gaussianity and time-reversibility," *IEEE Transactions on Signal Processing*, vol. 42, pp. 3460-3472, 1994.

- [17] T. Müller, R. Stotzka, W. Eppler, and H. Gemmeke, "Three-dimensional reconstruction of clustered microcalcifications," *Proceedings of Computer Assisted Radiology (CAR) 98*, 1998, Tokyo, Japan.
- [18] T. Müller, R. Stotzka, A. Hochmuth, W. Eppler, and H. Gemmeke, "Volume reconstruction of clustered microcalcifications in mammograms," *Proceedings of Fourth International Workshop on Digital Mammography*, June 1998, Nijmegen, The Netherlands.
- [19] R. Stotzka, T. Müller, W. Eppler, and H. Gemmeke, "Three-dimensional reconstruction of clustered Microcalcifications from two digitized Mammograms," *SPIE's Internl. Symposium Medical Imaging*, 1998.
- [20] J. Dengler, S. Behrens, and J. F. Desaga, "Segmentation of Microcalcifications in Mammograms," *IEEE Trans. on Medical Imaging*, vol. 12, no. 4, pp. 634-642, December 1993.
- [21] W. Qian, L. P. Clarke, M. Kallergi, and R. A. Clark, "Tree-structured nonlinear filters in digital mammography," *IEEE Transactions on Medical Imaging*, vol. 13, no. 1, March 1994.
- [22] H. Chan, D. Wei, M. A. Helvie, B. Sahiner, D. D. Adler, M. M. Goodsitt, and N. Petrick, "Computer-aided classification of mammographic masses and normal tissue: linear discriminant analysis in texture feature space," *Phys. Med, Biol.*, 40, pp. 857-876, 1995.
- [23] K. Doi, M. L. Giger, R. M. Nishikawa, K. R. Hoffmann, H. Macmahon, R. A. Schmidt, and K. G. Chua, "Digital Radiography: A useful clinical tool for computer-aided diagnosis by quantitative analysis of radiological images," *Acta Radiologica*, 34, Fasc. 5, 1993.
- [24] B. Sahiner, H. P. Chan, N. Petrick, D. Wei, M. A. Helvie, D. D. Adler, and M. M. Goodsitt, "Classification of Mass and Normal Breast Tissue: A Convolution Neural Network Classifier with Spatial Domain and Texture Images," *IEEE Trans. on Medical Imaging*, vol. 15, no. 5, pp. 598-610, October, 1996.
- [25] S. Liu and E. J. Delp, "Multiresolution Detection of Stellate Lesions in Mammograms," *Proceedings of IEEE International Conference on Image Processing (ICIP)'97*, Santa Barbara, CA, pp. II:109-112, October 26-29, 1997.

- [26] M. N. Gürcan, Ö. N. Gerek, and A. E. Çetin, "Binary Morphological Subband Decomposition For Image Coding," *IEEE International Symposium on Time-Frequency and Time-Scale Analysis*, June 18-21, 1996, Paris, France.
- [27] M. N. Gürcan, Ö. N. Gerek, and A. E. Çetin, "A Morphological Subband Decomposition Structure Using GF(n) Arithmetic," *Proceedings of IEEE International Conference On Image Processing*, vol I, pp. 253-256, 16-19 September 1996, Lausanne, Switzerland.
- [28] M. N. Gürcan, Y. Yardımcı, and A. E. Çetin and R. Ansari, "Detection of microcalcifications in mammograms using nonlinear subband decomposition and outlier labeling," in *Proceedings of SPIE Visual Communications and Image Processing Conference*, pp. 909-918, 8-14 February, 1997, San Jose, CA.
- [29] M. N. Gürcan, Y. Yardımcı, A. E. Çetin, and R. Ansari, "Automated Detection and Enhancement of Microcalcifications in Mammograms Using Nonlinear Subband Decomposition," *Proceedings of IEEE ICASSP97, International Conference on Acoustics, Speech, and Signal Processing*, April 20-24, 1997, Munich, Germany.
- [30] M. N. Gürcan, Y. Yardımcı, A. Enis Çetin, and Rashid Ansari, "Detection of Microcalcifications in Mammograms Using Higher Order Statistics," *IEEE Signal Processing Letters*, vol. 4, no. 8, pp 213-216, August 1997.
- [31] M. N. Gürcan, Y. Yardımcı, and A. E. Çetin, "2-D Adaptive Filtering Based Gaussianity Tests in Microcalcification Detection," *Proceedings of SPIE Visual Communications and Image Processing Conference*, vol. 3309, part II, pp. 625- 633, 24-30 January, 1998, San Jose, CA.
- [32] M. N. Gürcan, Y. Yardımcı, and A. E. Çetin, "Microcalcification Detection Using Adaptive Filtering and Gaussianity Tests," *Proceedings of the Fourth International Workshop on Digital Mammography*, pp. 157-164, June 1998, Nijmegen, The Netherlands.
- [33] O. Egger and M. Kunt, "Embedded Zerotree Based Lossless Image Coding," *IEEE ICIP'95*, vol. II pp. 616-619., June 1995.
- [34] D. E. F. Florencio, and R. Schafer "Perfect Reconstructing Nonlinear Filter Banks," in *Proc. of IEEE Int. Conf. on Acoust., Speech, Signal Proc.*, 1996.

- [35] R. L. de Queiroz and D. A. F. Florencio, "A Pyramidal Coding Using a Nonlinear Filter Bank," in *Proc. of IEEE Int. Conf. on Acoust., Speech, Signal Proc.*, 1996.
- [36] F. J. Hampson and J. C. Pesquet, "A Nonlinear Subband Decomposition with Perfect Reconstruction," in *Proc. of IEEE Int. Conf. on Acoust., Speech, Signal Proc.*, 1996.
- [37] W. Sweldens, "Wavelets and the lifting scheme: A 5 minute tour," *Zeitschrift für Angewandte Mathematik und Mechanik*, vol. 76 (Suppl. 2), pp. 41-44, 1996.
- [38] B. Iglewicz and D. C. Hoaglin, *How to Detect and Handle Outliers*, ASQC basic references in quality control; v.16, 1993.
- [39] <ftp://figment.csee.usf.edu/pub/mammograms/nijmegen-images>.
- [40] T. Netsch, "Detection of Microcalcification Clusters in Digital Mammograms: A Scale-Space Approach," *4. Workshop Digitale Bildverarbeitung in der Medizin*, Universität Freiburg, 1996
- [41] J. S. Lim, *Two Dimensional Signal and Image Processing*, Prentice-Hall International, New Jersey, 1990.
- [42] I. Hutt, *The Computer-aided Detection of Abnormalities in Digital Mammograms*, PhD. Thesis, Department of Medical Biophysics, University of Manchester, 1996.
- [43] I. Pitas and A. N. Venetsanopoulos, *Nonlinear Digital Filters - Principles and Applications*, Massachusetts: Kluwer Academic Publishers, 1990.
- [44] Y. Barnett and T. Lewis, *Outliers in Statistical Data*, 3rd Ed. New York: John Wiley & Sons, 1994.
- [45] C. L. Nikias and A. Petropulu, *Higher Order Statistical Analysis*, Prentice-Hall, 1994.
- [46] P. J. Bickel and K. A. Doksum, *Mathematical Statistics*, Holden-Day, California, 1977.
- [47] E. R. Dougherty and J. Astola, *An Introduction to Nonlinear Image Processing*, SPIE Optical Engineering Presss, vol. TT 16, Washington, 1994.
- [48] R. J. Larsen and M. L. Marx, *An Introduction to Mathematical Statistics and Its Applications*, Prentice-Hall, 1981.

- [49] H. Yoshida, K. Doi, R. M. Nishikawa, and M. L. Giger, "An Improved Computer-Assisted Diagnostic Scheme Using Wavelet Transform for Detecting Clustered Microcalcifications in Digital Mammograms," *Academic Radiology*, vol. 3, no. 8, pp. 621-627, August 1996.
- [50] P. A. Ffrench, J. R. Zeidler, and W. H. Ku, "Enhanced Detectability of Small Objects in Correlated Clutter Using and Improved 2-D Adaptive Lattice Algorithm," *IEEE Transactions on Image Processing*, vol. 6, no. 3, pp. 383-397, March 1997.
- [51] S. G. Sankaran and A. A. Beex, "Normalized LMS Algorithm with Orthogonal Correction Factors," *Proceedings of 31st Annual Asilomar Conference on Signals, Systems and Computers*, Pacific Grove, CA, pp. 1670-1673, Nov. 1997.
- [52] Ö. N. Gerek, *Image Coding for Digitized Libraries*, PhD. Thesis, Department of Electrical and Electronics Engineering, Bilkent University, Ankara, Turkey, September, 1998.
- [53] R. C. Gonzales and P. Wintz, *Digital Image Processing*, Addison-Wesley, New York, 1987.
- [54] R. Ojeda, J. Cardoso, and E. Moulines, "Asymptotically Invariant Gaussianity Test For Causal Invertible Time Series," *Proceedings of IEEE International Conference on Acoustics, Speech, and Signal Processing*, vol. 5, pp. 3713-3716, April 21-24, 1997.
- [55] E. Moulines and K. Choukri, "Time-Domain Procedures for Testing that a Stationary Time-Series is Gaussian," *IEEE Transactions on Signal Processing*, vol. 44, no. 8, pp. 2010-2025, August 1996.
- [56] B. Mulgrew and C. F. N. Cowan, *Adaptive Filters and Equalizers*, Kluwer Academic Publishers, Boston, 1988.
- [57] R. W. Lucky, "Techniques for Adaptive Equalization of Digital Communication Systems," *Bell System Technical Journal*, vol. 45, no. 2, pp. 255-286, Feb. 1966.
- [58] W. W. Hines and D. C. Montgomery, *Probability and Statistics in Engineering and Management Science*, John Wiley and Sons, New York : 1980.

- [59] D. Guliato, R. M. Rangayyan, J. A. Zuffo, and J. E. L. Desautels, "Detection of Breast Tumor Boundaries Using Iso-Intensity Contours and Dynamic Thresholding," *Digital Mammography*, Kluwer Academic Publishers, pp 253-260, 1998.
- [60] L.A. Zadeh, "Fuzzy Sets," *Information and Control*, 8:338-353, 1965.
- [61] M. Kass, A. Witkin, and D. Terzopoulos, "Snakes: Active contour models," *Int. J. Computer Vision*, vol. 1, no. 4, pp. 321-331, 1988.
- [62] F. Leymarie and M. D. Levine, "Tracking Deformable Objects in the Plane Using an Active Contour Model," *IEEE Trans. on Pattern Analysis and Machine Intelligence*, vol. 15, no. 6, pp. 617-633, 1993.
- [63] A. A. Amini, S. Tehrani, and T. E. Weymouth, "Using dynamic programming for minimizing the energy of active contours in the presence of hard constraints," *Proceedings of Second International Conference on Computer Vision*, pp. 95-98, 1988.
- [64] D. J. Williams and M. Shah, "A fast algorithm for active contours," *IEEE Trans. on PAMI*, vol. 4, pp. 592-595, 1990.
- [65] F. R. Hampel, E. M. Ronchetti, P. J. Rousseeuw, and W. A. Stahel, *Robust Statistics: The Approach Based on the Influence Functions*, John Wiley & Sons, New York : 1986.
- [66] J. W. Tukey, *Exploratory Data Analysis*, Addison-Wesley, Reading, Mass. : 1971.
- [67] M. Koyuturk, M. N. Gürcan, and A. E. Cetin, "Mammogramlarda Kutle Lezyonlarının Yılan Algoritmasıyla Otomatik olarak Sezinlenmesi," *6. Sinyal İşleme ve Uygulamaları Kurultayı*, pp. 334-339, Ankara, 1998 (in Turkish).
- [68] M. N. Gürcan, M. Koyuturk, H. S. Yildiz, R. Cetin-Atalay, and A. E. Cetin, "Identification of Relative Protein Bands in Polyacrylamide Gel Electrophoresis (PAGE) Using Multiresolution Snake Algorithm," *Proceedings of IEEE-SP International Symposium on Time-Frequency/Time-Scale Analysis*, pp. 277-280, October 7-9, 1998, Pittsburgh, Pennsylvania, USA, also *Biotechniques* (in press).
- [69] O. N. Gerek, M. N. Gürcan, and A. E. Cetin, "Frequency band characteristics of tree-structured filter banks," *Electronics Letters*, vol. 32, No. 8. pp.724-726, 1996.

- [70] A. N. Akansu and R. A. Haddad, *Multiresolution Signal Decomposition - Transforms, Subbands, Wavelets*, Academic Press, Inc., San Diego, CA, 1992.
- [71] P. P. Vaidyanathan, *Multirate Systems and Filter Banks*, Prentice Hall, Inc., Englewood Cliffs, NJ, 1993.
- [72] N. J. Fliege, *Multirate Digital Signal Processing*, John Wiley and Sons, Ltd., West Sussex, England, 1994.
- [73] C. Guillemot, A. E. Cetin, and R. Ansari, 'M-channel nonrectangular wavelet representation for 2-D signals,' in the book *Wavelets in Image Communication* edited by M. Barlaud, Elsevier, December 1994.
- [74] A. E. Cetin, Ö. N. Gerek, and Ş. Ulukuş, 'Block Wavelet Transforms for Image Coding,' *IEEE Trans. Circuits and Systems for Video Technology*, vol. 3, no. 6, pp. 433-435, Dec. 1993.
- [75] E. M. Reingold, J. Nievergelt, and N. Deo, *Combinatorial Algorithms - Theory and Practice*, Prentice Hall, Inc., Englewood Cliffs, NJ, 1977.
- [76] R. C. Allen, C. A. Savaris, and H. R. Marier, *Gel Electrophoresis and Isoelectric Focusing of Proteins : Selected Techniques*, Walter de Gruyter, Berlin, 1984.
- [77] M. M. Bradford, "A rapid and sensitive method for quantitation of microgram quantities of protein utilizing the principle of protein-dye binding", *Anal. Biochem*, 72:248-254, 1976.
- [78] C.W. Kim, R. Ansari, and A. E. Cetin, 1992, "A class of linear-phase regular biorthogonal wavelets," *IEEE International Conference on Acoustics, Speech, and Signal Processing (ICASSP'92)*, San Francisco, USA, 1992.
- [79] M. Vetterli and J. Kovacevic, *Wavelets and Subband Coding*, Prentice Hall, New Jersey, 1995.

Vita

Metin Nafi Gürcan was born in Burdur, Turkey, on March 12, 1970. He received his B.Sc. degree from the Department of Electrical & Electronics Engineering at Bilkent University, Ankara, Turkey, in 1991 and his MSc. degree in Digital Systems Engineering from the University of Manchester Institute of Science and Technology, Manchester, United Kingdom, in 1994. He then pursued his Ph.D studies at the Department of Electrical and Electronics Engineering, Bilkent University. He was a visiting researcher at the Electrical Engineering Department, University of Minnesota, in 1996 and 1997 winters. He is the recipient of British Foreign and Commonwealth Organization Award in 1992. His research interests include computer-aided diagnosis, signal/image processing theory and its applications in medicine and biology.